UCLA
UCLA Electronic Theses and Dissertations

Title
Multi-Dimensional Quantitative Dynamic Contrast Enhanced Magnetic Resonance Imaging Using Multitasking: Technical Development and Applications

Permalink
https://escholarship.org/uc/item/6j3860ps

Author
Wang, Nan

Publication Date
2020

Peer reviewed|Thesis/dissertation

eScholarship.org Powered by the California Digital Library
University of California

UNIVERSITY OF CALIFORNIA

Los Angeles

Multi-Dimensional Quantitative Dynamic Contrast Enhanced Magnetic Resonance Imaging Using Multitasking: Technical Development and Applications

A thesis submitted in partial satisfaction

of the requirements for the degree Doctor of Philosophy

in Bioengineering

by

Nan Wang

2020

© Copyright by

Nan Wang

2020

ABSTRACT OF THE DISSERTATION

Multi-Dimensional Quantitative Dynamic Contrast Enhanced
Magnetic Resonance Imaging Using Multitasking:
Technical Development and Applications

by

Nan Wang

Doctor of Philosophy in Department of Bioengineering

University of California, Los Angeles, 2020

Professor Debiao Li, Chair

Dynamic contrast enhanced (DCE) MRI plays a central role in the diagnosis, characterization, and treatment monitoring of various diseases. It can provide essential functional information of the tissues, including the perfusion and permeability properties. Besides, the changes in functional properties is recognized to precede the morphological alterations, which can potentially provide an avenue for early diagnosis and treatment evaluation.

However, current practice of DCE MRI continues to face demanding technical challenges. First, there is direct conflict in the requirements for adequate anatomical

coverage and high spatial and temporal resolution for tissues characterization. Existing techniques usually compromise one or more aspects, leading to suboptimal protocol. Second, dynamic T1 mapping for the quantification of CA concentration is hard to realize. Approximation in this step can introduce error in the derivation of DCE parameters. Third, imaging of some organs, such as heart or abdominal organs, is subject to artifacts caused by physiological motion, which can significantly degrade image quality or increase the scan time. Forth, the growing concern towards Gd deposition within body parts makes it controversial to use contrast agent.

The primary goal of the work in the dissertation is to address the aforementioned limitations by developing a novel quantitative DCE MRI technique using MR Multitasking framework to achieve: 1) motion-resolved imaging with free-breathing acquisition and bulk-motion correction, 2) high spatial-temporal resolution with 3D anatomical coverage for simultaneous perfusion and permeability quantification, 3) dynamic T1 mapping for accurate quantification of CA concentration and potentials for reducing GBCA dose. All the technical advancements aims to improve the detection, staging, characterization, and treatment monitoring for multiple organs and diseases. There are three specific aims to achieve the ultimate goal.

First, the Multitasking DCE technique was developed and tested in the study of carotid atherosclerosis. It enables 3D coverage of entire carotid vasculature with high spatial resolution (0.7 mm isotropic), high temporal resolution (600 ms), and dynamic T1 mapping for direct quantification of CA concentration. Bulk motion detection and removal scheme were also implemented for the improvement of image quality. In vivo studies have shown that the proposed technique can achieve accurate T1 quantification and

robustness to motion. The PK parameters were repeatable in vivo and showed significant difference between carotid atherosclerosis and normal carotid vessel wall.

Second, 6-dimensional (6D) Multitasking DCE technique was developed for the characterization of PDAC. It achieves respiratory-motion-resolved, high-temporal-resolution T1 quantification of the entire abdomen in a 10-min free-breathing scan. Sixteen healthy volunteers and 14 patients with pathologically confirmed PDAC were recruited for the in vivo study. The results demonstrated that the quantitative PK parameters using Multitasking DCE were repeatable in vivo and showed significant differences between normal pancreas, tumor and non-tumoral regions in PDAC patients. In addition, 8 patients with confirmed CP were recruited. The PK parameters representing blood flow and vascular properties showed significant difference between normal pancreas, PDAC, and CP.

Third, the Multitasking DCE technique using a low dose at 0.02 mmol/kg (LD-MT-DCE) was developed for breast imaging. It produced co-registered high-spatial-resolution (0.9 mm × 0.9 mm × 1.14 mm) dynamic T1 maps at 1.4-second temporal resolution with whole-breast coverage in the 10-min scan. The dose was chosen to be 0.02 mmol/kg, 20% of the standard dose, based on a numerical simulation conducted to evaluate the dose effect on the accuracy and precision of the PK parameters quantified using LD-MT-DCE. Twenty healthy volunteers and 7 patients with breast cancer were recruited for the in vivo study. The results demonstrated that LD-MT-DCE were repeatable, showed excellent image quality and equivalent diagnosis compared with standard-dose clinical DCE. The estimated PK parameters were capable of differentiating between normal breast tissue, and benign and malignant tumors.

The dissertation of Nan Wang is approved.

Peng Hu

Holden H. Wu

Zhaoyang Fan

Debiao Li, Committee Chair

University of California, Los Angeles

2020

Dedicated to the ones I love,

who have unconditionally supported me

throughout my graduate studies:

My lovely parents: Jie Liu & Dejun Wang

My husband: Sen Ma

TABLE OF CONTENTS

ABSTRACT OF THE DISSERTATION ..... **II**

LIST OF ACRONYMS ..... **XIV**

LIST OF FIGURES ..... **XVIII**

LIST OF TABLES ..... **XXV**

ACKNOWLEDGEMENTS ..... **XXVII**

VITA ..... **XXX**

CHAPTER 1: INTRODUCTION **1**

1.1 SIGNIFICANCE 1

1.2 CURRENT STATES OF DCE MRI 1

1.2.1 Qualitative DCE MRI 2

1.2.2 Semi-quantitative DCE MRI 3

1.2.3 Quantitative DCE MRI 4

1.3 MAJOR TECHNICAL CHALLENGES FOR QUANTITATIVE DCE MRI 4

1.3.1 Coverage and resolution 5

1.3.2. Physiological motion 5

1.3.3 Nonlinearity between signal intensity and CA concentration 6

1.4 CONCERN TO GBCA DEPOSITION 6

1.5 OBJECTIVE 7

1.5.1 Aim 1: To develop a novel quantitative DCE MRI technique, Multitasking DCE, for the characterization of carotid atherosclerosis that achieves dynamic T1

quantification with the coverage of entire carotid arteries, 0.7 mm isotropic resolution, and 1.2-second temporal resolution. 8
1.5.2 Aim 2: To develop a 6D Multitasking DCE for abdominal imaging with respiratory-motion-resolved, 1-second temporal resolution dynamic T1 mapping of the entire abdomen. 8
1.5.3 Aim 3: To develop the Multitasking DCE using 20% of standard GBCA dose for breast cancer detection and characterization. 8
CHAPTER 2: BACKGROUND 10
2.1 BASIC THEORY OF DCE MRI 10
2.1.1 Angiogenesis 10
2.1.2 Gadolinium-based contrast agent (GBCA) 12
2.1.3 Imaging principles 15
2.2 IMAGE ANALYSIS 16
2.2.1 Qualitative approach 16
2.2.2 Semi-quantitative approach 18
2.2.3 Quantitative approach 19
2.3 PHARMACOKINETIC MODEL 20
2.3.1 Estimating CA concentration 20
2.3.2 AIF 22
2.3.3 Vascular-interstitial exchange 22
2.3.4 Two compartment exchange model (2CXM) 25
2.3.5 Simplified model 27
2.4 STATE-OF-ART PRACTICE OF DCE MRI 28

2.4.1 Clinical practice 28
2.4.2 Novel techniques 30
2.4.3 Major technical challenges and concerns 33
2.5 MR MULTITASKING FRAMEWORK 33
2.5.1 Image model 33
2.5.2 Sampling and reconstruction strategies 35
2.5.3 Tensor subspace estimation 36
CHAPTER 3: MULTITASKING DCE MRI IN THE CHARACTERIZATION OF CAROTID ATHEROSCLEROSIS 39
3.1 INTRODUCTION 39
3.2 METHODS 41
3.2.1 Sequence design 41
3.2.2 Sampling pattern 41
3.2.3 Image reconstruction 42
3.2.4 Dynamic T1 quantification and PK model 44
3.2.5 Abrupt motion removal 45
3.2.6 Simulations 47
3.2.7 Imaging experiments 48
3.2.8 Phantom study 49
3.2.9 In vivo study 49
3.2.10 Image analysis 50
3.2.11 Inter-session repeatability at different temporal resolution 51
3.2.12 Statistical analysis 51

3.3 RESULTS 52
3.3.1 Simulations 52
3.3.2 Phantom measurements 54
3.3.3 In vivo measurements 55
3.3.4 Effects of motion removal 60
3.3.5 Inter-session repeatability at different temporal resolution 61
3.4 DISCUSSION 61
3.5 CONCLUSION 64

CHPTER 4: SIX-DIMENSIONAL MULTITASKING DCE OF ENTIRE ABDOMEN: METHODS AND APPLICATION TO PANCREATIC DUCTAL ADENOCARCINOMA (PDAC) 65

4.1 INTRODUCTION 65
4.2 METHODS 66
4.2.1 Sequence design 66
4.2.2 Image reconstruction 67
4.2.2.1 respiratory motion identification 67
4.2.2.2 Respiratory motion compensation 69
4.2.2.3 Tensor subspace estimation 70
4.2.2.4 Spatial coefficient recovery 71
4.2.3 Dynamic T1 quantification and PK modeling 71
4.2.4 Imaging experiments 72
4.2.4.1 Imaging protocol 72
4.2.4.2 Phantom study 73

4.2.4.3 In vivo study 74
4.2.5 Image analysis 75
4.2.6 Statistical analysis 76
4.3 RESULTS 76
4.3.1. Phantom measurements 76
4.3.2. Effect of respiratory motion compensation 79
4.3.3. In vivo measurements 79
4.4 DISCUSSION 86
4.5 CONCLUSION 90
CHAPTER 5: DIFFERENTIATING PANCREATIC DUCTAL ADENOCARCINOMA AND CHRONIC PANCREATITIS USING SIX-DIMENSIONAL QUANTITATIVE MULTITASKING DCE 91
5.1 INTRODUCTION 91
5.2 METHODS 93
5.2.1 Study population 93
5.2.2 MRI protocol 93
5.2.3 Image Analysis 94
5.2.4 Statistical Analysis 94
5.3 RESULTS 95
5.4 DISCUSSION 98
5.5 CONCLUSION 100
CHPATER 6: QUANTITATIVE LOW-DOSE MULTITASKING DCE (LD-MT-DCE) FOR BREAST CANCER 101

6.1 INTRODUCTION 101
6.2 METHODS 103
6.2.1 Sequence design 103
6.2.2 Image reconstruction 103
6.2.3 Motion compensation 105
6.2.4 PK modeling 105
6.2.5 Simulations 107
6.2.6 Imaging experiments 108
6.2.6.1 Imaging protocol 108
6.2.6.2 Volunteer study 109
6.2.6.3 Patient study 110
6.2.7 Image analysis 110
6.2.8 Statistical analysis 112
6.3 RESULTS 112
6.3.1 Simulations 112
6.3.2 In vivo demonstration 114
6.3.3 Volunteer study 116
6.3.4 Patient study 120
6.4 DISCUSSIONS 124
6.5 CONCLUSION 128
CHAPTER 7: CONCLUSIONS AND FUTURE INNOVATIONS 129
7.1 SUMMARY OF THE WORK 129
7.1.1 Multitasking DCE in carotid atherosclerosis 130

7.1.2 Multitasking DCE in abdomen 130
7.1.3 Multitasking DCE in breast with low-dose 131
7.2 FUTURE WORK 132
7.2.1 Accelerating image reconstruction 132
7.2.2 Application of LD-MT-DCE to a variety of pathological conditions 132
7.2.3 Animal studies with histological validation 134
7.2.4 Follow-up study for therapy monitoring 135
7.2.5 Early diagnosis incorporating deep learning 135
REFERENCE 137

LIST OF ACRONYMS

General

T — Tesla

mT — millitesla

mm — millimeter

s — second

ms — millisecond

min — minute

CT — computerized tomography

Statistics

ANOVA — analysis of variance

ICC — intra-class correlation coefficient

CoV — coefficient of variation

R — regression coefficient

P — statistical significance coefficient

Mathematics

SVD — singular value decomposition

LRT — low-rank tensor

Medicine

ECG — echocardiography

PDAC — pancreatic ductal adenocarcinoma

CP — chronic pancreatitis

TNBC — triple negative breast cancer

MVD — microvascular density

EES — extravascular extracellular space

BF — blood flow

Magnetic Resonance Imaging

MRI — magnetic resonance imaging

SNR — signal-to-noise ratio

CNR — contrast-to-noise ratio

FOV — field of view

ROI — region of interest

2D/3D/4D/5D/6D — two/three/four/five/six dimensions

RF — radiofrequency

B0 — main magnetic field of MRI system

B1 — excitation of RF field orthogonal to B0

TE — echo time

TR — repetition time

T1W — T1 weighted

T2W — T2 weighted

PD — proton density

IR — inversion recovery

SR — saturation recovery

TI — inversion time

FA — flip angle

SS — single shot

EPI — echo planar imaging

SE — spin echo

TSE — turbo spin echo

GRE — gradient echo

FLASH — fast low angle shot

DWI — diffusion weighted imaging

VIBE — volumetric interpolated breath-hold examination

HASTE — half-Fourier acquisition single-shot turbo spin-echo

MOLLI — modified look-lock inversion recovery

STIR — short-TI-inversion-recovery

MRCP — magnetic resonance cholangiopancreatography

CE — contrast enhanced

DCE — dynamic contrast enhanced

KWIC — k-space weighted image reconstruction

GRASP — golden-angle radial sparse parallel technique

XD-GRASP — extra-dimensional GRASP

CA — contrast agent

Gd — gadolinium

GBCA — gadolinium based contrast agent

AUC — area under concentration-versus-time curve

TTP — time to peak

SER — signal enhancement ratio

PK — pharmacokinetic

AIF — arterial input function

PS — permeability-surface area product

2CXM — two-compartment exchange model

TH — tissue-homogeneity model

AATH — adiabatic approximation tissue-homogeneity model

DP — distributed parameter model

TK — Tofts-Kermode model

LIST OF FIGURES

Figure 2.1 Basic types of primary vascular growth. Redrawn after Carmeliet and Collen (2000)……...10

Figure 2.2 Illustration of CA concentration curves for AIF and tissues of interest……16

Figure 2.3: Common categories of the types of signal enhancement curve: type 1, persistent increase; type 2, plateau; type 3: wash-out……..17

Figure 2.4: Illustration of semi-quantitative parameters……19

Figure 2.5: Scheme of two-region architecture and capillary-interstitium exchange…...23

Figure 2.6: Principles of KWIC reconstruction technique. a Diagram of the four-interleaf angle-bisection reordering acquisition scheme is presented using a simple example composed of eight projection views. During MR scanning of one full-frame image series, k-space data are acquired radially so that subsequent projection views bisect the earlier ones. Projection views are grouped into four interleaved subsets that are serially acquired. b For the reconstruction of full-frame images by gridding, data from all subsets are combined without weighting. For the reconstruction of subframe images by KWIC view-sharing, the central k-space is filled with data of the timely subset and the adjacent k-space at the Nyquist-radius is filled with data from the time-contiguous subset. The outermost K-space is filled with data from all subsets. c The four time-resolved subframe KWIC images have different k-space cores and similar k-space peripheries. This KWIC view-sharing is possible because of the oversampled, central k-space data of radial MRI. Data of a single subframe image set can improve the effective temporal resolution by a factor of 4. Redrawn after Kim (2013)……..31

Figure 3.1 (A): Pulse sequence diagram for the proposed 5D DCE and corresponding simulated signal evolution for vessel wall and blood. Non-selective saturation recovery preparation pulse is applied every TR followed by a series alpha pulses. A readout lines is collected every alpha pulse. This SR period is repeated to traverse the entire k-space seven times during the scan. The contrast media is injected when 144 SR periods was collected. (B): Simplified illustration of k-space sampling strategy. Cartesian acquisition with randomized reordering in ky and kz directions is implemented according to a variable-density Gaussian distribution. A center k-space line is acquired every 8 lines as the LRT subspace training data. Rest of the data forms the imaging data……..42

Fig 3.2: The result of fitted dynamic T1 compared with the true value. The fitted dynamic T1 curves are the mean value over the ROI……...52

Fig 3.3: Pixel-wised parametric mapping. The first column shows the true map of the parameter. The second column shows the fitted map. The third column shows the absolute relative difference of the fitted map compared with the true map……...53

Figure 3.4: Simulation results for the comparison between Multitasking approach, LA, and NLA. Each bar graph displays the mean relative error of the estimated parameter at different temporal resolution. The error bar represents the relative standard deviation of 100 repetitions. When temporal resolution is high (<10 seconds), Multitasking approach showed best performance in the estimation of PK parameters, producing the smallest bias and standard deviation for both tissues and all parameters……..54

Figure 3.5: Phantom measurements. (A): T1 mapping of the pre- and post-contrast phantoms using Multitasking DCE and reference IR-SE. (B): Comparison of T1 quantification using the proposed Multitasking DCE versus a standard reference method (IR-spin echo). The solid black line represents y = x while the dashed red lines stands for the regression of the results from two methods ($R^2 = 0.96$). The error bar shows the standard deviation for each measured T1. (C): The Bland–Altman plot shows inter-session repeatability of the T1 measurement of the proposed protocol measured on two different days. Solid line and dashed lines indicate the means and standard deviation of the T1 values between different measurement, respectively……55

Figure 3.6: Representative image set from a study of a normal subject using the proposed method. Multi-phase images are reconstructed with the LRT framework in the SR dimension (images at different SR times) and dynamic enhancement dimension (images at different time after injection). Zoomed-in images are the transversal view of the locations marked by yellow lines. Multiple SR phases allows T1 quantification and direct estimation of contrast concentration. Three key DCE phases are shown along horizontal axis, including pre-injection, peak enhancement, and washing out. DCE temporal footprint is 1.2 s……56

Figure 3.7: (A): Real-time signal evolution of three representative tissues from a healthy subject. The zoom-in area in the image of blood signal shows the SR curves during the peak enhancement. (B) Dynamic T1 mapping based on the SR information. (C)

Contrast agent concentration curves derived directly from the T1 mapping according to contrast media relaxivity……..57

Figure 3.8: Examples of kinetic parametric mappings. The gray-scale images are the post-contrast T1-weighted images in coronal view. The overlaid color maps on the zoomed-in area in transversal view are AUC, v_p, K^{trans} and v_e maps. (A) is an example from a healthy subject with thin vessel wall. The location of the zoomed-in images in red and blue frames are marked by the red and blue lines in the coronal image in (A), respectively. (B) is from a 58-year old patient with lipid core. (C) is from a 69-year-old patient with intra-plaque hemorrhage. The location of zoomed-in area is marked by the red line in the coronal image in (B) and (C), respectively. The plaques were marked by white arrows on the AUC maps…….58

Figure 3.9: Inter-session repeatability of the kinetic parameters v_p, K^{trans}, v_e and AUC, as measured by mean absolute interscan difference. Seven healthy subjects received the second scan with the same protocol on a separate day. The Bland-Altman plots show good repeatability of the kinetic parameters…….58

Figure 3.10: Effects of motion removal in the proposed method. Abrupt motion is a common issue in DCE studies. Without motion removal, images may be corrupted by artifacts. Reconstructed images with motion removal shows sharper and superior delineation of different tissue types. (A) is an image corrupted by motion artifacts. The set of red arrows mark a blurry structure. The dashed yellow arrow marks a vessel with corrupted contrast. (B) is the image from the same subject after motion removal. The area marked by red arrows has much clearer structure. The vessel marked by dashed yellow arrow has more reasonable contrast and better delineation…….59

Figure 3.11: Inter-session repeatability at different temporal resolution. The repeatability between two scans was evaluated at different temporal resolutions retrospectively. The chosen temporal resolutions were 595 ms, 1.2s, 1.8s, 2.4s, 3.6s, 4.8s, and 7.2s. When temporal resolution<1s, the average repeatability was not as good because of the reduced SNR. When temporal resolution>3s, the repeatability decreased due to the worse depiction of fast-changing dynamic information. The best repeatability achieved when temporal resolution = 1.2s……...60

Figure 4.1: Respiratory binning scheme. (A) A narrow bar-shaped ROI in the head-foot direction was manually drawn on top of the liver-air interface. (B) The signal at each last-TI phase within the ROI was averaged over left-right direction as a 1D

projection. The 1D projection over the duration of the scan formed a 2D spatial-temporal profile showing the location changes of the liver dome. (C) The position of the liver dome was extracted and then divided into 6 respiratory bins……...68

Figure 4.2: Phantom measurements. (A) T1 maps from the Multitasking DCE and reference IR-SE sequence of the T1 layer of ISMRM/NIST MRI system phantom. (B) Regression of T1 of the proposed Multitasking DCE versus IR-SE. The solid line represents y = x while the dashed lines stands for the regression of the T1 from two methods ($R^2 = 0.970$). (C) The Bland–Altman plot shows reproducibility of the T1 measurement of the Multitasking DCE measured on two different days. Solid line and dashed lines indicate the mean value and 1.96 of standard deviation of the T1 between different measurements, respectively……77

Figure 4.3: Effect of respiratory motion compensation. The images without and with respiratory compensation are shown at two DCE phases, one pre-contrast phase and one post-contrast phase. The CA concentration curve of pancreas are displayed. Images with compensation show less artifacts and improved structure delineation. The red thick arrows mark the pancreas, which is much sharper with less artifacts for both pre-contrast images with compensation. The yellow thin arrows mark small vessels, which shows clearer boundary and improved contrast on images with motion compensation. The green dashed arrows point out that the CA concentration curve with compensation is much cleaner with less oscillation.....78

Figure 4.4: Representative 6D images with 3 spatial dimensions, a SR dimension, a respiratory dimension and a DCE time course. Images are displayed at pre-contrast phase, arterial phase (t_d = 20 s), venous phase (t_d = 60 s), and equilibrium phase (t_d = 4 min). For each DCE phase, images of end-inspiration (bin 1) and end-expiration (bin 6) phases at τ = 470 ms are shown in coronal orientation; images of different saturation recovery time τ (τ = 168 ms and τ = 470 ms) at end-expiration phase are shown in transversal view with clear pancreas delineation. t_d is the time from injection……80

Figure 4.5: Transformation from signal intensity to contrast agent concentration. (A) Representative signal profiles of blood, normal pancreas and PDAC displayed at end expiration. The zoom-in area in the image of blood signal shows the SR curves during the peak enhancement. (B) Dynamic T1 mapping based on SR periods. (C) Contrast agent concentration curves derived directly from the T1 mapping according to contrast media relaxivity……..81

Figure 4.6: Representative maps of kinetic parameters of a 32-year-old subject in control group (A) and a 57-year-old subject with PDAC marked by yellow solid circle (B). The gray-scale image in each case is a transversal slice with excellent pancreas delineation at the arterial phase. The overlaid color maps display v_p, K^{trans}, v_e, and K_{ep} of the pancreas. In (B), the tumor region has lower v_p, K^{trans}, K_{ep} and higher v_e than the surrounding non-tumoral regions. The area marked by the red dashed line in (B) is a hypo-enhancing cyst……81

Figure 4.7: Bland-Altman plots evaluating the in vivo reproducibility of the kinetic parameters from Multitasking DCE on the eight subjects in control group who received the scan twice on separate days. The solid lines indicate the mean bias and the dashed lines indicate the 95% limit of agreement. The ICC and CoV of each parameter are listed on top of the corresponding plot……84

Figure 4.8: Bar graph showing the mean value and standard deviation of v_p, K^{trans}, v_e, and K_{ep} for control group, tumor and non-tumoral regions in patient group. The P values between each two categories by one-way unbalanced ANOVA with Holm-Bonferroni correction are marked on top of the bar graph. All the four parameters were significantly different in the comparison between tumor and control and between tumor and non-tumor. The K^{trans}, v_e and K_{ep} between control and non-tumor also showed significant difference……85

Figure 5.1: Conversion from signal intensity to CA concentration. (A) Representative signal profiles of blood, normal pancreas, CP and PDAC displayed at end expiration. The zoom-in area in the image of blood signal shows the SR curves during the peak enhancement. (B) Dynamic T1 mapping based on SR periods. (C) CA concentration curves derived directly from the T1 mapping according to contrast media relaxivity. ……..95

Figure 5.2: Representative maps of kinetic parameters of a 25-year-old subject in control group (A), a 77-year-old subject with PDAC marked by yellow solid circle (B), and a 65-year-old subject with CP. The gray-scale image in each subfigure is a transversal slice at the arterial phase. The overlaid color maps display v_p, K^{trans}, v_e, and K_{ep} of the pancreas……..96

Figure 5.3: Bar graph showing the mean value and standard deviation of v_p, K^{trans}, v_e, and K_{ep} for control group, PDAC, non-tumoral regions in PDAC group (denoted as NT), and CP. The P values between PDAC versus CP, PDAC versus normal, and CP versus normal are labeled on top of each sub-graph. All the four parameters were

significantly different in the comparison between PDAC versus CP and between PDAC versus normal. The K^{trans}, v_e and K_{ep} between CP and normal also showed significant difference……...97

Figure 6.1: Simulations results. Each bar graph displays the mean relative error between the estimated parameter and the true parameter for GBCA dose from 0.01 mmol/kg to 0.1 mmol/kg at one SNR level. The error bars show the relative standard deviation of the 20 repetitions for each condition. For a dose equivalent or larger than 0.02 mmol/kg, the mean relative errors and relative standard deviations are within 2% for both tumor and normal tissue……113

Figure 6.2: Representative 5D images of LD-MT-DCE from a 66-year-old patient. Images are displayed at pre-contrast phase, peak-enhancement phase (t = 40 s), and delayed phase (t = 5 min). For each DCE phase, images at two different saturation recovery times (τ = 350 ms and τ = 1380 ms) are shown in axial and sagittal views with clear tumor delineation. t is the time from injection……115

Figure 6.3: Transformation from signal intensity to CA concentration. (A) Representative signal profiles of blood, normal breast tissue, and malignant tumor. The zoom-in area shows the SR curves during the enhancement. (B) Dynamic T1 mapping based on SR periods. (C) Contrast agent concentration curves derived directly from the T1 mapping according to CA relaxivity……...116

Figure 6.4: Representative maps of PK parameters showing normal breast tissue from a 52-year-old healthy volunteer (A), a benign tumor (marked by a yellow solid boundary) from a 49-year-old patient (B), and a malignant tumor (marked by a red dashed boundary) from a 65-year-old patient (C). The gray-scale images display peak-enhanced LD-MT-DCE images. The overlaid colormaps represents F_p, v_p, K^{trans}, v_e, $iAUC_{60}$, and $iAUC_{120}$, respectively. The malignant tumor has the highest F_p, v_p, K^{trans}, $iAUC_{60}$, and $iAUC_{120}$ values……...117

Figure 6.5: Motion compensation effect of a patient of 51 years old. (A) Peak-enhanced phase of clinical DCE. The tumor is labeled by the red dashed boundary, showing clear structure. (B) Motion-corrupted phase in LD-MT-DCE due to movement of the patient. Yellow arrows point out motion artifacts. The tumor structure is unclear. (C) The image after motion compensation. The motion artifacts are removed. The tumor has largely improved delineation……118

Figure 6.6: Repeatability evaluation for PK parameters on the repeat LD-MT-DCE data. The regression coefficients, ICC, and CoV between the estimation using the first and second LD-MT-DCE images were evaluated and displayed for all parameters……119

Figure 6.7: Correlation between the PK parameters estimated using LD-MT-DCE and SD-MT-DCE. The regression coefficients, ICC, and CoV were evaluated for the dose-independent parameters F_p, v_p, K^{trans}, v_e. For dose-dependent parameters $iAUC_{60}$, and $iAUC_{120}$, the regression coefficients between LD-MT-DCE and SD-MT-DCE were assessed……..119

Figure 6.8: (A) Representative images from LD-MT-DCE and clinical DCE of a 58-year-old patient. The original DCE images display the images at peak-enhancement phase for both methods. The subtracted images are the original DCE images subtracting pre-contrast images. Dynamic curves from LD-MT-DCE and clinical DCE are displayed. With higher temporal resolution, LD-MT-DCE produces dynamic curves with more temporal details. (B) Bar graphs showing the CNR for original DCE images at peak-enhancement phase and subtracted images for all patients. The CNR of subtracted images shows no difference between LD-MT-DCE and clinical DCE……..121

Figure 6.9: Bar graph showing the mean value and standard deviation of F_p, v_p, K^{trans}, v_e, $iAUC_{60}$, and $iAUC_{120}$ for control group, benign tumors and malignant tumors in patient group. The P values between each pair by one-way unbalanced ANOVA with Tukey test are marked on top of the bar graphs. F_p, v_p, K^{trans}, $iAUC_{60}$, and iAUC120 were significantly different between control breast tissue and malignant tumor; F_p, v_p, $iAUC_{60}$, and iAUC120 were significantly different between control and benign tumor; F_p, v_p, and K^{trans} were significantly different between malignant and benign tumor. * indicates statistically significant difference……122

Figure 7.1: Repeatability evaluation for PK parameters on the repeat LD-MT-DCE data in pancreas. The regression coefficients, ICC, and CoV between the estimation using the first and second LD-MT-DCE images were evaluated and displayed for all parameters……133

Figure 7.2: Correlation between the PK parameters estimated using LD-MT-DCE and SD-MT-DCE. The regression coefficients, ICC, and CoV were evaluated and displayed for all parameters……..134

LIST OF TABLES

Table 2.1 GBCA relaxivity rate. ……14

Table 2.2: List of PK parameters……..25

Table 3.1: Multitasking DCE sequence parameters……..49

Table 3.2: The mean and standard deviation of the kinetic parameters compared with the true value. The standard deviation reports the variance of parameter value within the ROI. The mean error reports bias of the estimated values……53

Table 3.3: MOLLI reference values in healthy subjects……...56

Table 3.4: Kinetic modeling properties in healthy subjects (n = 14) and patients with known carotid atherosclerosis (n = 7). For v_p, K^{trans} and AUC the mean values of patient group were significantly higher than the mean value of healthy group….59

Table 4.1: List of imaging parameters……..73

Table 4.2: Size and location of the tumor for all the patients. The size of the tumor is defined as the largest diameter in axial CT images according to RECIST 1.1 criteria……...74

Table 4.3: Comparison of SNR and SHP without motion compensation (NMC) and with motion compensation (MC) over all the cases (N = 30). One-tailed t test were applied and the P value are listed. The equilibrium phase is t_d = 4 min, where t_d is the time after injection……78

Table 4.4: Comparison of in vivo T1 measurements between Multitasking DCE and MOLLI. The mean values and standard deviation of pre- and post-contrast T1 from Multitasking DCE and MOLLI are listed for healthy pancreas in control group, tumor and non-tumoral regions in patients. The ICC and P value by paired t-test between T1 measured by MOLLI and Multitasking are provided. The ICC of each category indicates good agreement of in vivo T1 measurement between Multitasking DCE and MOLLI……83

Table 4.5: Statistical result of v_p, K^{trans}, v_e, and K_{ep} for control group, tumor and non-tumoral regions in patient group. * indicate statistical significance……..85

Table 5.1: P value of v_p, K^{trans}, v_e, and K_{ep} for each pair. * indicate statistical significance……..98

Table 6.1: List of imaging parameters……...109

Table 6.2: Comparison of the image quality and diagnosis results between LD-MT-DCE and clinical DCE. The number of malignant tumors and benign tumors were diagnosed on clinical DCE. The image quality of both methods are listed. The LD-MT-DCE images were scored as “excellent” for 5 cases and equal or above “good” for the other 2 cases by both radiologists. In 6 cases, the diagnosis results of LD-MT-DCE perfectly match the results of clinical DCE in terms of the location, size, type, margin, and perfusion type…….120

Table 6.3: Detailed information about tumors detected in patient group…….123

Table 6.4: Detailed statistical results of F_p, v_p, K^{trans}, v_e, $iAUC_{60}$, and $iAUC_{120}$ for control group, benign tumors and malignant tumors in patient group. C: control; B: benign tumor; M: malignant tumor. * indicates statistically significant difference…….124

ACKNOWLEDGEMENTS

I would like to extend my deepest gratitude to my advisor Dr. Debiao Li. It is truly lucky of me to join his lab and have his guidance and support throughout my PhD career. He has provided me with endless research resources including sufficient MR scanner access, insightful instructionss on my work and the big picture of the field of medical imaging, and encouragement when facing challenges. From him I have learned that always keep the vision to the frontier of the development of science, that always keep a wide-open mind to collaborate with others, and that the ultimate goal of research is always to translate it into productivity and to serve people. These valuable qualities can surely benefit my future research career.

In addition, I would like to express my appreciation to Dr. Anthony Christodoulou, Dr. Yibin Xie, and Dr. Zhaoyang Fan. They are talented and diligent young scientists, who have provided me with valuable and detailed instructions on my research work. They have been leading me and mentoring me since my first step into the MRI field. From them I have learned a mass of knowledge of medical background, sequence design, image reconstruction, data analysis, etc., and that how to turn my knowledge into research. They are respectable mentors and friends.

I would like to extend my gratitude to my doctoral committee, Dr. Peng Hu, Dr. Holden H. Wu, and Dr. Daniel Ennis. They have guided me starting my PhD qualification exam, offering valuable advice and instructions. Discussions with them are always instructive and inspiring. Their technical and clinical expertise and generous personality have a great influence on me as well as me research work.

Special thanks go to our onsite Siemens scientists, Dr. Xiaoming Bi, and Dr. Fei Han. They have walked me through the process of sequence programming and offered me with numerous help during my practice. I truly appreciate their generous sharing of their knowledge and experience in sequence development. Having them as colleagues and friends is truly luck of me.

I wouldn't have achieved what I have in my research without the help from our clinical collaborators Dr. Stephen Pandol, Dr. Srinivas Gaddam, Dr. Simon Lo, Dr. Andrew Hendifar, Dr. Stephen Shiao, Dr. Richard Tuli, Dr. Wensha Yang from Cedars-Sinai Medical Center, Dr. Wei Yu from Anzhen Hospital in China, Dr. Iksung Cho, Dr. Mi Sun Chung from Chung-Ang Hospital in Korea, and Dr. Hyukjae Chang, Dr. Sangeun Lee from Yonsei University in Korea. They provided me with their valuable clinical insights, which immensely influence my overall research design.

I would like to specially thank Dr. Rola Saouaf, Dr. Lixia Wang, and Dr. Yu Guo, who provide their professional reading on our clinical data. I have learned a lot from them.

My sincerest thanks go to the entire Biomedical Imaging Research Institute family including but not limited to faculty (Dr. Rohan Dharmakumar, Dr. Shawn Wagner, Dr. Behzad Sharif, Dr. Wei Gao, Dr. Hui Han, and our previous member, Dr. Christopher Nguyen, Dr. Jianing Pang, Dr. Randy Yang), who have inspired me with their expertise; MRI technologists, nurses, and coordinators at imaging core (Laura Smith, Ed Gill, Jerry Zinch, Joselyn Ricafrente, and Laura Chey), and support research staff (Mary Eileen Da Vido, Karen Gutierrez, Joceline Mota, Natalin Aroyan, Rhona littman, Grant Dagliyan, Gloria Arrenquin), who have made it much easier to conduct

research. I would like to specially thank my fellow graduate students and dearest friends Dr. Jaime Shaw, Dr. Zixin Deng, Dr. Zhengwei Zhou, Xingmin Guan, Yuhua Chen, Eric Johnson, Pei Han, Zhehao Hu, Xinheng Zhang, Tianle Cao, who make the five years a lot of fun. We discuss research, we go to conference together, we share lots of precious memories.

It is hard to say how grateful I am to my parents, Jie Liu and Dejun Wang, who have been unconditionally loving me and supporting me throughout my life. Their love and support is my strongest backup and motivation to pursue my career. Last and most importantly, I would like to thank my husband, Sen Ma. We joined Dr. Li's group in the same year, we are colleagues, best friends, and the love of life for each other. We have been discussing MRI, solving problems of research, sharing important thoughts and feeling, learning from and supporting each other for the past five years, and will be in the future career and life.

VITA

Education:

- **M.S.**, Department of Bioengineering, University of California, Los Angeles (2017)
- **B.S.**, Department of Electrical Engineering, Peking University, China (2015)

Journal Publications:

- **Wang N**, Christodoulou AG, Xie Y, Wang Z, Deng Z, Zhou B, Lee S, Fan Z, Chang H, Yu W, Li D. Quantitative 3D dynamic contrast enhanced (DCE) MR imaging of carotid vessel wall by fast T1 mapping using Multitasking. *Magn Reson Med*, 81(4) (2019), pp.2302-2314.
- **Wang N**, Gaddam S, Wang L, Xie Y, Fan Z, Yang W, Tuli R, Lo S, Hendifar A, Pandol S, Christodoulou AG, Li D. Six-dimensional quantitative DCE MR Multitasking of the entire abdomen: Method and application to pancreatic ductal adenocarcinoma. *Magn Reson Med*, 84(2) (2020), pp.928-948
- Christodoulou AG, Shaw JL, Nguyen C, Yang Q, Xie Y, **Wang N**, Li D. Magnetic resonance multitasking for motion-resolved quantitative cardiovascular imaging. *Nat Biomed Eng* 2(4) 2018, p.215.
- Ma S, Nguyen CT, Han F, **Wang N**, Deng Z, Binesh N, Moser FG, Christodoulou AG, Li D. Three-dimensional simultaneous brain T1, T2, and ADC mapping with MR Multitasking. *Magn Reson Med* 84, no. 1 (2020): 72-88.
- Wang L, Gaddam S, **Wang N**, Xie Y, Deng Z, Zhou Z, Fan Z, Jiang T, Christodoulou AG, Han F, Lo SK, Wachsman AM, Hendifar A, Pandol S, Li D. Multiparametric Mapping Magnetic Resonance Imaging of Pancreatic Disease. *Front Physiol* 11, p.8. 2020.
- Hu Z, Christodoulou AG, **Wang N**, Shaw JL, Song SS, Maya MM, Ishimori ML, Forbess LJ, Xiao J, Bi X, Han F, Li D, Fan Z. Magnetic resonance multitasking for multidimensional assessment of cardiovascular system: Development and feasibility study on the thoracic aorta. *Magn Reson Med* (2020) in press.

Selected Conference Publications

- **Wang N**, Xie Y, Wang L, Ma S, Shiao SL, Christodoulou AG, Li D. Low-Dose, High-Temporal-Resolution Dynamic Contrast Enhanced MRI With Dynamic T1 Mapping Using Multitasking: An Initial Study on Breast Cancer. *In Proceedings of the Annual Meeting of ISMRM, Paris, France, 2020*. Abstract 7105.
- **Wang N**, Christodoulou AG, Xie Y, Han Fei, Zhong X, Ma S, Bi X, Deshpande V, Li D.

Three-Dimensional Free-breathing Whole-Liver Simultaneous T1, R2*, and Fat-Fraction Quantification Using MR Multitasking. *In Proceedings of the Annual Meeting of ISMRM, Paris, France, 2020*. Abstract 6996.

- **Wang N**, Gaddam S, Wang L, Xie Y, Fan Z, Lo S, Pandol S, Christodoulou AG, Li D. Six-Dimensional Quantitative DCE MR Multitasking in the Characterization of Pancreatic Ductal Adenocarcinoma Versus Chronic Pancreatitis. *In Proceedings of the Annual Meeting of ISMRM, Paris, France, 2020*. Abstract 7091.
- **Wang N**, Cho I, Chung MS, Lu M, Chang HJ, Christodoulou AG, Li D, Xie Y. Quantitative Multi-Contrast Atherosclerosis Characterization (qMATCH): Initial Clinical Study of Plaque Analysis. *In Proceedings of the SCMR, Orlando, FL, USA, 2020.* Abstract 749492.
- **Wang N**, Christodoulou AG, Gaddam S, Wang L, Xie Y, Deng Z, Zhou Z, Yang W, Fan Z, Tuli R, Lo S, Hendifar A, Pandol S, Li D. Whole-abdomen Free-breathing Quantitative Dynamic Contrast Enhanced (DCE) MR Imaging of Pancreatic Ductal Adenocarcinoma (PDAC) with Fast T1 Mapping Using Multitasking: A Pilot Study. *In Proceedings of the Annual Meeting of ISMRM, Montreal, Canada, 2019*. Abstract 1722.
- **Wang N**, Christodoulou AG, Xie Y, Deng Z, Zhou B, Fan Z, Li D. Joint Reconstruction of Images with Different Temporal Basis in Carotid Vessel Wall Imaging. *In Proceedings of the Joint Annual Meeting of ISMRM-ESMRMB, Paris, France, 2018*. Abstract 8870.
- **Wang N**, Christodoulou AG, Xie Y, Deng Z, Zhou B, Fan Z, Yu W, Li D. High Spatiotemporal Resolution Dynamic Contrast Enhanced (DCE) For Assessing Vascular Inflammation: Initial Clinical Experience. *In Proceedings of the Joint Annual Meeting of ISMRM-ESMRMB, Paris, France, 2018.* Abstract 4157.
- **Wang N**, Christodoulou AG, Xie Y, Deng Z, Zhou B, Yu W, Li D. Fully Quantitative 3D Dynamic Contrast Enhanced (DCE) CMR of Carotid Vessel Wall by Fast T1 Mapping. *In Proceedings of the CMR 2018, Barcelona, Spain, 2018.* Abstract 372017.

Awards:

- ISMRM Merit Award (Magna Cum Laude): Whole-abdomen Free-breathing Quantitative Dynamic Contrast Enhanced (DCE) MR Imaging of Pancreatic Ductal Adenocarcinoma (PDAC) with Fast T1 Mapping Using Multitasking: A Pilot Study. 27th Annual ISMRM Scientific Meeting and Exhibition, Montreal, Canada, 2019.
- UCLA Bioengineering Department first-year fellowship 2015-2016

CHAPTER 1: INTRODUCTION

1.1 Significance

Dynamic contrast enhanced (DCE) MRI, as a promising imaging tool, has been widely explored in many clinical aspects for noninvasive characterization of diseases[1,2]. It typically involves the fast acquisition of images before, during and after the intravenous injection of MRI contrast agent (CA). The changes of signal intensity over time depend on the spatial and temporal distributions of CA transit, which carries the information of tissue perfusion, microvascular density, permeability, and volume of extracellular extravascular space (EES)[3-5]. This information can be used to evaluate the functionality, in addition to the anatomy, of the organ. Besides, the changes in functional properties is recognized to precede the morphological alterations, which can potentially provide an avenue for early diagnosis and treatment evaluation[6,7]. Currently, DCE MRI plays an important role in the evaluation of various organs and diseases including but not restricted to heart failure, renal rejection, atherosclerosis, multiple sclerosis, and various kinds of tumors (brain, breast, prostate, liver, pancreas, etc.), showing great ability in the diagnosis, characterization, staging, and treatment monitoring. However, some major technical challenges continue to limit the exploiting of its clinical value. With the advanced imaging and reconstruction technologies in recent years, the development of novel DCE MRI techniques to overcome the limitations and further realize its ability in clinical practice is of great significance.

1.2 Current States of DCE MRI

DCE MRI typically involves the acquisition of sequential T1-weighted (T1W) images during the passage of an intravenous gadolinium-based CA (GBCA) within the tissue of interest[8]. GBCAs are paramagnetic, appearing to shorten the T1 relaxation time in the tissues. The reduction of the T1 values (or the enhancement of T1W signal intensity) are related to distribution of CA concentration, which depends on the functional characteristics such as vascular properties of the tissues. By analyzing the signal enhancement pattern, these functional characteristics can be assessed. The protocols and analysis methods of DCE MRI vary in different applications or organs.

1.2.1 Qualitative DCE MRI

Qualitative DCE MRI is the most readily accessible approach and has been most widely applied to standard clinical exams[9]. It relies on the morphologic criteria on the contrast enhanced images and shape of the signal intensity versus time curve for disease detection. Malignant tumor usually appears bright on the early post-contrast phases and bears a signal intensity curve with fast wash-in and wash-out.

DCE MRI is a crucial part of standard clinical protocol for breast cancer. It acquires 3D T1W gradient-echo (GRE) images with voxels smaller than $1\times1\times3$ mm^3. Each DCE phase takes up to 1 to 2 minutes. Previous studies have shown that DCE MRI has the highest sensitivity, which is close to 100%, among all the imaging modalities in the diagnosis of breast tumor[10-13].

In prostate cancer, DCE MRI shows moderate sensitivity (~0.52) but high specificity (~0.89) in the diagnosis of prostate cancer, both of which are higher than standard T2W imaging (0.52 and 0.73, respectively)[14]. High accuracy was reported using

DCE MRI in detecting cancer recurrence on patients who have undergone radical prostatectomy.

DCE MRI is also an essential component for clinical practice of pancreatic ductal adenocarcinoma (PDAC). It acquires 3D T1W GRE images at pre-contrast phase, arterial phase (20-40 s after the start of injection), venous phase (45-65 s), and equilibrium phase (3-5 min), each of which is within one breath-hold. PDAC mass usually presents hypo-enhancing on arterial phase due to the reduced microvascular density within the tumor[15,16]. Investigations suggested that DCE MRI has superior accuracy in the detection of PDAC compared to clinical standard MDCT, especially with small tumors (<=1.5 cm)[16].

1.2.2 Semi-quantitative DCE MRI

Semi-quantitative DCE MRI measures the shape of the curve instead of visually assessment. The frequently-used parameters includes the area under the concentration -versus-time curve (AUC) for the first 60 seconds or 120 seconds after the initiation of the enhancement, time to the contrast peak (TTP), peak enhancement, maximum slop of the curve, initial enhancement rate, and signal enhancement ratio (SER)[1,9,17,18]. Abe et al. showed that some of the semi-quantitative parameters are capable of differentiating malignant and benign breast tumors[3]. Medved et al. suggested that semi-quantitative DCE MRI analysis showed low variability and was able to detect the change in tumors during therapy[19].

Semi-quantitative analysis relies less on experienced readers as well as has increased robustness to intra- or inter- observer variability. However, this approach is still sensitive to the variation in signal intensity, which can be subject to coil positioning, etc.

Moreover, these descriptive parameters provide no physiological insight to the behavior of the microenvironment within the lesions.

1.2.3 Quantitative DCE MRI

Other than directly analyzing the shape of the curve, quantitative approach is based on the modeling of the CA concentration of tissues of interest as dependence of the arterial input function (AIF) and vascular properties. By applying proper pharmacokinetic (PK) model, some imaging markers such as fractional plasma volume (v_p), transfer constant between plasma and EES (forward rate from plasma to EES: K^{trans}, and reverse reflux rate: k_{ep}), and the fractional volume of EES (v_e), can be fitted based on the CA concentration curves[1].

Quantitative approach requires higher temporal resolution for the sampling of DCE phases for better capture of the dynamics of CA concentration, which has been a technical challenge limiting its application in current clinical practice[20,21]. In recent years, with the advances in imaging technique, an increasing number of investigations have been conducted using quantitative DCE MRI to study the vascular properties of a variety of pathological tissues. The correlation between the PK parameters and the histological markers including microvascular density and fibrosis has been reported in different tissues[22-27]. Zhang et al. found that PK parameters are able to differentiate low- and high-grade gliomas with histopathology as gold standard[28]. The value of quantitative DCE MRI in monitoring therapy response have also been investigated in various diseases[5,29-34].

1.3 Major Technical Challenges for Quantitative DCE MRI

Compared to qualitative and semi-quantitative approaches, quantitative approach possesses the morphological and curve information, and can additionally provide the characteristics of the microenvironment, which can maximize the utility of DCE MRI in the evaluation of the functionality of the tissues of interest. The pharmacokinetic model is theoretically more robust to dose, injection rate, and signal variation caused by coil positioning. However, demanding technical challenges continue to hamper its wide application in clinical practice.

1.3.1 Coverage and resolution

The pathological structure of lesions is usually heterogeneous in most of the diseases targeted by quantitative DCE MRI. Usually 3D coverage of the entire anatomical structure is necessary. The lesions can be rather small (for instance, the diameter of the targeted tumor can be less than 1 cm) and heterogeneous, which requires a high spatial resolution on order of 1 mm, even submillimeter in some applications. To capture the rapid-changing dynamics of CA for accurate kinetic modeling, a temporal resolution, which is the acquisition time for each DCE phase, less than or on order of 10 second is preferable[35]. However, these requirements are in direct conflict with conventional imaging techniques. In most cases, compromises among coverage, spatial resolution and temporal resolution have to be made.

1.3.2. Physiological motion

In cardiac or abdominal imaging, the artifacts induced by physiological motion is one of the major sources to reduce image quality and then affect the quantification. ECG-

gated or respiratory-triggered acquisition is an option to alleviate the motion artifacts, but can lead to even longer scan time for each DCE phase, which worsen the conflict among the coverage and spatial/temporal resolution. In abdominal study, acquisition with breath-holding is the most common way to deal with respiratory motion. However, this can be unreliable and infeasible in some patient cases.

1.3.3 Nonlinearity between signal intensity and CA concentration

According to the relaxivity of the alteration in the R1 values and the CA concentration, dynamic T1 (R1) mapping is the most reliable way to quantify the CA concentration. However, dynamic T1 (R1) mapping requires the multiple images to be acquired with different inversion times (TIs) or flip angles (FAs) at each DCE phase, which is usually impractical given the abovementioned sampling conflicts. Most existing DCE techniques linearly transform the dynamic signal intensity from T1W MRI to estimate CA concentration for kinetic modeling. However, the nonlinearity between T1W MRI signal and CA concentration can introduce errors in the quantification of kinetic parameters, especially in tissues with high contrast uptake such as blood. Another approach is to nonlinearly calculate the CA concentration based on a separately acquired pre-contrast T1 map and dynamic T1W signal, but this requires an additional scan and is subject to misregistration between separate imaging series[36,37].

1.4 Concern to GBCA Deposition

All GBCAs used in DCE MRI are non-toxic, extracellularly distributed, excretable contrast agent[38]. Current standard dose for clinical and research use is 0.1 mmol/kg,

which was determined in 1980s after the initial pre-clinical and clinical experience due to the balance between in vivo tolerance and effectiveness in imaging[39,40]. Recently, the safety of the use of GCBAs has been brought to public attention due to the findings that Gd can deposit in brain and other body parts in patient with normal renal function[41-43]. Although the long-term clinical consequences of Gd deposition remains unknown, the benefit and risk of the usage of GBCA in clinical activities can be controversial. Studies indicated that the accumulation of Gd is dose-dependent that high deposition tend to appear in patients who receive larger cumulative dose[42], suggesting that reduced dose may lower the potential risks caused by Gd deposition. Therefore, to develop novel imaging technique that can use lower GBCA dosage without losing the diagnosis power would be a preferable way to alleviate the concern while taking advantages of crucial clinical information provided by DCE MRI.

1.5 Objective

The broad, long-term goal of the project in the dissertation is to develop a novel quantitative DCE MRI technique using Multitasking framework that can achieve 1) motion-resolved imaging with free-breathing acquisition and bulk-motion correction, 2) high spatial-temporal resolution with 3D anatomical coverage for simultaneous perfusion and permeability quantification, 3) dynamic T1 quantification for accurate quantification of CA concentration and potentials for reduced GBCA dose. The overall objective is split into 3 specific aims.

1.5.1 Aim 1: To develop a novel quantitative DCE MRI technique, Multitasking DCE, for the characterization of carotid atherosclerosis that achieves dynamic T1 quantification with the coverage of entire carotid arteries, 0.7 mm isotropic resolution, and 1.2-second temporal resolution.

Chapter 3 presents the novel quantitative DCE MRI technique developed based on MR Multitasking, which uses a low-rank tensor (LRT) imaging model to exploit the high correlation between multiple time dimensions and thus achieves a vastly accelerated acquisition. A bulk motion detection and removal scheme were incorporated into the Multitasking DCE framework to improve the image quality. The feasibility of the technique was tested on both phantom, volunteer, and patient studies.

1.5.2 Aim 2: To develop a 6D Multitasking DCE for abdominal imaging with respiratory-motion-resolved, 1-second temporal resolution dynamic T1 mapping of the entire abdomen.

A respiratory dimension was added to the Multitasking DCE framework developed in Aim 1 to resolve the respiratory motion, achieving free-breathing acquisition and motion-resolved reconstruction. As described in Chapter 4 & 5, this technique was tested on 16 healthy volunteers, 14 patients with PDAC, and 10 patients with chronic pancreatitis (CP), showing the feasibility to characterize normal pancreas, tumor and non-tumoral regions in PDAC patients, and CP.

1.5.3 Aim 3: To develop the Multitasking DCE using 20% of standard GBCA dose for breast cancer detection and characterization.

In Chapter 6, the Multitasking DCE was improved for the imaging of breast, achieving an entire-breast coverage, ~1mm spatial resolution, and 1.4-second temporal resolution dynamic T1 quantification. The repeatability of kinetic parameters estimated using Multitasking DCE using 20% of standard dose and the correlation between the parameters estimated using 20% dose or standard dose were evaluated. A patient study was conducted using low-dose Multitasking DCE and standard-dose clinical DCE, showing that the low-dose Multitasking DCE presents excellent image quality and equivalent diagnosis power compared to clinical DCE, which suggests that low-dose Multitasking DCE is feasible in the detection of breast cancer.

CHAPTER 2: BACKGROUND

2.1 Basic Theory of DCE MRI

2.1.1 Angiogenesis

DCE MRI is targeted to evaluate the vascular properties in pathological lesions[34]. Blood vessels serve oxygen and nutrients for mammalian cells, which is vital to their life maintenance. Active cells usually locate within a few hundred micrometers of capillaries due to the diffusion limit for the oxygen[44]. To support the growth of multicellular organisms beyond their current size, new vessels have to be formed, which is referred to as angiogenesis.

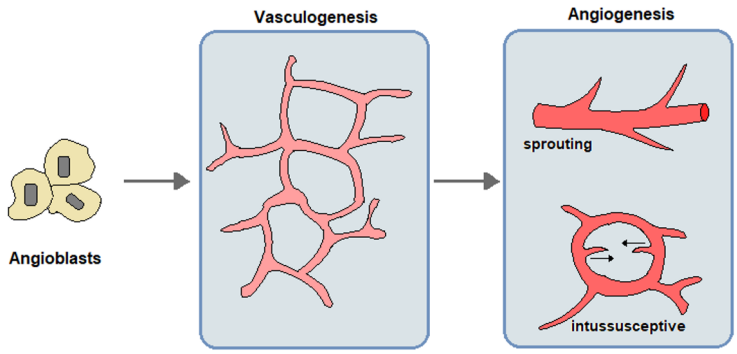


Figure 2.1 Basic types of primary vascular growth. Redrawn after Carmeliet and Collen (2000)

The phenomenon of angiogenesis was first observed by John Hunter in 1794, suggesting a proportionality between the vascularity and metabolic requirements in both health and disease[45]. This phenomenon has been studied and investigated over centuries and plenty of progress has been made. Under modern terminology, vessels in an embryo are originated and differentiated from angioblast, referred to as vasculogenesis; angiogenesis is responsible for the remodeling and expansion of the vascular network, occurring throughout lifetime[46]. There are two types of angiogenesis, sprouting angiogenesis and intussusceptive angiogenesis. Sprouting angiogenesis is the based on

endothelial cell migration, proliferation and tube formation[46], while intussusceptive angiogenesis involves the splitting of existing vessels[45]. Figure 2.1 demonstrated the basic morphological events of both types[45]. In normal physiological process, such as tissue growth, wound healing, etc., angiogenesis is under hierarchy and stringently regulated by an extensive variety of angiogenic stimulator and inhibitor[47].

The observation of the occurrence of angiogenesis around tumors was made nearly 100 years ago. However, the study of the relation between angiogenesis and tumor and other diseases had not been intensified until 1971 when Folkman proposed the hypothesis that tumor growth is angiogenesis-dependent and hence blocking angiogenesis could be a strategy to arrest tumor growth[48]. Investigations have revealed that the angiogenesis involved in pathological process is structurally and functionally abnormal. First, the vasculature in pathological tissues is highly disorganized. The vessels are tortuous and dilated, with uneven diameter, excessive branching and shunts[44]. As a result, the blood flow is chaotic, leading to hypoxic regions, which can be a major driven factor of further rise of angiogenesis. Second, these neovessels are usually immature[49]. Their vessel walls usually have endothelial fenestrae, widened interendothelial junctions, and discontinuous basal membrane, or absent of mural cells, which accounts for increased permeability of the vessels. The differences in the density and permeability in the vessels are crucial characteristics to differentiate pathological and normal tissues. Since the abnormal angiogenesis occurs along with the entire pathological process, the detection of changes in the vascular properties also provide a possible way for the early diagnosis of disease.

The properties of the vasculature alter in a complex way during the treatment[50]. On the other hand, due to the key role angiogenesis plays in the progress of the disease, inhibiting angiogenesis to halt the development of disease has become a critical step in the therapy[51]. Various antiangiogenetic drugs and therapeutic strategies has been proposed or already in clinical trial for different type of disease[44,52]. A proper way to estimate the changes of vascular properties during treatment is crucial for the early assessment of the effect for current therapeutic regime, which is significant to optimize the therapy strategy individually and to improve the prognosis of diseases.

2.1.2 Gadolinium-based contrast agent (GBCA)

Due to the vital role angiogenesis plays in the progress of extensive types of diseases, imaging approaches that can reliably and non-invasively evaluate the vascular properties in vivo would be able to provide crucial information for diagnosis, staging, and treatment monitoring. Among the many imaging techniques developed for this purpose, the dynamic contrast enhanced (DCE) imaging, which analyze tracer kinetics of intravenously injected CA, is the most widely used scheme for various imaging modalities including ultrasound, CT, and MRI[53]. The changes in the density and permeability of the vessels lead to a different temporal distribution of the CA concentration within the pathological tissues compare to normal. The signal intensities of different tissues are altered proportionate to the CA concentration, resulting in a differentiated enhancement pattern. Compared to other imaging modalities, MRI is superior in the excellent soft tissue contrast without the exposure to radiation. DCE MRI has been flourishing and widely

applied in the study of various diseases since mid 1980s, almost immediately after the idea of DCE was introduced to imaging field.

The phenomenon that proton relaxation time, known as T1 and T2/T2* in MRI, can be influenced by the presence of paramagnetic ion was realized in late 1970s, shortly after the generation of the first MRI images at 1973[39]. Paramagnetic ion has unpaired electrons in the outer orbital shells. When exposed to magnetic field, those electrons can create large fluctuating magnetic field experienced by surrounding protons due to the 700 times larger magnetic moment of an electron compared to a proton[54]. When the frequency of this fluctuation has a component close to the Larmor frequency, the relaxation of the nearby proton will be enhanced.

Efforts has been made to search for proper ion and complexes that are effective in altering relaxation time as well as clinically stable and in vivo non-toxic. In 1981, Weinmann et al. recognized that Gd^{3+} was the most effective paramagnetic ion in terms of reducing T1[38]. Gd^{3+} has seven unpaired electrons. However, Gd^{3+} itself is rather toxic and need to be incorporated in a ligand as chelate in either linear or macrocyclic structure[39]. The first Gd chelate injected on a human volunteer was gadopentetate dimeglumine in 1983[55]. Till now, various type of GBCA has been FDA approved for in vivo use, such as Gd-DTPA. GBCAs are with small molecular weight so that they can diffuse from the plasma into the extracellular fluid. They are biologically inert, so they do not participate in metabolic activities. Most of them are not taken up by cells and are excreted by kidney, with exceptions of a few liver-specific CAs, such as Gd-EOB-DTPA, that can be partially taken up by hepatocytes and eliminated by hepatobiliary system.

The efficiency of GBCAs to alter the proton relaxation times is termed relaxivity, which depends on their individual chemical properties and extrinsic factors including temperature, magnetic field strength and the tissue surroundings. The relation between the CA concentration and relaxation time is shown as Equation 2.1:

$$R_{1,2} = \frac{1}{T_{1,2}} = R_{1,2}^{0} + r_{1,2}C, \tag{2.1}$$

Where $R_{1,2}^{0}$ are the pre-contrast relaxation rate for T1 and T2, C is the molar concentration for CA, and $r_{1,2}$ are the relaxivity rate for T1 and T2, respectively. With standard clinical dose at 0.1 mmol/kg body weight or lower, T1 relaxivity effect dominate. Table 2.1 summarizes the common relaxivity rate for different GBCAs.

Table 2.1 GBCA relaxivity rate

	Gadavist (Gd-BT-DO3A)	Magnevist (Gd-DTPA)	Eovist Gd-EOB-DTPA)	MultiHance (Gd-BOPTA)
Company	Bayer	Bayer	Bayer	Bracco
Dose (mmol/kg)	0.1	0.1	0.05	0.1
Concentration (M)	1.0	0.5	0.25	0.5
Structure	Macrocyclic	Linear	Linear	Linear
Relaxivity (r1/r2,1.5T)	5.2/6.1	4.1/4.6	6.9/8.7	6.3/8.7
Relaxivity (r1/r2,3T)	5.0/7.1	3.7/5.2	6.2/11	5.5/11.0
Clearance	Renal	Renal	Renal & hepatic	Renal & hepatic

All the FDA-approved GBCAs are non-toxic and stable in vivo. The incidence to acute adverse drug reaction of GBCAs appear to be very low, much lower than those reported for non-ionic iodinated contrast media for X-ray and CT. A risk for GBCAs is the possibility to induce nephrogenic systemic fibrosis (NSF), which is rare but potentially fatal disorder in patient with end-stage renal disease[56]. Studies have found that GBCAs with macrocyclic structure are at lower risk for the development of NSF. The reported

incidence for NSF has been decreased in recent year, possibly attributed to great awareness of at-risk patient and the widespread use of macrocyclic agents[57,58].

Another concern toward GBCAs recently is the deposition of gadolinium in human body (brain, bone, etc.) in subjects with normal renal function. Studies have also reported that the amount of the Gd deposition is related to the cumulative dose received previously. The clinical consequence of Gd deposition is not yet clear. Further investigation is warranted into the biodistribution of gadolinium and effect of Gd deposition.

2.1.3 Imaging principles

DCE MRI involves the fast acquisition of sequential T1W images during the passage of intravenous GBCA in the regions of interest (ROIs). The vascular properties within the ROI are reflected by the distribution of CA concentration, and consequently the enhancement pattern of the T1W signal intensity. The typical injection rate of CA is 1 to 4 mL/s. The acquisition time course of a DCE MRI study is usually between 5 to 10 minutes after the CA administration[9]. The CA concentration curve in the blood plasma, which is so-called arterial input function (AIF), changes rapidly within the first 20 to 60 seconds, varying individual by individual. The contrast kinetics in other tissues usually changes slower. Figure 2.2 shows a typical example of the AIF and CA concentration curve of a tissue.

The detailed protocol for DCE MRI varies for different applications due to the requirements for coverage, spatial resolution, and temporal resolution, which is the scan time for each DCE phase. Pathological tissues are usually heterogeneous in their properties, which usually requires high spatial resolution. An adequate temporal

resolution would also be preferable to acquire the fast-changing dynamics of CA concentration. Many diseases desired by DCE MRI can be multi-centric, such as cancer, so sufficient spatial coverage is also significant for accurate evaluation. However, these requirements are in direct conflict. Compromises usually have to be made depend on particular applications[59].

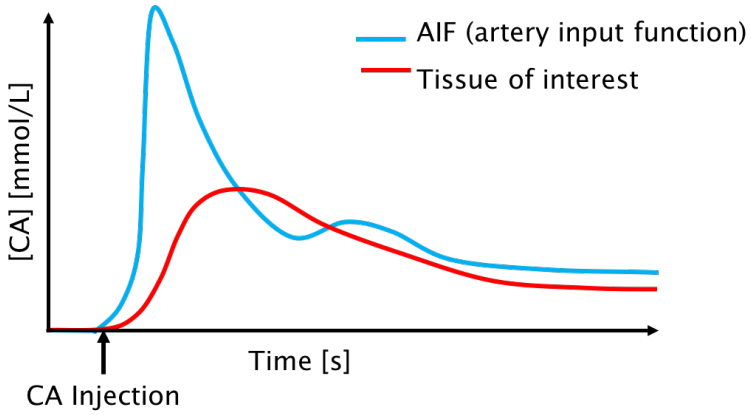


Figure 2.2 Illustration of CA concentration curves for AIF and tissues of interest

2.2 Image Analysis

DCE MRI carry both morphological and functional information of pathological tissues. As briefly introduced in Chapter 1, there are generally three approaches to analyze images from DCE MRI: qualitative, semi-quantitative, and quantitative. Qualitative approach is the most readily accessible but least standardized method. Quantitative approach is the most complex but most generalizable method. In between is the semi-quantitative approach[1,9,17,18].

2.2.1 Qualitative approach

Qualitative approach relies most on visually assessing the contrast changes on the gray-scale post-contrast images. In most cases, micro vessels in pathological tissues has

high density and permeability, resulting in easier exchange of the CA between capillaries and EES. Those tissues appear bright on the early post-contrast images. Another way is to evaluate the pattern of the signal intensity curve versus time. The signal of pathological tissues usually has rapid and high enhancement at early phases followed by a relative rapid decline compared to slower but continuously signal enhancement of normal tissues. The shape of dynamic enhancement curves is divided into three categories after initial uptake, as shown in Figure 2.3: type 1, persistent increase; type 2, plateau; type 3: wash-out[60]. Type 3 is considered as the most suspicious for lots of malignant cancers, such as breast cancer and prostate cancer. However, there are exceptions. For example, the signal of PDAC, due to its low vascular density within the tumor, has slow and persistent enhancement pattern as type 1. The diagnosis should be made based on the practice for each individual disease.

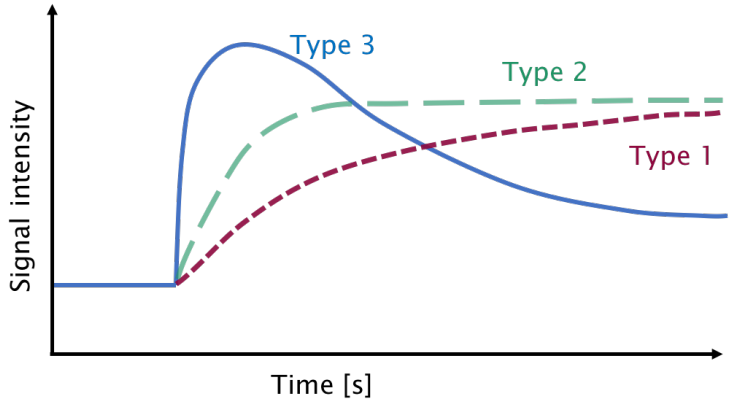


Figure 2.3: Common categories of the types of signal enhancement curve: type 1, persistent increase; type 2, plateau; type 3: wash-out

Qualitative analysis is visual assessable and model-free, which is the most readily accessible approach and has been widely applied clinically. However, the analysis is inherently subject to the factors affecting signal intensity, such as coil positioning and

inter-scanner variability, which makes it difficult for multi-center meta-analysis or longitudinal follow-up.

2.2.2 Semi-quantitative approach

Instead of visually assessment of the morphology or enhancement pattern, semi-quantitative approach defines some parameters that can quantitatively evaluate the shape of the enhancement curve. The enhancement curve used in semi-quantitative analysis are typically relative enhancement curve as shown in Equation 2.2:

$$c_{\mathrm{rel}}(t) = \frac{s(t) - s(0)}{s(0)}, \tag{2.2}$$

where $s(0)$ is the pre-contrast signal intensity, $s(t)$ is the signal intensity at time point t, and $c_{\mathrm{rel}}(t)$ is the relative enhancement curve at time point t. Figure 2.4 displays a representative relative enhancement curve and typical semi-quantitative parameters. Time-to-peak (TTP), which equals to $t_{\max} - t_{\mathrm{ini}}$, where t_{ini} is the initial enhancement time and $t_{\max}$ is the peak enhancement time. Peak enhancement $c_{\mathrm{rel,max}}$, which is the value of c_{rel} at $t_{\max}$. Signal enhancement ratios (SER) is defined as $c_{\mathrm{rel}}(t_{\max})/c_{\mathrm{rel}}(t_{\mathrm{delay}})$, where t_{delay} is the time of delayed phase, which may vary for different applications. Area under CA concentration versus time curve (AUC) is also an easily accessible parameter. The AUC for the first 60 seconds, 90 seconds, or 120 seconds (denoted as AUC_{60}, AUC_{90}, AUC_{180}) after the initial enhancement are most commonly used[1,9,17,18].

Semi-quantitative approach is also easy to apply and has been adopted in a large number of studies. Abe et al. showed that semi-quantitative parameters are capable of differentiating benign and malignant breast tumor[3]; Medved et al. suggested that semi-quantitative DCE MRI analysis showed low variability and was able to detect the change

in tumors during therapy[19]. Dijkhoff et al. found there is correlation between semi-quantitative parameter and quantitative parameters in rectal cancer[61]. However, semi-quantitative can be sensitive the factors affecting signal intensity, such as acquisition protocols or injection scheme. Moreover, these descriptive parameters are not capable of providing direct information on the vascular properties of the pathological tissues.

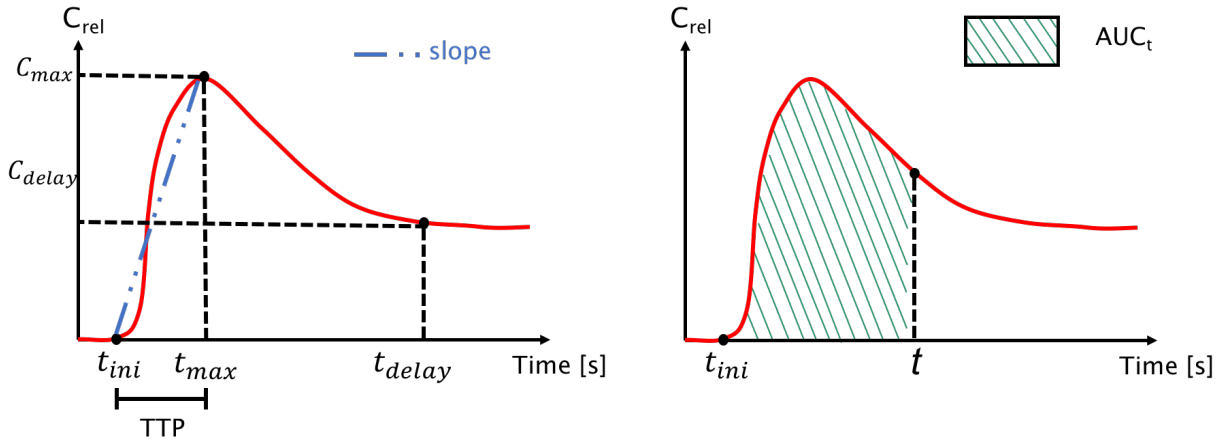


Figure 2.4: Illustration of semi-quantitative parameters.

2.2.3 Quantitative approach

Quantitative approach assesses the vascular properties using pharmacokinetic (PK) model. The idea was first developed in early 1990s separately by Larsson, Tofts, Brix and colleagues as a means to evaluate the permeability of blood-brain barrier[62-64]. In 1999, a consensus on the early models with standard quantities and symbols was made, yielding the well-known Tofts-Kermode (TK) model[65]. With the CA concentration of plasma and tissues of interest, some imaging markers representing vascular properties such as fractional plasma volume (v_p), transfer constant between plasma and EES (forward rate from plasma to EES: K^{trans}, and reverse reflux rate: k_{ep}), and the fractional volume of EES (v_e), can be quantified. Numerous investigations using TK model to estimate vascular properties sprang up, particularly in the field of oncology[20,21]. In the

following decades, with the growing number of research into the study of vascular properties as well as the development in MRI hardware and acquisition techniques especially the increase SNR and temporal resolution, models that are more generalized and can incorporate more physiological characteristics not embedded in the early models, such as perfusion (F_p) and product of permeability-surface area (PS), have been proposed. The 2-compartment exchange model (2CXM) is an example of the generalized model. The details of the PK modeling are discussed in the next section.

2.3 Pharmacokinetic Model

2.3.1 Estimating CA concentration

Almost all model-based DCE analysis requires the determination of CA concentration curves $C(t)$ for the tissue of interest, denoted as $C_{\mathrm{t}}(t)$, and the blood plasma, denoted as $C_{\mathrm{p}}(t)$. The straightforward way is to calculate $C(t)$ from dynamic T1 mapping using Equation 1 in section 2.1.2. However, due to the practical sampling difficulties for high-temporal-resolution T1 mapping, T1W images instead of T1 maps are usually used for the estimation of $C(t)$. The T1W signal intensity $S(t)$ using SPGR sequence at time point t with $R_1(t) = 1/T_1(t)$ is given by:

$$S(t) = A\frac{1 - e^{-T_{\mathrm{R}} \cdot R_1(t)}}{1 - e^{-T_{\mathrm{R}} \cdot R_1(t)} \cos\alpha} \sin\alpha, \tag{2.3}$$

With amplitude A, SPGR readout interval T_{R}, and flip angle α. There are two approaches to convert $S(t)$ to $C(t)$, linear approach and non-linear approach.

Linear approach

Short T_{R} (<=10ms) are usually used for fast acquisition. Assuming that $T_{\mathrm{R}} \ll T_1(t)$, or $T_{\mathrm{R}} \cdot R_1(t) \ll 1$ always hold true, then there is $e^{-T_{\mathrm{R}} \cdot R_1(t)} \approx 1 - T_{\mathrm{R}} \cdot R_1(t) \approx 1$. Equation 2.3 can be simplified as

$$S(t) = A \cdot T_{\mathrm{R}} \cdot R_1(t) \cdot \sin \alpha \tag{2.4}$$

Given $S(0)$ and pre-contrast $R_1(0)$, $C(t)$ can be calculated as:

$$C(t) = \frac{1}{\gamma}\big(R_1(t) - R_1(0)\big) = \frac{R_1(0)}{\gamma}\frac{S(t) - S(0)}{S(0)} \tag{2.5}$$

With dynamic T1W signal intensity $S(0)$ and $S(t)$, and $R_1(0)$ from the pre-contrast T1 map acquired ahead of time, the $C(t)$ can be easily assessed with linear approach.

One major drawback for this approach is that the assumption $T_{\mathrm{R}} \cdot R_1(t) \ll 1$ is invalid when $T_1(t)$ is largely shortened after contrast injection, particular in tissues with high contrast uptake such blood plasma where the post-contrast T1 can fall below 100 ms. In this situation, the nonlinearity between T1W signal intensity and CA concentration can introduce error in the following estimation of vascular parameters[1,66].

Nonlinear approach

Nonlinear approach is calculating post-contrast T1 values using the dynamic T1W signal intensity and pre-contrast T1 maps using Equation 2.3.

$$C(t) = \frac{1}{T_{\mathrm{R}} \cdot \gamma} \ln\left(\frac{S(0) - \cos\alpha \cdot S^* \cdot S(t)}{S(0) - S^* \cdot S(t)}\right) - \frac{R_1(0)}{\gamma}, \tag{2.6}$$

where $S^* = \frac{1 - e^{-T_{\mathrm{R}} \cdot R_1(0)}}{1 - e^{-T_{\mathrm{R}} \cdot R_1(0)} \cos\alpha}$. Nonlinear approach avoids the error introduced by linear assumption between T1W signal and CA concentration. However, each post-contrast T1 value $T_1(t)$ is calculated relying on one-point $S(t)$, which can be sensitive to noise in $S(t)$ and mis-registration of pre-contrast T1 maps.

2.3.2 AIF

AIF describes the dynamic CA concentration in the blood plasma. It is typically characterized by a sharp uptake, followed by a short-lived peak, and subsequently a longer wash-out period. AIF is required in almost all PK models. However, it is difficult to accurately determine AIF due to the issues including flow artifacts, inflow, partial volume effect and the rapid-changing nature. Previous studies have shown that a temporal resolution on order of 1 second is necessary for accurately estimating AIF, which is hard to achieve for most existing DCE techniques. Some applications adopt a population-based AIF instead of individually measured AIF for PK modeling, presuming small inter-subject variabilities. However, this assumption is usually invalid because the AIF can vary a lot from individual to individual. The inaccuracies caused by population-based AIF can lead to errors in PK estimation[1].

2.3.3 Vascular-interstitial exchange

The assumption that the physiological systems are linear and stationary systems forms the foundation for all tracer-kinetic models[20,21]. In the context of DCE MRI, the tracer (CA) is distributed over two tissue regions: the tissue blood plasma and interstitium, or EES, the exchange of CA is allowed in both directions. Figure 2.5 illustrates a generic architecture of this tissue type. Tissues with this architecture are characterized by four independent parameters, which can be combined to derive any other parameters. Here lists the most common parameters and interpretations.

Volumes

Parameters v_p and v_e are two independent parameters that measures the fractional volume of plasma and EES within the tissues. Both are dimensionless and the sum is the total volume of extracellular space, which much satisfy $v_p + v_e \leq 1$.

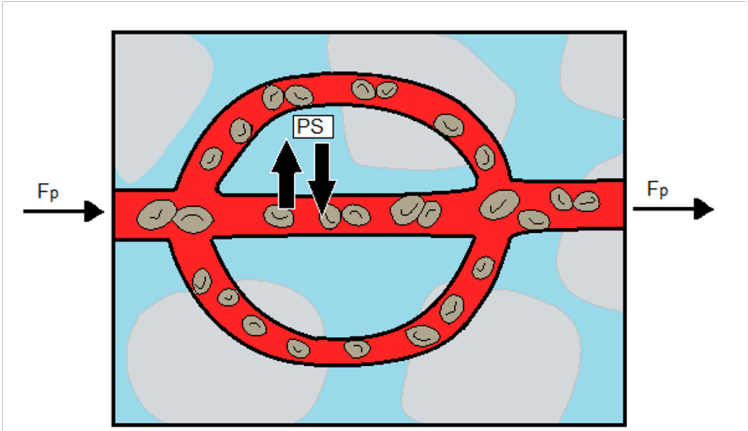


Figure 2.5: Scheme of two-region architecture and capillary-interstitium exchange

Flows

F_p is an independent parameter representing the inflow of the plasma per unit of tissue volume (ml/min/ml). Blood does not accumulate in the tissue so the venous outflow if also F_p.

Permeability-surface area product

PS measures the rate at which the CA leak out of the plasma with unit min^{-1}. More precisely, PS is the number of CA particles that transfer from plasma to interstitium per unit of time, tissue volume and tissue plasma concentration.

Mean transit time

When considering the extracellular space as a unity with plasma flow F_p as the only inlet, the mean transit time can be defined as:

$$T = \frac{v_p + v_e}{F_p} \tag{2.7}$$

The interstitum has a single inlet from the plasma, so the interstitial mean transit time is:

$$T_e = \frac{v_e}{PS} \tag{2.8}$$

And the capillary mean transit time is:

$$T_c = \frac{v_p}{F_p} \tag{2.9}$$

Extraction fraction

The extraction fraction E is the fraction of the CA particles extracted into the interstitium, defines as:

$$E = \frac{\int_0^\infty PSC_p(t)dt}{\int_0^\infty F_p C_a(t)dt} \tag{2.10}$$

with the CA concentration in the arteries $C_a(t)$. Given the relation between $C_p(t)$ and $C_a(t)$, the final expression for E is[20,21]

$$E = \frac{PS}{v_p} T_p \tag{2.11}$$

where T_p is the plasma mean transit time depend on the particular model chosen for the parameter estimation.

Transfer constant

Given the rate at which the CA particles are delivered to the capillary bed Fp and the extraction fraction E, the transfer constant K^{trans} can be easily defined as:

$$K^{trans} = EF_p \tag{2.12}$$

Table 2.2 summarizes the common parameters under this tissue architecture. Among them, F_p, v_p, v_e, and PS are the most common combination of four independent parameters to describe the vascular properties of the tissues.

Table 2.2: List of PK parameters

Symbol	Interpretation	Units	Formula
F_p	Plasma flow	ml/min/g	/
v_p	Fractional plasma volume	/	/
v_e	EES volume	/	/
PS	Permeability-surface area product	ml/min/g	/
E	Extraction fraction	ml/min/g	$PS/ (PS + F_p)$
K^{trans}	Transfer constant	1/min	$PS \cdot F_p /(PS + F_p)$
k_{ep}	EES-to-plasma rate constant	1/min	K^{trans}/v_e
T	Mean transit time	min	$(v_p + v_e)/ F_p$
T_e	EES mean transit time	min	v_e /PS
T_p	Plasma mean transit time	min	$v_p /(PS + F_p)$
T_c	Capillary mean transit time	min	v_p / F_p

2.3.4 Two compartment exchange model (2CXM)

Figure 2.5 illustrates the architecture of the tissue, but doesn't make any assumption on the CA distribution within each space, which is an indispensable step to PK modeling. One common assumption on the CA distribution is compartmental model, which assumes the specific region as a well-mixed space where the concentration is spatially uniform within the volume of distribution. There are also other distribution models. Other than one-compartment model, there is plug-flow model available for plasma, and distributed model available for interstitium. The combination of the model of the two regions forms a complete two-region exchange PK model, yielding 2CXM, which model both plasma and interstitium as one compartment; tissue-homogeneity model (TH) and adiabatic approximation model (AATH), both of which assume plasma as plug-flow model and interstitium as one compartment; and distributed parameter model (DP), which models plasma as plug-flow and interstitium as distributed. Among those PK models, 2CXM is the most commonly implemented model for the analysis of DCE MRI.

The mass balance in 2CXM for each compartment can be easily developed. For plasma, it is:

$$v_p \frac{dC_p(t)}{dt} = F_p C_a(t) - F_p C_p(t) + PSC_e(t) - PSC_p(t) \quad (2.13)$$

For interstitium, it is

$$v_e \frac{dC_e(t)}{dt} = PSC_p(t) - PSC_e(t) \quad (2.14)$$

where $C_e(t)$ is CA concentration in the EES. Then $C_t(t)$ can be defined as the CA concentration of the tissue, which is the sum of the two regions:

$$C_t(t) = v_p C_p(t) + v_e C_e(t) \quad (2.15)$$

With Equation 2.13-2.15, the time-domain solution for 2CXM can be summarized as:

$$C_t(t) = F_p \cdot C_p(t) * \left(Me^{-\alpha t} + (1-M)e^{-\beta t}\right), \quad (2.16)$$

where

$$\alpha = \frac{PS(v_p + v_e) + F_p \cdot v_e + \sqrt{PS^2(v_p + v_e)^2 + F_p^2 v_e^2 - 2PS \cdot F_p(v_p - v_e)v_e}}{2v_p \cdot v_e}, \quad (2.17)$$

$$\beta = \frac{PS(v_p + v_e) + F_p \cdot v_e - \sqrt{PS^2(v_p + v_e)^2 + F_p^2 v_e^2 - 2PS \cdot F_p(v_p - v_e)v_e}}{2v_p \cdot v_e}, \quad (2.18)$$

and

$$M = \frac{-PS(v_p + v_e) + F_p \cdot v_e + \sqrt{PS^2(v_p + v_e)^2 + F_p^2 v_e^2 - 2PS \cdot F_p(v_p - v_e)v_e}}{2\sqrt{PS^2(v_p + v_e)^2 + F_p^2 v_e^2 - 2PS \cdot F_p(v_p - v_e)v_e}}, \quad (2.19)$$

using F_p, v_p, v_e, and PS as a set of independent parameters. Also, with fitted F_p, α, β, M, parameters v_p, v_e, and PS can be recovered as:

$$v_p = \frac{F_p}{M\alpha + (1-M)\beta}, PS = F_p \frac{M(1-M)(\alpha-\beta)^2}{(M\alpha + (1-M)\beta)^2}, v_e = F_p \frac{M(1-M)(\alpha-\beta)^2}{(M\alpha + (1-M)\beta)\alpha\beta} \quad (2.20)$$

2.3.5 Simplified model

The 2CXM is a very comprehensive model in describing the vascular properties of tissues. However, to accurately assess the four parameters, especially F_p, requires accurate capture of the contrast dynamics with high temporal resolution, which is unrealistic in most of the applications. The simpler TK model is still the most widely used model in DCE MRI to date. Instead of estimating F_p and PS separately, TK model adopts the combined K^{trans}. TK model also has several alternatives under different circumstance.

Extended Tofts model

Extended Tofts model enables the measurement of v_p, K^{trans}, and v_e. It is a simplification of 2CXM under high-perfusion condition, where $F_p \to \infty$ and $K^{trans} = PS$. The solution to the model is:

$$C_t(t) = v_p C_p(t) + K^{trans} C_p(t) * e^{-\frac{K^{trans}}{v_e}(t)} \tag{2.21}$$

Although the assumption for infinite F_p is difficult to justify in most of tissue types, the experimental results showed that the parameters estimated by extended Tofts model is useful in variety of clinical applications.

Patlak model

Besides high perfusion, Patlak model assumes negligible back flux from the interstitium into the plasma. When the total acquisition time is short (~2 minutes after injection), this condition can be considered partially fulfilled. The solution to Patlak model is:

$$C_t(t) = v_p C_p(t) + K^{trans} \int_0^t C_p(\tau)\, d\tau \tag{2.22}$$

With reduced freedom of parameters and linear stucture, Patlak model is robust and readily applied. In some applications such as in the evaluation of carotid atherosclerosis with a DCE protocol of 2-5 minutes, patlak model is the most suitable model with best repeatability[67].

TK model

The classic TK model can be derived from 2CXM by assuming high-perfusion condition and weak-vascularization condition. In this context, $K^{trans} = PS$, $v_p \to 0$, $v = v_e$. The solution to TK model is:

$$C_t(t) = K^{trans} C_p(t) * e^{-\frac{K^{trans}}{v_e}(t)} \tag{2.23}$$

2.4 State-of-Art Practice of DCE MRI

2.4.1 Clinical practice

Breast cancer

DCE MRI plays a central role in current standard of care for breast cancer. Clinical practice suggests that DCE MRI has the highest sensitivity, which is close to 100%, among all the imaging modalities in the diagnosis of breast tumor[10]. The standard clinical protocol acquires 3D T1W GRE images covering entire breast with voxels smaller than $1\times1\times3$ mm^3, yielding a temporal resolution at 1 to 2 minutes. With the advance in the imaging technique, new DCE MRI methods with improved temporal resolution have been proposed. Abe et al. used ultrafast DCE technique, which achieves voxel size at $1.5\times1.5\times3.0$ mm^3 and temporal resolution at 7 seconds, can differentiate malignant and benign tumors using semi-quantitative parameters initial enhancement rate and SER[3]. For quantitative DCE, some studies have suggested that K^{trans} is positively correlated with

histopathological markers such as MVD[26] and vascular permeability[27]. Changes in the PK parameters such as F_p, K^{trans} and v_e can indicate the response to therapy of breast cancer at early course of the treatment[5,31,68].

Pancreatic ductal adenocarcinoma (PDAC)

DCE MRI is an essential component for clinical management of PDAC. Previous investigations have suggested that DCE MRI has superior accuracy in the detection of PDAC compared to clinical standard MDCT, especially with small tumors (<=1.5 cm)[16]. However, one major drawback for the clinical protocol is that it only comprises four DCE phases as specified in Section 1.2.1 due to the sampling conflict and the requirement for breath-hold, which makes it incapable of quantitative analysis. To allow for accelerated and continuous acquisition for quantification, reduced coverage or patient cooperation such as prone position or shallow breath are usually necessary[24,30]. New imaging techniques using radial sampling pattern, which is more robust to motion has also been implemented[29]. Quantitative analyses have shown that K^{trans} and v_e are positively correlated with vascular density and fibrosis in PDAC, respectively[24,25]. It has also been reported that the changes of PK parameters can indicate the effectiveness of therapy at early phase.

Carotid atherosclerosis

In carotid atherosclerosis, quantitative DCE MRI has been used to characterize the plaque neovascularization, a significant indication of inflammation which is the key factor facilitating plaque vulnerability. Studies have shown that v_p and K^{trans} are

significantly correlated with inflammatory markers including macrophages, neovasculature, and loose matrix, suggesting v_p and K^{trans} can be used as imaging markers for plaque inflammation[22,69]. Other works also presented that K^{trans} is a useful biomarker to assess the treatment effect on vasa vasorum[70].

2.4.2 Novel techniques

In recent years, various new techniques have been proposed to address the common limitations in DCE MRI specified in Section 1.3.

K-space weighted image reconstruction (KWIC)

The k-space weighted image reconstruction was first proposed by Song et al[71,72]. This technique achieves the reconstruction of images at high spatial and temporal resolution simultaneously using radial sampling pattern. Figure 2.6 displays the schematic principle for KWIC. The acquired radial views are divided into N subsets (N = 4 as an example). For current subset, the views are equally spaced between 0° and 180°. The selected angle for views of the next subset bisects the angles in current subset. During the reconstruction, the central k-space area employs data from a single subset; the adjacent k-space region at Nyquist radius adopt the data from the same subset and also the time-neighboring subset; the outermost k-space region was contributed by all radial view. This technique has been applied to acquire data for abdominal DCE MRI[29]. A temporal resolution at 4.1 second with voxel size $1.5\times1.5\times5$ mm^3 covering a volume of $380\times380\times200$ mm^3 were achieved. The PK parameters derived accordingly were feasible for PDAC characterization. An improved technique to achieve respiratory motion compensated KWIC were proposed by Lin et al. at 2008[73]. The DCE images were

reconstructed at end-expiration state at a temporal resolution equal to respiratory rate and a spatial resolution at 2×2×5 mm^3 covering a coronal volume of 380×380×80 mm^3.

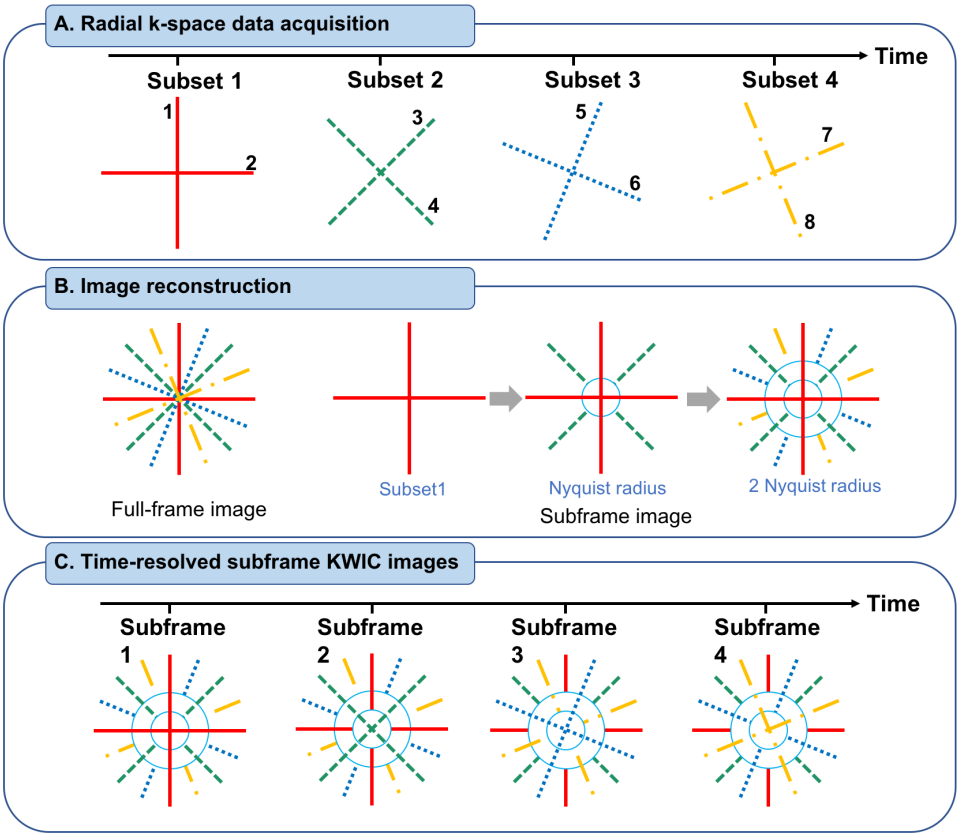


Figure 2.6: Principles of KWIC reconstruction technique. (A). Diagram of the four-interleaf angle-bisection reordering acquisition scheme is presented using a simple example composed of eight projection views. During MR scanning of one full-frame image series, k-space data are acquired radially so that subsequent projection views bisect the earlier ones. Projection views are grouped into four interleaved subsets that are serially acquired. (B). For the reconstruction of full-frame images by gridding, data from all subsets are combined without weighting. For the reconstruction of subframe images by KWIC view-sharing, the central k-space is filled with data of the timely subset and the adjacent k-space at the Nyquist-radius is filled with data from the time-contiguous subset. The outermost K-space is filled with data from all subsets. (C) The four time-resolved subframe KWIC images have different k-space cores and similar k-space peripheries. This KWIC view-sharing is possible because of the oversampled, central k-space data of radial MRI. Data of a single subframe image set can improve the effective temporal resolution by a factor of 4. Redrawn after Kim (2013)

XD-GRASP

Feng et al. proposed Golden-angle RAdial Sparse Parallel (GRASP) technique, which combines compressed-sensing, parallel imaging, and golden-angle radial sampling pattern for fast and flexible free-breathing dynamic volumetric MRI[74]. Coil sensitivity maps

are calculated using the temporal average of all acquired radial spokes from raw k-space data. Then, raw k-space data are resorted into different temporal frames, each of which contains a Fibonacci number (e.g., 34, 21,13,…) of consecutively acquired spokes. The choice of the number is according to the desired temporal resolution. Due to the strong image correlation along the multiple temporal frames, a temporal sparsity constraint is employed to exploit. The GRASP reconstruction is formulated as:

$$\hat{d} = \underset{d}{\operatorname{argmin}} \|F \cdot S \cdot d - m\|_2^2 + \lambda \|\mathrm{T} \cdot d\|_1 \,, \tag{2.24}$$

where d is the desired image series, m is the acquired multi-coil k-space data, S is the sensitivity maps, F is NUFFT operator, T is a temporal total variation operator, and λ is the regularization factor.

Based on this work, Feng et al. proposed XD-GRASP, where XD represents eXtra dimension to resolve physiological motion for free-breathing acquisition[75]. Take 3D dynamic abdominal case as an example: one extra step for XD-GRASP is to characterize respiratory motion into several states using a combination of the 1D imaging lines at k_x=k_y=0. The reconstruction problem can be formulated as:

$$\hat{d} = \underset{d}{\operatorname{argmin}} \|F \cdot S \cdot d - m\|_2^2 + \lambda_1 \|\mathrm{T}_1 \cdot d\|_1 + \lambda_2 \|\mathrm{T}_2 \cdot d\|_1 \,, \tag{2.25}$$

where T_1 is the sparsity constraint applied in the contrast enhanced dimension and T_2 is the sparsity constraint applied in the extra respiratory motion dimension. With the capability to resolve respiratory motion, the dynamic images showed less motion artifacts and improved depiction of the anatomical structure. This technique was performed on 4 volunteers and 1 patient with suspected liver lesions. The images were reconstructed at a temporal resolution ~13s with voxel size 1.4×1.4×3 mm^3 covering a volume of 360×360×240 mm^3.

2.4.3 Major technical challenges and concerns

Although various novel techniques have been proposed in recent years with promising preliminary results, quantitative DCE MRI still faces unsolved challenges. First of all, there is room to improve the coverage, and spatial/ temporal resolution. Previous studies have shown that a temporal resolution on order of 1 second would be preferred for the sampling of AIF[76-78] and a temporal resolution under 10 seconds for characterizing the dynamic in pathological tissues[35], which are still hard to achieve with current techniques. Second, no existing technique allows for dynamic T1 quantification, which is the most reliable way to calculate CA concentration. Moreover, the potential to reduce the CA dose while keeping the diagnosis power for DCE MRI techniques has not been widely evaluated. To address the unresolved limitations, we proposed a novel DCE technique based on our newly developed Multitasking framework.

2.5 MR Multitasking Framework

2.5.1 Image model

MR Multitasking framework was published by Christodoulou et al. in 2019[79]. This is a continuous-acquisition framework with the ability to resolve the temporal dynamics in multiple dimensions[80,81]. It is difficult to capture all the temporal dynamics with conventional MRI because the scan time grows exponentially with the number of dynamics, a phenomenon known as “curse of dimensionality”. Multitasking framework conceptualizes the different sources of temporal dynamics as different time dimensions and then resolves the multiple time dimensions using a low-rank tensor (LRT) imaging

method, which can exploit the high correlation along and across time dimensions and thus achieve a vastly accelerated scan[82-85].

Images in Multitasking framework are represented as a multidimensional function $I(\mathbf{x}, t_1, t_2, \cdots, t_N)$ of spatial location $\mathbf{x} = [x\ y\ z]^T$ and N time dimensions $t_1, t_2, \ldots, t_N$. Each time dimension corresponds to a specific 'task' to be resolved. Particular in the scope of quantitative DCE MRI, the example time dimensions consist of inversion-recovery (IR) or saturation-recovery (SR) time (for T1 quantification), physiological (respiratory/ cardiac) motion, and DCE time course depicting the CA passage. The image function can be formulated as a ($N+1$)-way tensor $\mathcal{A}$ consisting of elements $A_{jkm\cdots q} = I(\mathbf{x}_j, t_{1,k}, t_{2,m}, \cdots, t_{N,q})$ with voxel location $\{\mathbf{x}_j\}_{j=1}^{J}$ and each time dimension from $\{\ t_{1,k}\}_{k=1}^{K}$ to $\{\ t_{N,q}\}_{q=1}^{Q}$. Direct recovery of $\mathcal{A}$, whose dimension is $J \times K \times M \times \cdots \times Q$, requires the exponentially increased number of samples and consequently leads to impractical scan time. Fortunately, the high image correlation along each time dimension and across the spatial and time dimensions induces $\mathcal{A}$ to be low-rank, which can be decomposed into the product of core tensor $\mathcal{G}$ and $N+1$ factor matrices:

$$\mathcal{A} = \mathcal{G} \times_1 \mathbf{U}_{\mathbf{x}} \times_2 \mathbf{U}_{t_1} \times_3 \mathbf{U}_{t_2} \times_4 \cdots \times_{(N+1)} \mathbf{U}_{t_N}, \tag{2.26}$$

where the operator $\times_i$ denotes the ith mode product, the factor matrix $\mathbf{U}_{\mathbf{x}} \in \mathbb{C}^{J \times L}$ contains L spatial basis functions, each of which comprises J voxels, each factor matrix $\mathbf{U}_{t_i}$ contains L_i basis function for ith time dimension, and the core tensor $\mathcal{G} \in \mathbb{C}^{L \times L_1 \times \cdots \times L_N}$ is the coefficient dominating the interaction between factor matrices. The low-rankness of $\mathcal{A}$ assures that the number of basis functions is smaller than its original elements (e.g., $L \ll J$) for each factor matrix, reducing the total elements of the core tensor and factor matrices from $JK \cdots Q$ to $LJ + L_1K + \cdots + L_NQ + LL_1 \cdots L_N$. For imaging scenarios, the

bound is dominated by the first term LJ. Take the abdominal DCE as an instance. Given the spatial matrix size 300×300×60, 100 TIs for T1 mapping, 6 respiratory bins, and 300 different DCE phases with a temporal resolution at 1 second for a 5-min scan, the total elements in $\mathcal{A}$ is 300×300×60×100×6×300 ≈9.7×10^{11}, while the decomposed factor matrices with ranks [20, 5, 6, 150] has approximately 1.6×10^{8}, yielding a 5000-fold reduction in the degrees of freedom.

For the convenience of notation, Equation 2.26 can be expressed in matrix form as

$$\mathbf{A}_{(1)} = \mathbf{U}_{\mathbf{x}}\mathbf{G}_{(1)}(\mathbf{U}_{t_N}\otimes\mathbf{U}_{t_{N-1}}\otimes\cdots\otimes\mathbf{U}_{t_1})^T, \tag{2.27}$$

where ⊗ denotes the Kronecker product, and the subscript (i) denotes the mode-i flattening of the tensor.

2.5.2 Sampling and reconstruction strategies

The acquired multi-channel signal $\mathbf{d}$ from tensor $\mathcal{A}$ can be expressed as $\mathbf{d} = \Omega\left(\mathbf{FSA}_{(1)}\right)$, where $\mathbf{S}$ is the multi-channel coil sensitivity maps, $\mathbf{F}$ is the Fourier transform, and Ω is the undersampling pattern. The image tensor $\mathcal{A}$ can be recovered by solving the following optimization problem:

$$\hat{\mathcal{A}} = \arg\min_{\mathcal{A}}\left\|\mathbf{d} - \Omega\left(\mathbf{FSA}_{(1)}\right)\right\|_2^2 + \lambda\sum_{n=1}^{N+1}\left\|\mathbf{A}_{(n)}\right\|_* + R(\mathcal{A}), \tag{2.28}$$

where λ is a regularization factor, $\|\cdot\|_*$ denotes the nuclear norm (accounting for low-rank-ness), and $R(\cdot)$ is an optional additional regularization functional, which can be chosen to enforce complementary image properties such as transform sparsity.

Although the implement of LRT model frees a large sampling requirement for recovering $\mathcal{A}$, directly solving the problem specified by Equation 28 are still impractical under some circumstances, particularly with 3D dynamic imaging, due to the large size of $\mathcal{A}$. To avoid the consuming of computational resources, the reconstruction of $\mathcal{A}$ can be factorized into the explicitly recovery of the spatial factor matrix:

$$\widehat{\mathbf{U_x}} = \arg\min_{\mathbf{U}} \|\mathbf{d} - \Omega(\mathbf{FSU_x\Phi})\|_2^2 + R(\mathbf{U_x}), \tag{2.29}$$

where $\mathbf{\Phi} = \mathbf{G}_{(1)}(\mathbf{U}_{t_N} \otimes \mathbf{U}_{t_{N-1}} \otimes \cdots \otimes \mathbf{U}_{t_1})^T$ is the temporal basis function comprising core tensor and all temporal factor matrices. With known $\mathbf{\Phi}$, the optimization problem can be reduced to recover L columns of $\mathbf{U_x}$, which is way more feasible.

Containing only temporal information, $\mathbf{\Phi}$ can be constructed by using s subset of k-space data designated to a limited location (usually the central k-space area due to it contains most of the image contrast) sampled much more frequently than the rest of the k-space. This subset of k-space data, which is referred to as training data, contains limited spatial information but a wealth of temporal information to determine $\mathbf{\Phi}$. In most current applications of MR Multitasking, the training data is usually the collection of center k-space readout acquired periodically with a frequency enough to resolve the finest temporal dynamics (typically is cardiac motion). Steps to determine $\mathbf{\Phi}$ from training data is specified in Section 2.5.3.

The remaining subset of data, referred to as imaging data, is usually sampled incoherently of the entire k-space locations to determine the spatial factor matrix $\mathbf{U_x}$ using Equation 2.29.

2.5.3 Tensor subspace estimation

The training data can be expressed as a $(\mathbf{k}, t_1, t_2, \cdots, t_N)$-space tensor $\mathcal{D}_{\mathrm{tr}}$. In practice, due to the limited scan time, the measured training data $\mathbf{d}_{\mathrm{tr}}$ covers some combinations of contrast-weightings and motion states experienced during the scan, but typically not all combinations. Therefore, the acquired training data tensor is incomplete and can be recovered by:

$$\widehat{\mathcal{D}_{\mathrm{tr}}} = \arg\min_{\mathcal{A}} \|\mathbf{d}_{\mathrm{tr}} - \Omega_{\mathrm{tr}}\mathcal{D}_{\mathrm{tr}}\|_2^2 + \lambda \sum_{n=1}^{N+1} \left\|\mathcal{D}_{\mathrm{tr},(n)}\right\|_* + R_{tr}(\mathcal{D}_{\mathrm{tr}}), \tag{2.30}$$

where Ω_{tr} is the sampling pattern for training data, and $R_{tr}(\cdot)$ is a temporal regularization functional. Equation 2.30 required no Fourier transform, and the training data is acquired on a small subset of k-space locations, so the tensor completion problem defined by Equation 30 is far less computationally expensive compared to Equation 28. Once the training data tensor is complete, each factor matrix of $\mathbf{\Phi}$ can be quickly obtained from $\widehat{\mathcal{D}_{\mathrm{tr}}}$ by high order SVD.

The factor matrices from some time dimensions in some applications can be generated ahead of time, even before any data are acquired. For example, T1 relaxation is physically governed by Bloch equation, the factor matrix corresponding T1 relaxation can be created from a dictionary of T1 recovery signal curves. The dictionary is developed with a range of physically feasible T1 values and B1 inhomogeneities. The corresponding factor matrix can be directly extracted from the SVD of this dictionary. In this scenario, the tensor completion problem can be expressed as:

$$\widehat{\mathcal{D}_{\mathrm{tr}}} = \arg\min_{\mathcal{D}_{\mathrm{tr}} \in \Psi} \|\mathbf{d}_{\mathrm{tr}} - \Omega_{\mathrm{tr}}\mathcal{D}_{\mathrm{tr}}\|_2^2 + \lambda \sum_{n=2}^{N+1} \left\|\mathbf{D}_{\mathrm{tr},(n)}\right\|_* + R(\mathcal{D}_{\mathrm{tr}}), \tag{2.31}$$

Where Ψ is a tensor subspace defined from the columns of the factor matrix generated to describe T1 relaxation.

With the determined temporal basis function $\mathbf{\Phi}$, and recovered spatial basis function using Equation 2.29, the final reconstructed image tensor $\mathcal{A}$ is defined by $\mathbf{A}_{(1)} = \mathbf{U}_{\mathbf{x}}\mathbf{\Phi}$.

CHAPTER 3: MULTITASKING DCE MRI IN THE CHARACTERIZATION OF CAROTID ATHEROSCLEROSIS

3.1 Introduction

Carotid atherosclerosis is a primary pathological process underlying ischemic stroke, a leading cause of morbidity and mortality worldwide[86]. A major driving force behind the progression of plaque destabilization and rupture is inflammation, which weaken plaque structural integrity including inhibition of collagen production and dissolution of the fibrous matrix by means of matrix metalloproteinases[22,87-89]. One of the hallmarks of vascular inflammation is vasa vasorum neovascularization, which provides the pathways for harnessing inflammatory cell types such as monocytes and macrophages to the vessel wall. In addition, elevated adventitial vasa vasorum permeability is associated with the increase of intimal thickness, endothelial dysfunction and inflammation of plaques[90-93].

DCE MRI has been used for quantitative assessment of the neovascular architecture and perfusion properties in carotid artery wall[22,23,65,69,70,94-97]. The correlation between v_p and K^{trans} from DCE and the proinflammatory cardiovascular risk factors has been demonstrated[22]. In an atherosclerotic rabbit model, K^{trans} and AUC have been found to correlate with aortic plaque neovascularization[23]. Other works also presented that K^{trans} is a useful biomarker to assess the treatment effect on vasa vasorum[70].

Despite these encouraging results, the current application of DCE MRI in carotid vessel wall imaging still faces demanding technical challenges, including: 1) submillimeter in-plane spatial resolution (0.5–0.7mm), required for accurate contrast kinetic

characterization without significant partial volume effects of vessel wall; 2) adequate anatomical coverage, required to cover the entire carotid vasculature; 3) high temporal resolution, required to accurately capture the contrast kinetics in AIF; 4) accurate quantification of the CA concentration in the tissue of interest. These requirements are conventionally in direct conflict with each other, forcing compromises to be made. For example, Kerwin *et al.* used high in-plane spatial resolution with 2D acquisitions while sacrificing anatomical coverage and temporal resolution. Calcagno *et al.* adopted a 3D sequence with 0.6 mm isotropic resolution by lowering the temporal resolution to around 30 s[23]. In addition, existing DCE protocols in carotid atherosclerosis directly transform the change in pixel signal intensity to CA concentration for PK modeling[23,95], which can introduce potential errors in the estimation of PK parameters[69].

To satisfy all the technical requirements of carotid vessel wall imaging, we propose a T1 mapping-based DCE method using MR Multitasking[79], which employs a low-rank tensor (LRT) imaging model[80,81,98-100] to exploit the high correlation between images at different saturation recovery times and different contrast enhancement phases and thus achieves a vastly accelerated acquisition. The Multitasking DCE was applied with 3D Cartesian sampling, allowing for faster reconstruction. Bulk motion detection and removal scheme were also implemented for the improvement of image quality. This novel technique enables 3D acquisition with high spatial resolution (0.7 mm isotropic), high temporal resolution (595 ms), and large coverage of the carotid arteries. Moreover, contrast concentration estimation is based on fully quantitative dynamic T1 mapping during the enhancement process for accurate PK modeling. Based on this technique, fully quantitative evaluation of the PK parameters can be achieved.

3.2 Methods

3.2.1 Sequence design

A non-selective saturation-recovery (SR) preparation pulse followed by 3D FLASH readout with flow compensation was used as the basic sequence structure (Figure 3.1A). The FLASH readouts sample the entire recovery period in between SR prep pulses so that T1 can be quantified. Pre-contrast T1 values for the main tissues of interest (blood, vessel wall, and muscle) are relatively long (over 1000 ms). Classically, distinguishing T1 from proton density (PD) during parameter mapping would require a long recovery period, leading to low imaging speed and risking corruption of the signal evolution by the inflow of fresh blood. Fortunately for time-resolved DCE T1 mapping, a static PD map can be shared amongst the series of T1 maps at different contrast phases (including the peak contrast phase where T1 is shortest), allowing for much shorter recovery periods.

3.2.2 Sampling pattern

A 3D Cartesian sampling scheme was used for data acquisition, as shown in Figure 3.1B. Randomized Gaussian-density sampling in both the phase (k_y) and partition (k_z) encoding was used to incoherently undersample the k-space[101,102]. In addition, the k-space center line ($k_y = k_z = 0$) was collected every 8 readout lines as training data to estimate the temporal basis function[79,98]. The temporal resolution of the training data is 88 ms. The rest of the k-space data are the imaging data, which contains high spatial resolution information to recover the spatial factor $\mathbf{U}$.

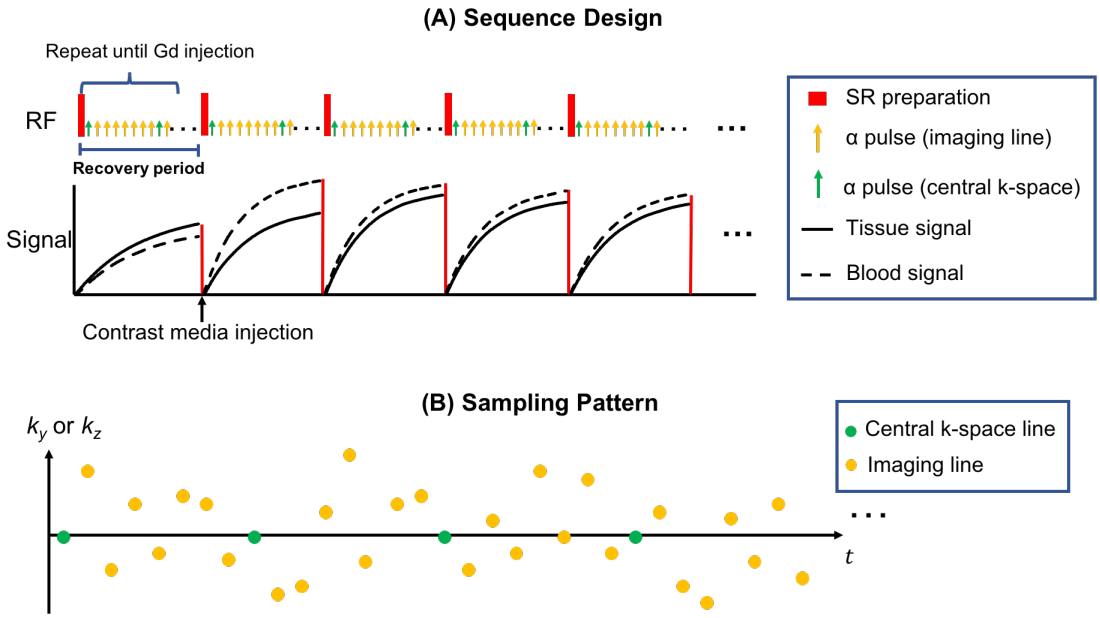


Fig 3.1 (A): Pulse sequence diagram for the proposed 5D DCE and corresponding simulated signal evolution for vessel wall and blood. Non-selective saturation recovery preparation pulse is applied every TR followed by a series alpha pulses. A readout lines is collected every alpha pulse. This SR period is repeated to traverse the entire k-space seven times during the scan. The contrast media is injected when 144 SR periods was collected. (B): Simplified illustration of k-space sampling strategy. Cartesian acquisition with randomized reordering in ky and kz directions is implemented according to a variable-density Gaussian distribution. A center k-space line is acquired every 8 lines as the LRT subspace training data. Rest of the data forms the imaging data.

3.2.3 Image reconstruction

The proposed Multitasking DCE technique acquired 5D images a with three spatial dimensions (x, y, z) and two time dimensions (saturation recovery time τ and DCE time course t), which can be formulated as a three-way tensor $\mathcal{A}$ with space location $\mathbf{x} = [x\ y\ z]^T$, τ, and t. High image correlation induces $\mathcal{A}$ to be low-rank and can be factorized as:

$$\mathbf{A}_{(1)} = \mathbf{U}\mathbf{G}_{(1)}(\mathbf{W} \otimes \mathbf{V})^T, \tag{3.1}$$

where the columns of $\mathbf{U}$, $\mathbf{V}$, and $\mathbf{W}$ contain the basis functions for spatial, SR, and DCE time dimensions. This low-rank model separates the image into spatial and temporal factors, decoupling the tradeoffs between spatial and temporal resolution and reducing

the degrees of freedom in the image, thereby providing an avenue for accelerated acquisition.

Image reconstruction is divided into three steps: 1) pre-determine the T1 recovery basis functions in $\mathbf{V}$ from a dictionary of SR signal curves; 2) estimate the DCE basis functions in $\mathbf{W}$ and the core tensor $\mathcal{G}$ from the training data; and 3) recover the basis images in $\mathbf{U}$ by fitting the known tensor factors to the imaging data.

In the first step, because T1 relaxation is physically governed by the Bloch equations, a dictionary of feasible SR signal curves is generated ahead of time for a range of T1 values and B1 inhomogeneities. Specifically, the dictionary had 101 T1 values logarithmically spaced from 100 ms to 3000 ms, 17 flip angles from 4° to 12° with half-degree increments, and 21 saturation pulse angles linearly spaced from 60° to 120°. The T1 recovery factor $\mathbf{V}$ was directly extracted from the singular value decomposition (SVD) of this dictionary.

With $\mathbf{V}$ obtained, the core tensor $\mathcal{G}$ and DCE factor $\mathbf{W}$ can be obtained from the training data as follows. Denoting the $(\mathbf{k}, \tau, t)$-space tensor of training data as $\mathcal{D}_{\mathrm{tr}}$, we solve the small-scale low-rank tensor completion problem:

$$\widehat{\mathcal{D}}_{\mathrm{tr}} = \arg \min_{\mathbf{D}_{\mathrm{tr},(2)} \in \mathrm{range}(\mathbf{V})} \|\mathbf{d}_{\mathrm{tr}} - \Omega_{\mathrm{tr}}\mathcal{D}_{\mathrm{tr}}\|_2^2 + \lambda \left(\left\|\mathbf{D}_{\mathrm{tr},(1)}\right\|_* + \left\|\mathbf{D}_{\mathrm{tr},(3)}\right\|_* \right) + R_{tr}(\mathcal{D}_{\mathrm{tr}}) \quad (3.2)$$

The regularization functional $R_{tr}(\cdot)$ was chosen as temporal total variation (TV) in the DCE time direction [75,103,104]. With complete $\widehat{\mathcal{D}}_{\mathrm{tr}}$, now the temporal factor, $\mathbf{\Phi} = \mathbf{G}_{(1)}(\mathbf{W} \otimes \mathbf{V})^T$ can be quickly extracted by truncating the SVD of $\widehat{\mathbf{D}}_{\mathrm{tr},(1)}$ or the higher-order SVD (HOSVD) [105] of $\widehat{\mathcal{D}}_{\mathrm{tr}}$. The λ was chosen based on the discrepancy principle [106] for one dataset, and then used for all datasets.

With a known temporal subspace spanned by the rows of $\mathbf{\Phi}$, image reconstruction then reduces to the recovery of the L images in $\mathbf{U}$ from the acquired imaging data $\mathbf{d}$.

$$\hat{\mathbf{U}} = \arg\min_{\mathbf{U}} \|\mathbf{d} - \Omega(\mathbf{FSU\Phi})\|_2^2 + R(\mathbf{U}) \tag{3.3}$$

The spatial TV regularizer was chosen as the spatial regularization functional to integrate compressed sensing into the low-rank framework [85,103].

3.2.4 Dynamic T1 quantification and PK model

With the reconstructed 5D images, pixelwise dynamic T1 mapping was performed to quantify CA concentration. The signal intensity of at a certain DCE time t can be expressed as:

$$s\big(A,\alpha,B,n,R_1(t)\big) = A\frac{1-e^{-T_\mathrm{R}\cdot R_1(t)}}{1-e^{-T_\mathrm{R}\cdot R_1(t)}\cos\alpha}\Big[1+(B-1)\big(e^{-T_\mathrm{R}\cdot R_1(t)}\cos\alpha\big)^n\Big]\sin\alpha, \tag{3.4}$$

with the relaxation rate $R_1(t) = 1/T_1(t)$ at DCE time t, amplitude A, SR pulse efficiency B, FLASH readout interval T_R, flip angle α, and SR time point n rendering $\tau = nT_\mathrm{R}$. The signal intensity vector $\mathbf{s}$ for an entire SR period with $n = 1, 2, \cdots, N$ at DCE time t is:

$$\mathbf{s}\big(A,\alpha,B,R_1(t)\big) = \big[s\big(A,\alpha,B,1,R_1(t)\big),\cdots,s\big(A,\alpha,B,N,R_1(t)\big)\big]^{\boldsymbol{T}}, \tag{3.5}$$

and the signal intensity matrix $\mathbf{S}$ over all DCE time bins $t = 0, 1, \cdots, T$ ($t = 0$ represents pre-contrast DCE phase) is:

$$\mathbf{S}(A,\alpha,B,\mathbf{r_1}) = \big[\boldsymbol{s}\big(A,\alpha,B,R_1(0)\big),\cdots,\boldsymbol{s}\big(A,\alpha,B,R_1(T)\big)\big], \tag{3.6}$$

where $\mathbf{r_1} = [R_1(0), R_1(1), \cdots, R_1(T)]^{\boldsymbol{T}}$ is the vector dynamic R_1 values over all DCE time bins. The CA concentration C_t can be quantified based on the relaxivity accordingly:

$$C_\mathrm{t}(t) = \frac{R_1(t) - R_1(0)}{\gamma} \tag{3.7}$$

Following the derivation of CA concentration, the extended Tofts model (Equation 2.21) was used for the estimation of PK parameters, accounting for potential reflux in the 9.8 min scan [97]. CA concentration curves for blood $C_{\mathrm{b}}(t)$ and tissues $C_{\mathrm{t}}(t)$ are extracted from left and right carotid arterial lumens and vessel wall, respectively.

Considering the hematocrit of blood, the $C_{\mathrm{p}}(t)$ can be determined with $C_{\mathrm{p}}(t) = C_{\mathrm{b}}(t)/(1 - \mathrm{Hct})$, assuming the average hematocrit value (Hct) of 0.4 [96,107]. With Equation 2.21 and the concentration curves over DCE time course t, v_p, K^{trans} and v_e can be fitted using the function *lsqnonlin* (non-linear least-square solver) in MATLAB (R2015b, Mathworks, MA, USA).

3.2.5 Abrupt motion removal

Abrupt movement of the subject, such as swallowing, is often inevitable during any scan that spans several minutes[108]. Unaddressed abrupt bulk motion leads to blurring and other motion artifacts. Because the carotid vessel wall is thin, it is especially sensitive to motion artifacts that worsen the partial volume effect, leading to incomplete vessel wall visualization and errors in quantification.

In the LRT framework, images with abrupt motion are less correlated with the remainder of the images and so would have a high residual after temporal estimation. Prior to image reconstruction, the outlier time points corrupted by bulk motion can therefore be detected by determining which columns of $\mathbf{D}_{\mathrm{tr}}$ (the Casorati matrix of raw training data) have a high residual after temporal subspace modeling. Calculating a "single-time" temporal factor matrix $\mathbf{\Phi}_{\mathrm{st}}$ (i.e., with only one time dimension indexing the readout number) from the SVD of $\mathbf{D}_{\mathrm{tr}}$, the training data residual is then:

$$\mathbf{E} = \mathbf{D}_{\mathrm{tr}} - \mathbf{D}_{\mathrm{tr}}\boldsymbol{\Phi}_{\mathrm{st}}^{\dagger}\boldsymbol{\Phi}_{\mathrm{st}}, \tag{3.8}$$

Where $\mathbf{E} \in \mathbb{C}^{N_{\mathrm{k}}N_{\mathrm{c}} \times N_{\mathrm{ro}}}$ is the residual matrix, $\mathbf{D}_{\mathrm{tr}} \in \mathbb{C}^{N_{\mathrm{k}}N_{\mathrm{c}} \times N_{\mathrm{ro}}}$ is the matrix of training data, $\boldsymbol{\Phi}_{\mathrm{st}} \in \mathbb{C}^{L \times N_{\mathrm{ro}}}$ is the single-time temporal factor matrix, N_{k} denotes the number of data points in each readout, N_{c} is the number of coils, N_{ro} represents the total number of training data readouts, and the superscript † denotes the pseudoinverse. The time-resolved sum-of-squares residual vector $\mathbf{r}$ can be calculated as having elements

$$e_j = \sum_i \left| E_{ij} \right|^2 \tag{3.9}$$

Training data corresponding to high-residual time points were removed before evaluating Equation 3.2, and imaging data immediately surrounding those time points were removed before evaluating Equation 3.3.

The effect of motion removal was tested by comparing the signal-to-noise ratio (SNR) of blood and vessel wall, the contrast-to-noise ratio (CNR) of vessel wall versus blood and the sharpness of blood/vessel wall boundary of the image with motion removal with the same frame without motion removal. The SNR of the tissue of interest was defined by:

$$SNR_t = \frac{SI_t}{\sigma_{bg}}, \tag{3.10}$$

with SI_t is the signal intensity of the tissue of interest, and σ_{bg} is the standard deviation of the background signal. The CNR was defined by:

$$CN_{t1,2} = \frac{SI_{t1} - SI_{t2}}{\sigma_{bg}}, \tag{3.11}$$

with SI_{t1} and with SI_{t2} are the signal intensity of the two tissues. The sharpness of the blood/vessel wall boundary was estimated using the rise-distance method [109].

3.2.6 Simulations

The simulations were carried out in MATLAB to demonstrate: 1) Multitasking DCE is capable of dynamic T1 quantification; 2) using dynamic T1 quantification to estimate PK parameters yields higher accuracy and precision compared to conventional linear or nonlinear approaches; 3) temporal resolution can affect the estimation of PK parameters. For the first aim, a 3D numerical phantom with the same matrix size as the in vivo data consisting of blood, vessel wall, and plaque was created. The AIF was generated using a traditional biexponential equation as used in [96]:

$$C_{\mathrm{p}}(t) = \begin{cases} 0, & t < t_0 \\ kt, & t_0 \le t < t_1 \\ D\left[a_1 \exp\left(-\dfrac{t-t_1}{\tau_1}\right) + a_2 \exp\left(-\dfrac{t-t_1}{\tau_2}\right)\right], & t \ge t_1 \end{cases} \tag{3.12}$$

Where t_0 is the time when contrast agent is injected, and t_1 is the peak enhanced point for AIF. The initial T1 for blood $T_{1,\mathrm{b}}(0)$ was chosen as 1550 ms. The CA concentration curves in vessel wall and plaque were then generated according to the extended Tofts model. For vessel wall, $T_{1,\mathrm{vw}}(0) = 1200\,ms$, v_p = 0.1, K^{trans} =0.12 min^{-1}, v_e = 0.5. For plaque, $T_{1,\mathrm{pl}}(0) = 900\,ms$, v_p = 0.15, K^{trans} =0.18 min^{-1}, v_e = 0.8. The dynamic T1s for blood, vessel wall and plaque were generated based on the following equation 3.7. Subsequently, the real-time signal curves for each tissue was created based on Equation 3.6.

The generated phantom images were Fourier transformed to k-space and complex white Gaussian noise was added to achieve an SNR of 20. The noisy k-space data were

undersampled and reconstructed as described in Section 3.2.2 and 3.2.3. Dynamic T1 mapping and PK modeling were then performed. The error between the estimated dynamic T1 and PK parameters and true values were evaluated for vessel wall and plaque.

In the second step, the same 3D phantom were used with different sets of PK parameters representing normal and pathological tissues. The original CA concentration curves for different tissues were generated at a temporal resolution at 0.1 second. Then the signal curves for Multitasking DCE and steady-state SPGR images were created based on Equation 3.7 and Equation 2.3, respectively. The same SNR were added to both image sets. Then, the PK parameters were derived using T1 quantification approach (denoted as Multitasking approach) for Multitasking DCE images, and linear (denoted as LA) or nonlinear approaches (denoted as NLA) for steady-state SPGR images. Each experiment was conducted 100 times. The mean value and standard deviation of the PK parameters estimated using each approach were then assessed.

3.2.7 Imaging experiments

The proposed protocol was implemented on a 3T clinical MR scanner (MAGNETOM Verio, Siemens Healthineers, Erlangen, Germany). Each SR period lasted 595 ms with 52 TIs, one every 11 ms. One readout line was collected per TI. The SR period was repeated 1008 times in a scan of 9.8 min, resulting in a total of 52×1,008 = 52,416 time points, each corresponding to a 3D image. The DCE bin temporal footprint was selected to be 1.2 s as two SR periods, except when evaluating the effect of different temporal resolutions/footprints. Detailed imaging parameters are summarized in Table 1.

Table 3.1. Multitasking DCE sequence parameters

Imaging Parameters (in coronal orientation)			
Field of view (FOV)	150 mm × 150 mm	**Slab thickness**	26 mm
Matrix size	208 × 208 × 36	**Spatial resolution**	0.7 mm isotropic
Recovery period	595 ms	**Number of TI per recovery period**	52
$\mathbf{T_R}$	11 ms	$\mathbf{T_E}$	6.8 ms
Flip angle	8°	**Scan Time**	9.8 min

3.2.8 Phantom study

To validate the T1 mapping accuracy and inter-session repeatability of the proposed Multitasking DCE, two experiments were performed on the same T1 phantom on separate days. The T1 values of the phantom ranged from 70 ms to 2000 ms, covering the pre- and post-contrast T1 values of the major tissue types of interest. Images with standard 2D inversion-recovery spin-echo (IR-SE) sequence with TR = 10000 ms and seven different inversion times (23, 100, 400, 900, 1600, 2200, 3000 ms) were also acquired at the center slice to provide the T1 reference. Other IR-SE imaging parameters were: FOV = 150×150 mm^2, in-plane spatial resolution = 1.2 mm, slice thickness = 8 mm.

3.2.9 In vivo study

The in vivo study was approved by the ethics boards of local institutions. All subjects gave written informed consent before participating in this study. Fourteen healthy volunteers (aged 25 to 57 years, five females) were recruited for the study; to assess the inter-session repeatability of the proposed method, seven of the volunteers were scanned twice, on different days, using the same protocol. Subjects were scanned using a 12-

channel head coil and a 4-channel surface coil from the system vendor. During the imaging session, localizers and time-of-flight (TOF) MR angiography were acquired to identify the overall neck anatomy. Following these sequences, Multitasking DCE was performed. Gd contrast media (Gadavist, 0.1 mmol/kg, Bayer Schering Pharma) was injected intravenously 1.4 minute into the scan, when 144 SR periods were collected. The injection rate was 1 mL/s, followed by a 20 mL saline flush at the same rate. To provide an in vivo T1 reference, pre- and post-contrast single-slice MOLLI [110] at 1.17 mm in-plane spatial resolution were also acquired immediately before and after the DCE scan, respectively. Vessel wall was not visible on the MOLLI images due to low spatial resolution, but the T1 values of blood and muscle could be quantified and were adopted as the reference.

Furthermore, seven patients (aged 54 to 80 years, three females) with a history of carotid atherosclerosis were recruited. In addition to the abovementioned protocol, a series of conventional carotid plaque imaging protocols including pre-contrast T1W turbo-spin-echo (TSE), pre-contrast T2W TSE and post-contrast T1W TSE were collected to assist in plaque diagnosis.

3.2.10 Image analysis

For each subject in the control group, three slices (two below the carotid bifurcation and one above) with clear vessel wall delineation were selected for analysis. ROI of the vessel wall in normal subjects was manually selected using the T1W images at early TIs and the pre-contrast T1 maps. For the paired measurements of the same subject on separate days, slices were matched manually and corresponding slices were selected for

comparison. In the patient group, the anatomical location of the plaque is identified on the conventional images. Then the anatomical location of the plaque was manually defined on the corresponding Multitasking DCE images. Three slices around plaque area were selected for each subject. Pixel-wise mapping for v_p, K^{trans} , v_e and AUC were obtained for each slice in MATLAB.

3.2.11 Inter-session repeatability at different temporal resolution

In practice, too high temporal resolution may result in noisy concentration curves, while too low temporal resolution may cause blurring of the fast-changing dynamic information, particularly in the AIF. To evaluate the impact of temporal resolution on the PK parameter mapping, the repeatability of PK parameters at different temporal resolutions were evaluated in the seven repeated subjects. Temporal resolutions from 595 ms to 7.2 s were retrospectively selected for image reconstruction.

3.2.12 Statistical analysis

Intra-group mean value and standard deviation of PK parameters for both the control and patient groups were calculated, and a two-way mixed ANOVA was performed in SPSS (Version 24, IBM, NY, USA) to address any correlation between samples arising from the use of three slices from each subject. For the mixed ANOVA, slice location was set as a within-subjects factor and the group (control or patient) was set as a between-subjects factor; a slice/group interaction term was included in the analysis. A *p* value of less than 0.05 was considered to be significant. Repeatability analysis, including Bland-Altman analysis, coefficient of variation (CV) [97] and intraclass correlation coefficient (ICC)

[111] of v_p, K^{trans}, v_e and AUC were applied to the data collected from the seven repeated volunteers.

3.3 Results

3.3.1 Simulations

The 3D numerical phantom simulating a carotid vessel in oblique direction with blood, vessel wall, and atherosclerosis were generated successfully. The true and fitted dynamic T1s are shown in Figure 3.2, with relative differences less than 1.0% for all tissues over all time points. Figure 3.3 shows the maps for dynamic T1 fitting at pre-contrast, peak-enhanced, and delayed phases and PK parametric mapping, respectively. The mean error of PK parametric mapping is within 3.0% for all tissues, as listed in Table 3.2.

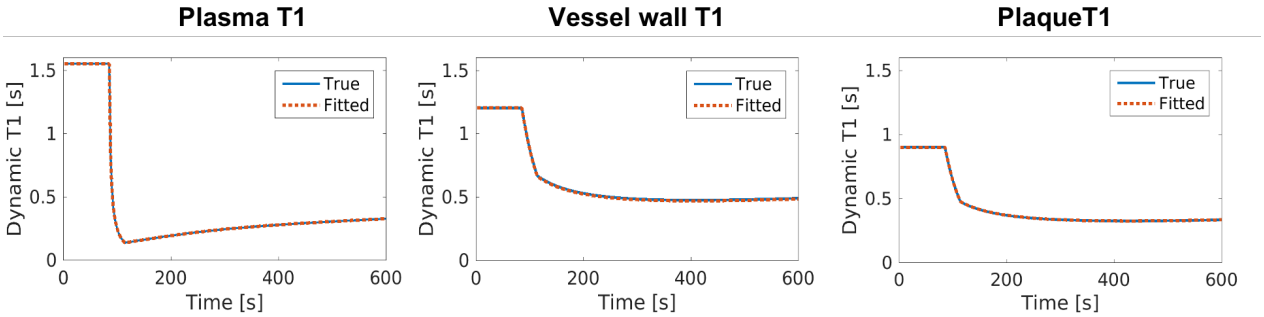


Fig 3.2: The result of fitted dynamic T1 compared with the true value. The fitted dynamic T1 curves are the mean value over the ROI.

Figure 3.4 displays the relative mean error and relative standard deviation of the PK parameters estimated using Multitasking approach, linear approach, and non-linear approach. When temporal resolution is high (<10 seconds), Multitasking approach showed best performance in the estimation of PK parameters, producing the smallest bias and standard deviation for both tissues and all parameters.

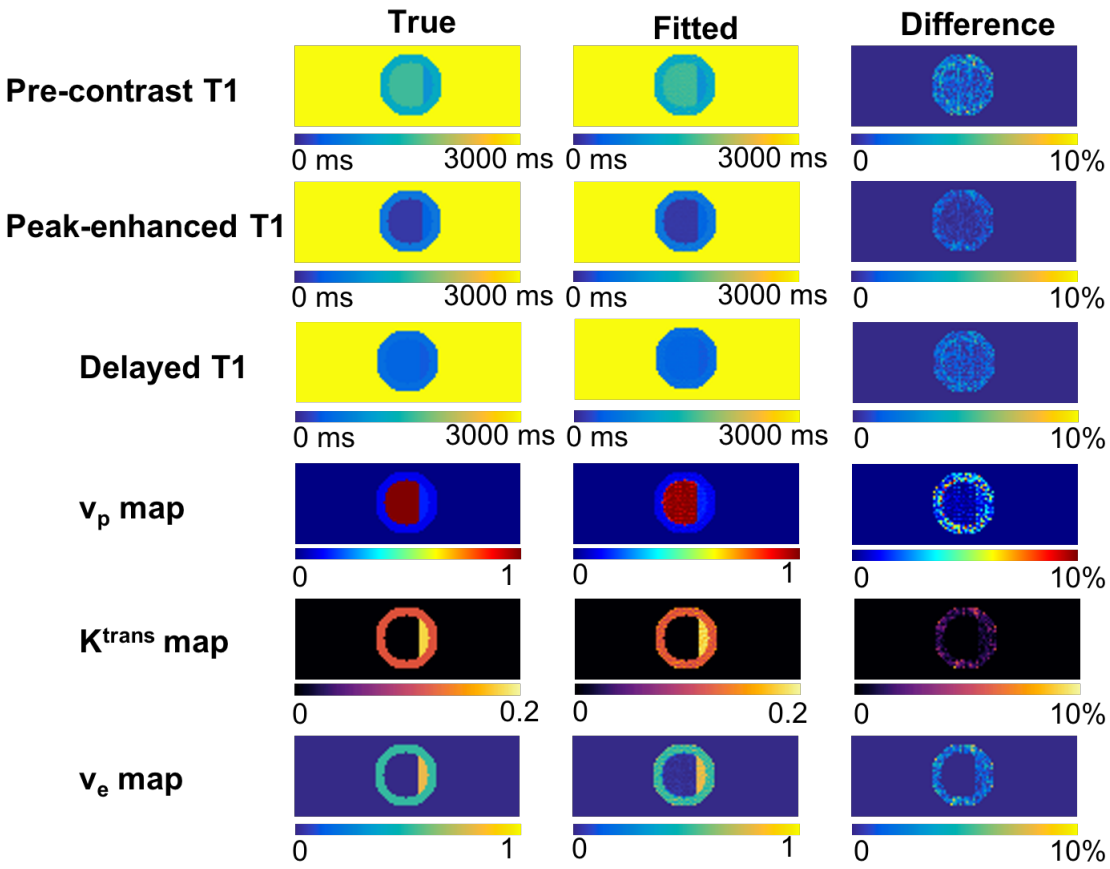


Fig 3.3: Pixel-wised parametric mapping. The first column shows the true map of the parameter. The second column shows the fitted map. The third column shows the absolute relative difference of the fitted map compared with the true map.

Table 3.2: The mean and standard deviation of the kinetic parameters compared with the true value. The standard deviation reports the variance of parameter value within the ROI.

		v_p	K^{trans} (min^{-1})	v_e
Vessel wall	True	0.100	0.120	0.500
	Fitted	0.103±0.014	0.123±0.010	0.514±0.018
	Mean error	3.0%	2.5%	2.8%
Plaque	True	0.150	0.180	0.800
	Fitted	0.154±0.010	0.181±0.006	0.792±0.022
	Mean error	2.7%	0.6%	-1.0%

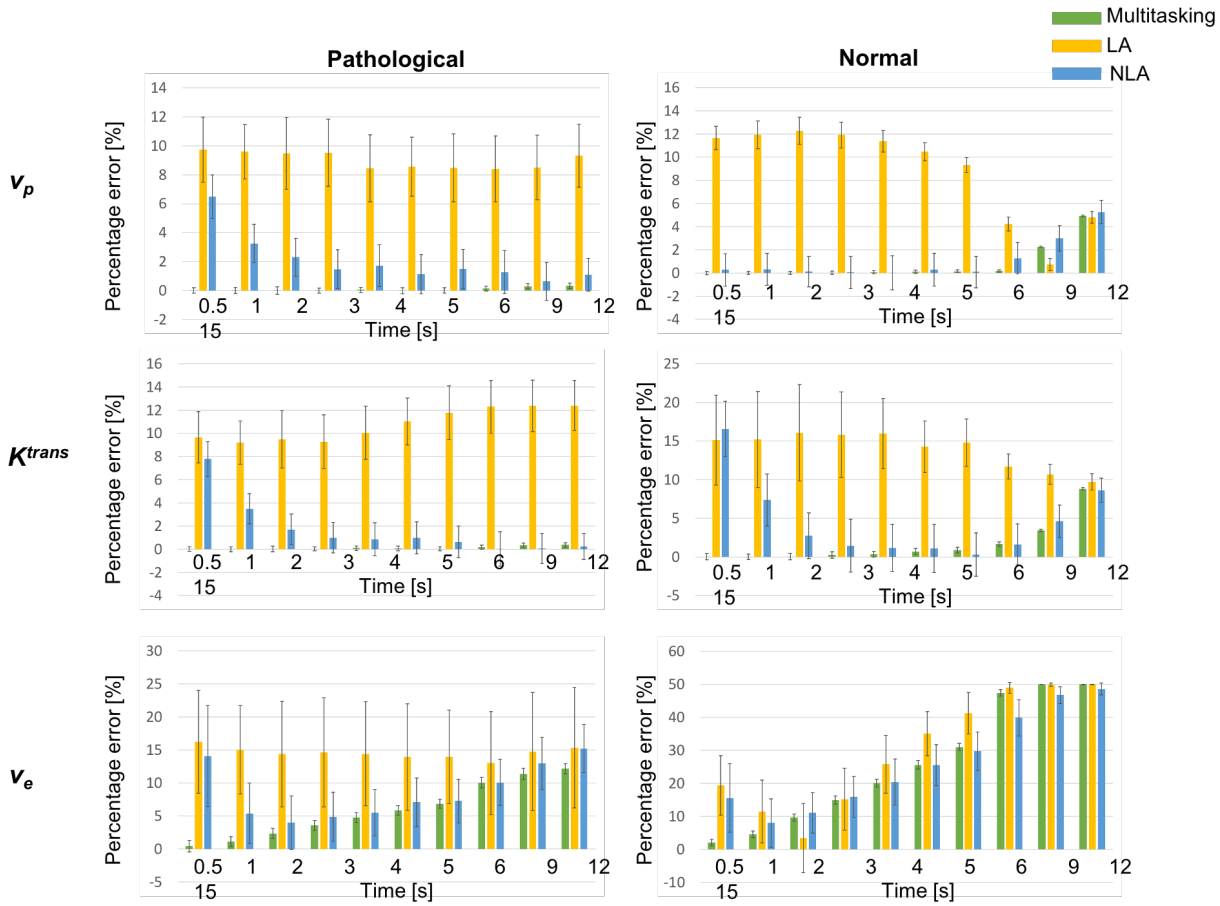


Figure 3.4: Simulation results for the comparison between Multitasking approach, LA, and NLA. Each bar graph displays the mean relative error of the estimated parameter at different temporal resolution. The error bar represents the relative standard deviation of 100 repetitions. When temporal resolution is high (<10 seconds), Multitasking approach showed best performance in the estimation of PK parameters, producing the smallest bias and standard deviation for both tissues and all parameters.

3.3.2 Phantom measurements

T1 maps collected for phantoms using Multitasking DCE and reference IR-SE are displayed in Figure 3.5 (A). The T1 values from Multitasking DCE were in good agreement with reference values ($R^2 = 0.96$), as shown in Figure 3.5 (B). Bland-Altman plots in Figure 3.5 (c) indicates that the mean absolute interscan difference of T1 mapping between separate Multitasking DCE scans are 1.68% with a variation for all vials within 10%.

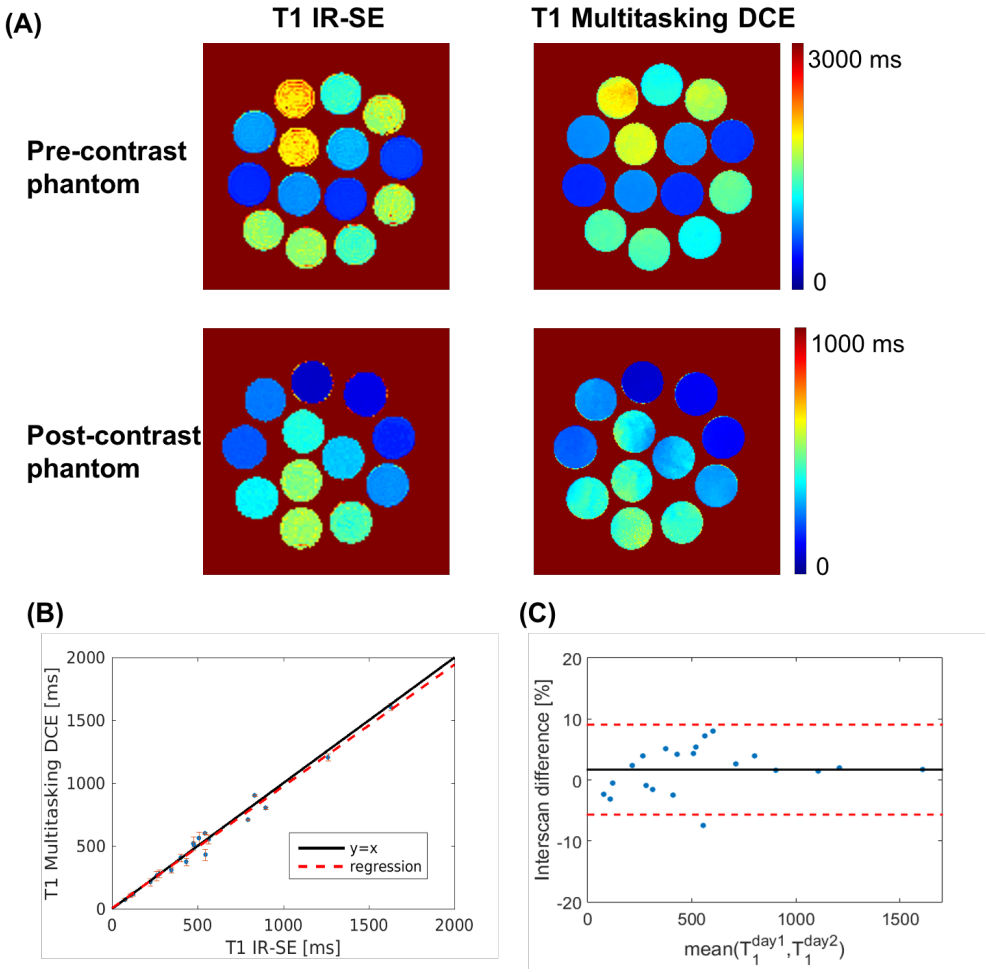


Fig 3.5: Phantom measurements. (A): T1 mapping of the pre- and post-contrast phantoms using Multitasking DCE and reference IR-SE. (B): Comparison of T1 quantification using the proposed Multitasking DCE versus a standard reference method (IR-spin echo). The solid black line represents y = x while the dashed red lines stands for the regression of the results from two methods ($R^2 = 0.96$). The error bar shows the standard deviation for each measured T1. (C): The Bland–Altman plot shows reproducibility of the T1 measurement of the proposed protocol measured on two different days. Solid line and dashed lines indicate the means and standard deviation of the T1 values between different measurement, respectively.

3.3.3 In vivo measurements

Figure 3.6 shows typical multi-dimensional images from Multitasking DCE in both coronal orientation, which provides an excellent view of entire carotid vessel along the direction of flow, and transversal orientation, which is useful for visualizing lumen and vessel wall condition. As previously states, there are 1,008 DCE phases, each of which contains 52 SR times in the proposed protocol. Figure 3.6 shows SR = 309 ms and SR =

595 ms (the final SR time) for three representative DCE phases: pre-contrast, peak-enhanced, and wash-out. Table 3.3 lists the comparison of T1 values between Multitasking DCE and MOLLI reference for healthy subjects.

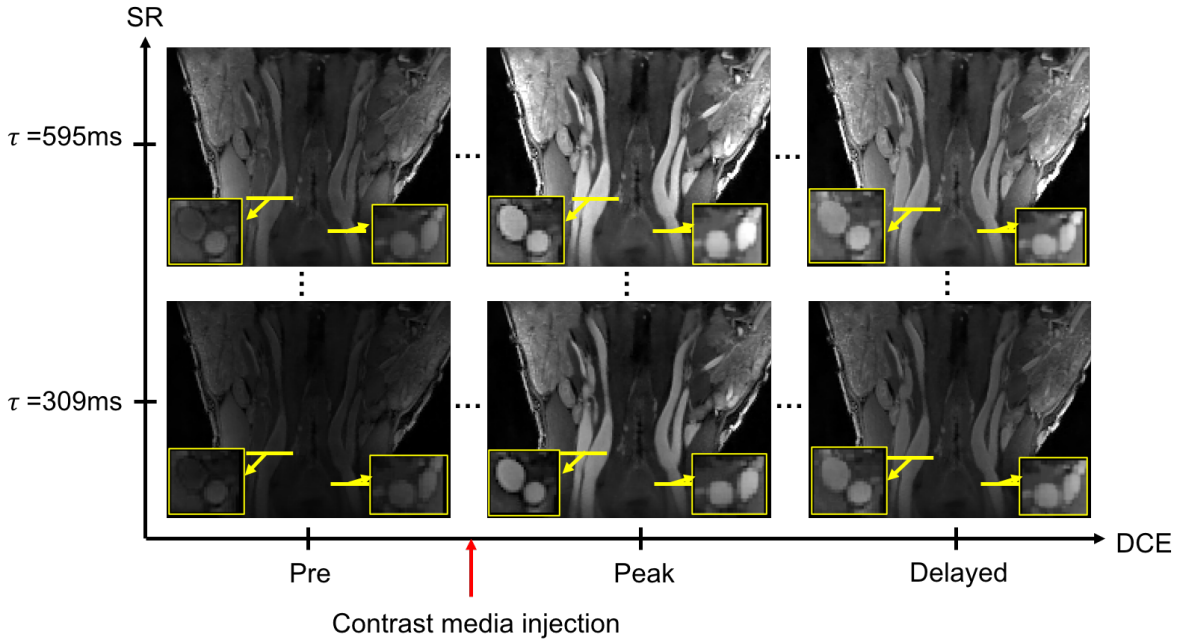


Fig 3.6: Representative image set from a study of a normal subject using the proposed method. Multi-phase images are reconstructed with the LRT framework in the SR dimension (images at different SR times) and dynamic enhancement dimension (images at different time after injection). Zoomed-in images are the transversal view of the locations marked by yellow lines. Multiple SR phases allows T1 quantification and direct estimation of contrast concentration. Three key DCE phases are shown along horizontal axis, including pre-injection, peak enhancement, and washing out. DCE temporal footprint is 1.2 s.

Table 3.3: MOLLI reference values in healthy subjects

	Pre-contrast T1 / ms			Post-contrast T1/ ms		
	DCE	MOLLI	ΔT1	DCE	MOLLI	ΔT1
Muscle	1219.1±114.5	1127.7±46.8	91.4	723.4±57.9	753.1±32.1	-29.7
Blood	1489.6±289.6	1401.9±264.3	87.7	439.3±31.6	428.6±26.3	10.7

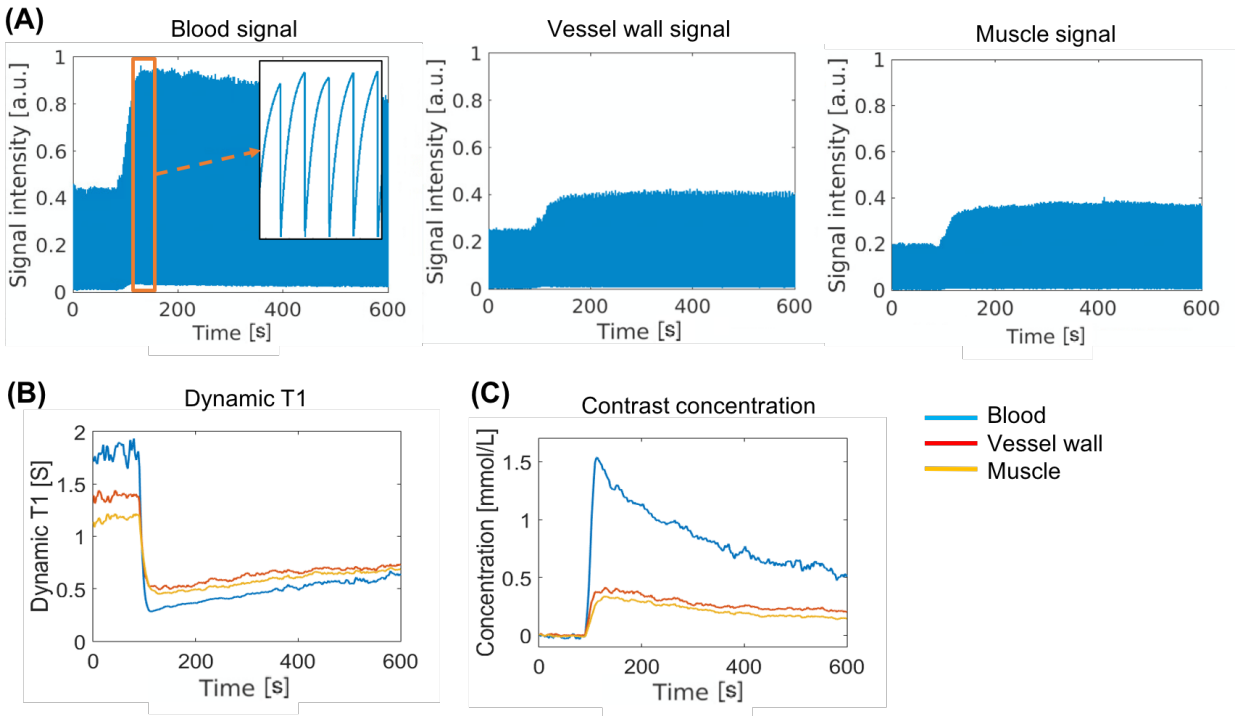


Fig 3.7: Real-time signal evolution of three representative tissues from a healthy subject. The zoom-in area in the image of blood signal shows the SR curves during the peak enhancement. (B) Dynamic T1 mapping based on the SR information. (C) Contrast agent concentration curves derived directly from the T1 mapping according to contrast media relaxivity.

Representative voxel-wise T1 fitting and conversion to CA concentration are illustrated in Figure 3.7. Subsequently, example parametric maps are shown in Figure 3.8. Figure 3.8 (A) shows a case of a normal subject with thin vessel wall. Figure 3.8 (B) and (C) show T1 weighted images and PK parameter maps from a patient with lipid-rich necrotic core and one with intra-plaque hemorrhage, respectively. The plaque composition was diagnosed clinically with the pre-contrast T1 TSE, T2 TSE and post-contrast T1 TSE images.

Bland–Altman plots in Figure 3.9 illustrate the inter-session repeatability of the PK parameters v_p, K^{trans}, v_e and AUC of the proposed method. The CV of v_p, K^{trans}, v_e and AUC were 4.62%, 4.24%, 3.50%, and 2.16%, respectively. The ICC of v_p, K^{trans}, v_e and AUC were 0.83, 0.87, 0.92, and 0.94, respectively.

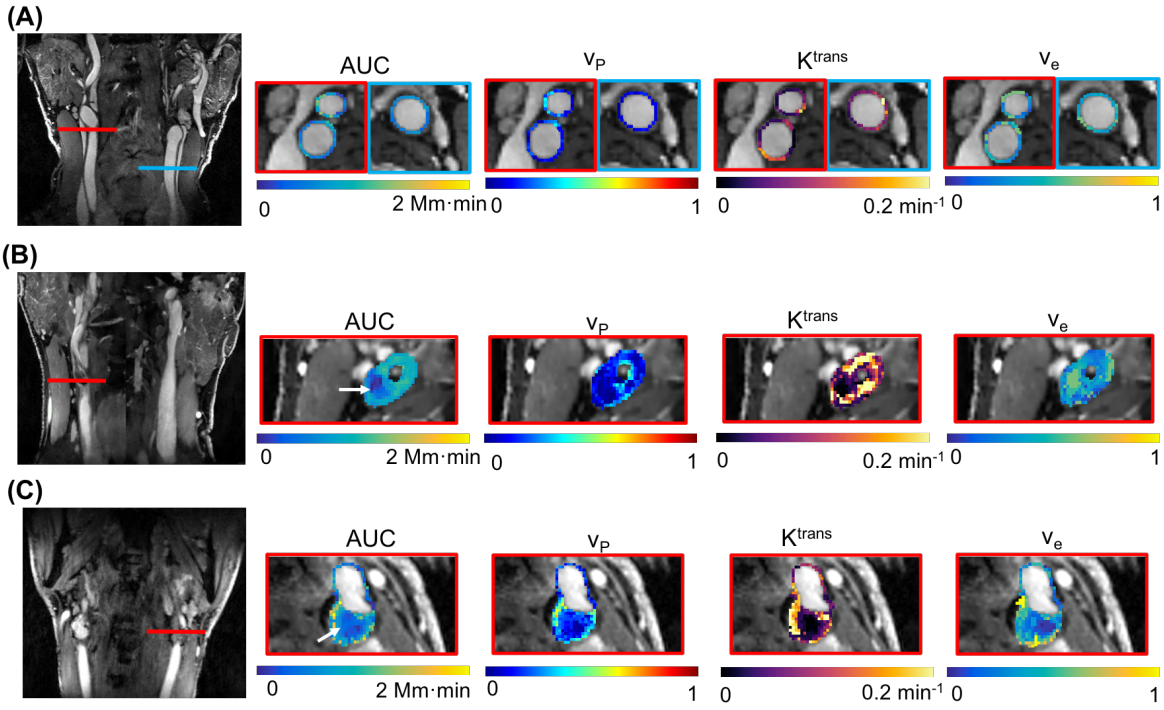


Fig 3.8: Real-time signal evolution of three representative tissues from a healthy subject. The zoom-in area in the image of blood signal shows the SR curves during the peak enhancement. (B) Dynamic T1 mapping based on the SR information. (C) Contrast agent concentration curves derived directly from the T1 mapping according to contrast media relaxivity.

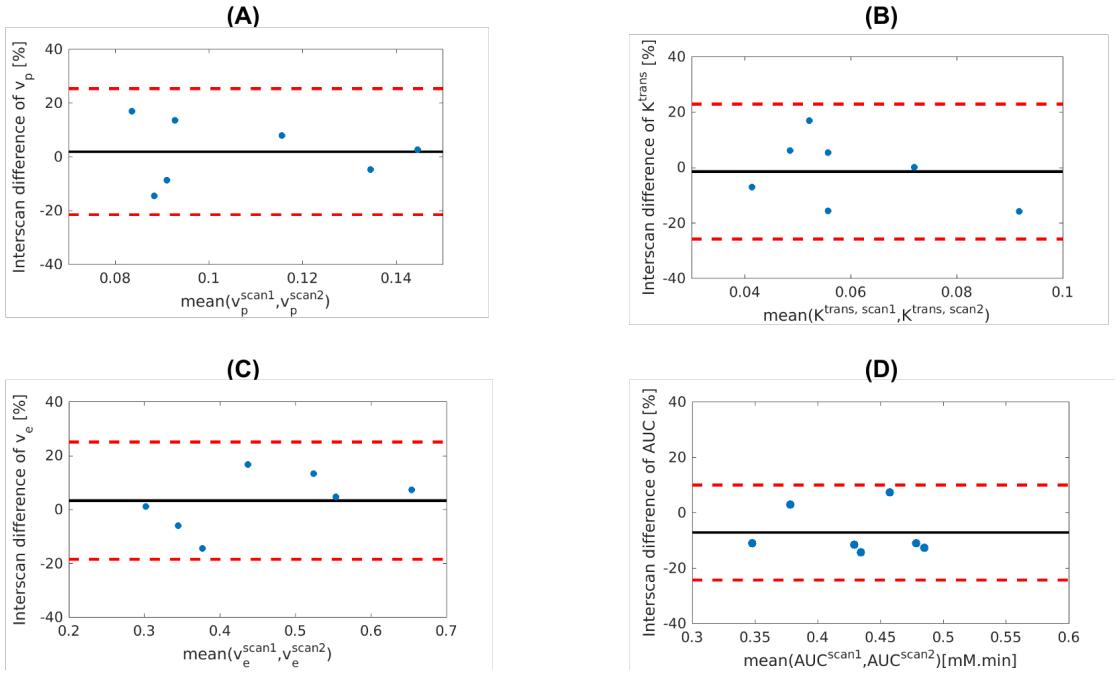


Fig 3.9: Real-time signal evolution of three representative tissues from a healthy subject. The zoom-in area in the image of blood signal shows the SR curves during the peak enhancement. (B) Dynamic T1 mapping based on the SR information. (C) Contrast agent concentration curves derived directly from the T1 mapping according to contrast media relaxivity.

Table 3.4 lists the mean and standard deviation measurements of v_p, K^{trans}, v_e and AUC in both the control group and patient group. The results for both groups were generally in agreement with published values from literature [70,96]. The ANOVA showed that v_p, K^{trans} and AUC were significantly higher in the patient group than in the control group (P = 0.034, <0.001, <0.001, respectively).

Table 3.4: Kinetic modeling properties in healthy subjects (n = 14) and patients with known carotid atherosclerosis (n = 7). For v_p, K^{trans} and AUC the mean values of patient group were significantly higher than the mean value of healthy group

	v_p	K^{trans} (min^{-1})	v_e	AUC (mM·min)
Control	0.11 ± 0.03	0.08 ± 0.02	0.49 ± 0.08	0.42 ± 0.12
Patient	0.14 ± 0.05	0.13 ± 0.04	0.54 ± 0.10	0.63 ± 0.13
P value	0.034	< 0.001	0.522	< 0.001

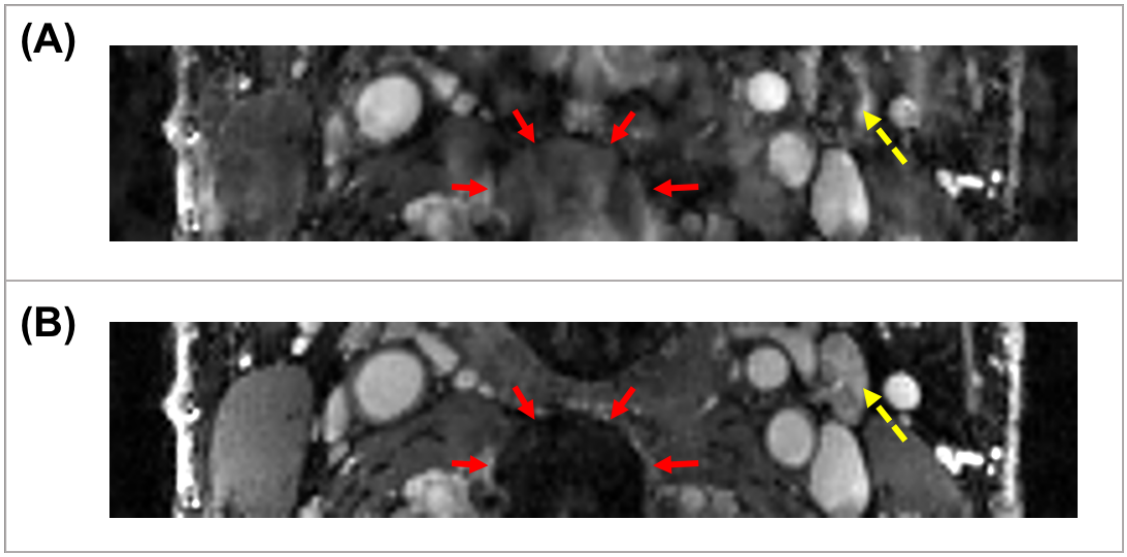


Fig 3.10: Effects of motion removal in the proposed method. Abrupt motion is a common issue in DCE studies. Without motion removal, images may be corrupted by artifacts. Reconstructed images with motion removal shows sharper and superior delineation of different tissue types. (A) is an image corrupted by motion artifacts. The set of red arrows mark a blurry structure. The dashed yellow arrow marks a vessel with corrupted contrast. (B) is the image from the same subject after motion removal. The area marked by red arrows has much clearer structure. The vessel marked by dashed yellow arrow has more reasonable contrast and better delineation

3.3.4 Effects of motion removal

Figure 3.10 shows an example of a motion-corrupted image (A) and the corresponding image after motion removal (B). The image quality parameters before motion removal is: SNR_{blood}=16.7, $SNR_{vessel\ wall}$ = 7.2, CNR = 9.5, sharpness = 2.68mm^{-1} (The signal intensity was normalized). After motion removal, the parameters are: SNR_{blood} = 74.8, $SNR_{vessel\ wall}$ = 30.4, CNR = 44.4, sharpness = 4.71mm^{-1}. All the parameters are substantially higher after motion removal, indicating better image quality and vessel wall delineation.

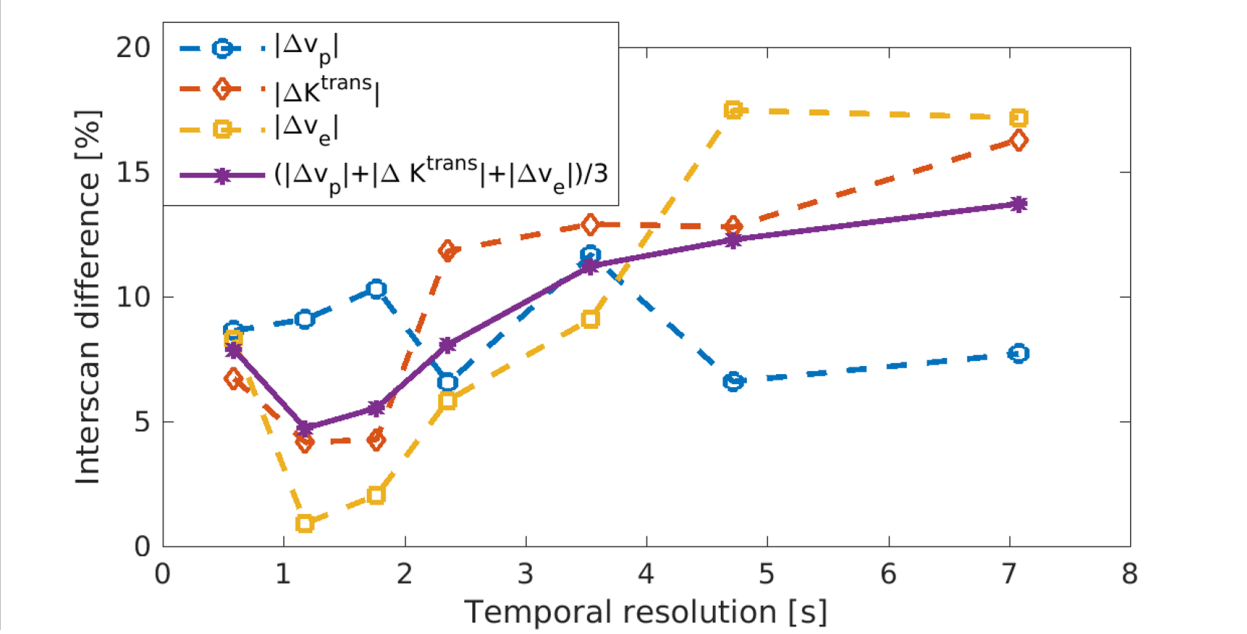


Fig 3.11: Reproducibility at different temporal resolution. The reproducibility between two scans was evaluated at different temporal resolutions retrospectively. The chosen temporal resolutions were 595 ms, 1.2s, 1.8s, 2.4s, 3.6s, 4.8s, and 7.2s. When temporal resolution<1s, the average reproducibility was not as good because of the reduced SNR. When temporal resolution>3s, the reproducibility decreased due to the worse depiction of fast-changing dynamic information. The best reproducibility achieved when temporal resolution = 1.2s

3.3.5 Inter-session repeatability at different temporal resolution

Figure 3.11 illustrates the mean absolute interscan differences of v_p, K^{trans} and v_e at different reconstructed temporal resolutions. Measurements of K^{trans} and v_e were most repeatable at the temporal resolution of 1.2 s, yielding interscan difference 4.2% and 0.9%, respectively, while v_p was most repeatable at the temporal resolution of 595 ms with 8.6% interscan difference. On average, the parameters were most repeatable at the temporal resolution of 1.2 s with the mean interscan difference (the mean value of the interscan difference of v_p, K^{trans} and v_e) of 4.7%.

3.4 Discussion

In this study, we presented a novel Multitasking DCE MRI method for the carotid artery. We achieved high spatial resolution, high temporal resolution, and complete carotid coverage with fully quantified T1 dynamics in a single 10-min scan. The feasibility of the proposed method was demonstrated in phantoms and in vivo.

Compared with previous work on carotid vessel wall DCE, the proposed method has multiple advantages. First, this technique allows 3D acquisition with large anatomical coverage and isotropic resolution at 0.7 mm. Previous findings showed that the imaging of carotid vessel wall requires a spatial resolution of at least 0.5–0.7 mm to capture the complex structure of plaque with limited partial volume artifacts and sufficient vessel wall/lumen delineation[23,112-114]. In most existing DCE protocols, the in-plane resolution can meet this requirement; however, slice thickness is typically equal to or larger than 2 mm in order to maintain sufficient SNR in 2D acquisitions[94,96], where lesions delineation would be compromised. In our method, the high isotropic spatial resolution would

significantly alleviate the limitation. It also allows flexible reformats of the images from any orientation, rendering optimal lesion visualization, especially in cases where the lesion is highly irregular and heterogeneous. Combined with the large anatomical coverage, the proposed method allows a comprehensive assessment of the disease extent.

Secondly, the proposed method can achieve a temporal resolution up to 595 ms, which can potentially capture the important dynamic information for AIF during the contrast enhancement[76,77]. The inter-session repeatability of PK parameters at different temporal resolutions were evaluated, indicating a temporal resolution at 1.2 second yields the best repeatability. The decreased repeatability at 595 ms was possibly due to its reduced SNR. When temporal resolution was higher than 1.2s, repeatability tended to decrease along with the decrease of temporal resolution, probably due to the obscure of the dynamic information. A major limitation of the current evaluation of temporal resolution is that the sample size is relatively small. Future evaluation with larger group of subjects is needed.

Thirdly, the CA concentration in Multitasking DCE is directly quantified by means of dynamic T1 mapping, as opposed to a linear approximation of contrast concentration from T1-weighted signal intensity (as in most of the current methods). The numerical simulation demonstrated the feasibility of the dynamic T1 mapping and the subsequent PK estimation using the proposed technique. To our knowledge, this is the first 3D protocol enabling dynamic T1 quantification.

The scan time in this work was set to be 9.8 min to collect sufficient data for the LRT reconstruction. In the recovery of the spatial coefficient $\mathbf{U}$, insufficient data can result in decreased image quality and reduced accuracy of the parametric fitting. In the future,

additional source of acceleration, such as partial Fourier acquisition may be adopted to further reduce the scan time.

The estimates of the PK parameters v_p, K^{trans}, v_e of control and patient groups are in line with the values published in literatures[22,70,94-96]. Among them, v_p and K^{trans} has been shown in a number of studies to correlate with the histological markers of inflammation[86]. In this work, v_p and K^{trans} in the patient group are both significantly higher than in the control group, which is consistent with previous studies. The correlation between v_e and inflammation biomarkers in carotid atherosclerosis has not been fully demonstrated yet. Besides, the estimate of v_e can be largely influenced by the total scan time because it relies on the presence of significant reflux. Previous work showed that a 7-min imaging period after CA administration is not enough to accurately estimate v_e[97]. Further investigations are needed to reveal the response of v_e in the inflammation of carotid atherosclerosis.

The proposed method requires further validation with histology. The capability of the proposed protocol in quantitatively assessing vasa vasorum was evaluated through the inter-session repeatability of the PK parameters. In addition, the consistency of the PK parameter values in our study and previously published literature is a support for the potential clinical value of the proposed protocol. In future, histological verification would elucidate the potential advantages of the proposed method in the diagnostic performance, including sensitivity, specificity, etc. compared with more conventional DCE approaches.

A potential limitation of the proposed technique is the lack of a black blood phase for vessel wall identification. The sequence we used in this work combined SR preparation and FLASH readouts. With SR preparation, the signal for all tissue types was

always positive during the recovery evolution. Any residual signal from the previous recovery period was reset to zero by the SR pulse, eliminating spin history issues during dynamic T1 mapping. In our study, the rim of the vessel wall was identified from the pre-contrast gray-scale images and the pre-contrast T1 maps generated with our method. In the future, inversion recovery preparation could be used in place of SR preparation, which would additionally yield black blood images at the blood null point for any DCE phase, potentially allowing better vessel wall identification. However, additional factors should be taken into consideration with inversion recovery. The extension of the magnetization recovery time to accommodate the full IR period could be subject to inflow effects. Also, during the dynamic process, residual magnetization would be carried over to subsequent recovery periods, which would have to be accounted for during T1 mapping.

3.5 Conclusion

We have demonstrated that the proposed Multitasking DCE MRI of carotid arterial wall is feasible with dynamic T1 mapping to achieve high spatiotemporal resolution and entire carotid coverage at the same time. The proposed method showed accurate T1 quantification, and robustness to motion in studies on phantom and healthy subjects. Preliminary patient studies were promising, and further validation is warranted in a larger clinical population.

CHPTER 4: SIX-DIMENSIONAL MULTITASKING DCE OF ENTIRE ABDOMEN: METHODS AND APPLICATION TO PANCREATIC DUCTAL ADENOCARCINOMA (PDAC)

4.1 Introduction

Pancreatic ductal adenocarcinoma (PDAC) represents 95% of malignant pancreatic cancers[115], which is the 3rd leading cause of cancer-related deaths in the US[116,117]. PDAC has an unusual microenvironment characterized by a highly desmoplastic stroma encompassing up to 90% of the tumor; regions with hypoxic tissue; interstitial hypertension; and heterogeneous vascularization including low MVD and reduced blood flow in the lesion area inherently resistant to treatment[25]. Due to technical challenges for early detection[16,118-120], approximately 60% of patients at the first diagnosis are deemed unable to receive macroscopic complete tumor resection, the only curative treatment option for PDAC[121]. Those patients who are ineligible for surgery will receive neoadjuvant chemotherapy or radiotherapy. However, the lack of effective approaches for early assessment of response to these therapies prevents optimization of the treatment design for each individual. The abovementioned reasons contribute to a dismal 5-year survival rate of 8%[122].

Because of its superior soft-tissue contrast, MRI plays a significant role in the detection, staging, and treatment management of PDAC[15,123,124].The clinical protocol includes T1W GRE imaging, T2W TSE imaging, DWI, and multi-phasic DCE MRI as introduced in Section 1.2.1. Multi-phasic DCE MRI has shown superior accuracy in the clinical evaluation of PDAC. To improve the quantification of vascular properties,

quantitative DCE MRI has also been introduced to investigate PDAC. Several studies have reported that K^{trans} and v_e are positively correlated with MVD and fibrosis in PDAC, respectively[24,25]. Other works have shown that quantitative DCE MRI can characterize PDAC and monitor treatment response[29,30].

However, abdominal DCE MRI continues to face demanding technical challenges, including the requirement to handle respiratory motion, the sub-optimized protocol due to the trade-off between spatial resolution, temporal resolution, and spatial coverage, and the difficulties to accurately quantify CA concentration, the as stated in Section 1.3[24,29,30,125,126 36,37,69]. To address the challenges, we improved the Multitasking DCE technique to perform 6-dimensional (6D) quantitative imaging with three spatial dimensions, a saturation recovery dimension, a respiration dimension, and a DCE time dimension. It achieves respiratory-motion-resolved, high-temporal-resolution T1 quantification of the entire abdomen in a 10-min free-breathing scan, followed by the derivation of contrast agent concentration and PK modeling. To our knowledge, this is the first abdominal DCE MRI method that simultaneously allows for 3D true free-breathing acquisition, 1-s temporal resolution, and dynamic T1 mapping.

4.2 Methods

4.2.1 Sequence design

Similar as in Chapter 3, 3D segmented FLASH readouts following periodic non-selective saturation-recovery (SR) preparation were used to acquire data at various SR times for dynamic T1 quantification[127]. Fat signal was suppressed by using water excitation for the FLASH readouts. Images were acquired in a transversal orientation,

covering the abdomen from the liver dome to the iliac crest. A 3D Cartesian trajectory with randomized Gaussian reordering in both phase (k_y) and partition (k_z) encoding was implemented to incoherently undersample k-space[127]. The collection of one center k-space line was interleaved with the collection of 7 imaging lines, yielding a sampling period of 45 ms for the training data. The orientation of the center k-space line was modified to the superior-inferior direction (partition encoding direction, $k_x = k_y = 0$) for the improved capture of respiratory motion.

4.2.2 Image reconstruction

In this work, the 6-dimensional image of abdominal Multitasking DCE $a(\mathbf{x}, \tau, t_r, t_d)$ with three spatial dimensions $\mathbf{x} = [x\ y\ z]^T$ and three time dimensions (saturation recovery time τ, respiration motion t_r, and DCE time course t_d) can be expressed as a 4-way tensor $\mathcal{A}$, which matrix notation is:

$$\mathbf{A}_{(1)} = \mathbf{U}\mathbf{G}_{(1)}(\mathbf{Q}\otimes\mathbf{W}\otimes\mathbf{V})^T, \tag{4.1}$$

where the columns of $\mathbf{U, V, W}$ and $\mathbf{Q}$ contain the basis functions for $\mathbf{x}$, τ, t_r, and t_d, $\otimes$ denotes the Kronecker product, and the subscript (i) denotes the mode-i flattening of the tensor[128]. The image tensor is recovered by sequentially determining each factor[79].

4.2.2.1 respiratory motion identification

To determine the respiratory motion states for each time point, dynamic images with a single time dimension were first generated using an explicit low-rank matrix imaging strategy, with the one temporal dimension t (elapsed time) representing a mixture of saturation recovery times, respiratory states and dynamic CA changes:

$$a(\mathbf{x},t) = \sum_{\ell=1}^{L} u_{\mathrm{rt},\ell}(\mathbf{x})\phi_{\mathrm{rt},\ell}(t), \tag{4.2}$$

where the single-time-dimension temporal basis function $\{\phi_{\mathrm{rt},\ell}(t)\}_{\ell=1}^{L}$ was estimated from the singular value decomposition (SVD) of the training data. Following this, the spatial coefficients $\{u_{\mathrm{rt},\ell}(\mathbf{x})\}_{\ell=1}^{L}$ were recovered by fitting the $\{\phi_{\mathrm{rt},\ell}(t)\}_{\ell=1}^{L}$ to the collected imaging data using a conjugate gradient least-squares algorithm[82].

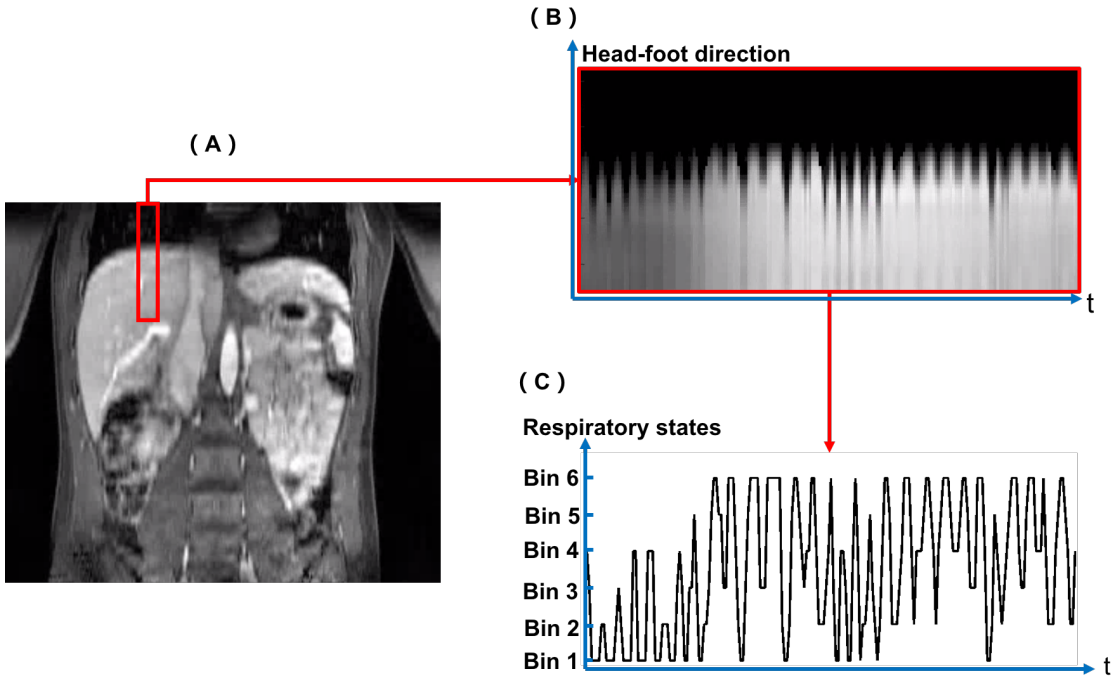


Figure 4.1: Respiratory binning scheme. (A) A narrow bar-shaped ROI in the head-foot direction was manually drawn on top of the liver-air interface. (B) The signal at each last-TI phase within the ROI was averaged over left-right direction as a 1D projection. The 1D projection over the duration of the scan formed a 2D spatial-temporal profile showing the location changes of the liver dome. (C) The position of the liver dome was extracted and then divided into 6 respiratory bins

Due to the relatively short SR repetition time (500 ms) in this work compared to a typical respiratory cycle (~3s), only the single-time-dimension images at the last saturation time of every SR period were used for respiration binning to avoid binning

errors introduced by variable T1 weighting. A narrow bar-shaped ROI in the head-foot direction was manually drawn on top of the liver-air interface. The signal at the last-saturation time points within the ROI over the duration of the scan formed a 2D spatial-temporal profile showing the location changes of the liver dome. After thresholding out the noise from the background, the position of the liver dome was extracted and then divided into 6 respiratory bins. The bins at other saturation times were then interpolated using a nearest-neighbor scheme. Figure 4.1 illustrates the scheme of the respiratory motion identification.

4.2.2.2 Respiratory motion compensation

To augment the correlation between images across different respiratory bins with minimal increase in the computational complexity, inter-bin translational registration was applied to the k-space data. To estimate translational motion, a template image of each bin was first obtained by averaging the single-time-dimension images within each respiratory state. The template image from end-expiration was set to be the reference, denoted as $\mathbf{a}_{\mathrm{ref}}$; the template images from the other five bins are denoted as $\mathbf{a}_i$, $i \in 1,2,\cdots,5$. The translation vector b_i between the moving bin i and the reference was estimated as

$$\widehat{b_i} = \arg\max_{b_i} Mt\left(\mathbf{F}^{-1}\left(\mathbf{P}(b_i) \circ (\mathbf{F}\mathbf{W}\mathbf{a}_i)\right), \mathbf{a}_{\mathrm{ref}}\right), \tag{4.3}$$

with spatial Fourier transform $\mathbf{F}$, a weighting window $\mathbf{W}$ that emphasizes the signal from moving organs of interest and reduces the signal from surrounding static muscle, linear phase modulator $\mathbf{P}(b_i)$ (the k-space operation equivalent to image-domain translation),

and mutual information metric $Mt(\cdot,\cdot)$. The k-space data was then directly compensated by applying $\mathbf{P}(b_i)$ to all k-space lines corresponding to the ith respiratory bin.

We note that the purpose of respiratory motion compensation was not to erase the difference of images between respiratory bins, but to increase the image correlation by moving them to a similar location, thereby improving image quality[129]. The superiority of respiratory motion compensation was tested by comparing the SNR in the pancreas and sharpness of the pancreas boundary with and without compensation using a one-tailed t-test. The sharpness of the boundary was estimated using the rise-distance method[109].

4.2.2.3 Tensor subspace estimation

Following respiratory motion identification and compensation, the next stage is to recover the multi-dimensional temporal factor $\mathbf{\Phi} = \mathbf{G}_{(1)}(\mathbf{Q}\otimes\mathbf{W}\otimes\mathbf{V})^T$ from the training data.

As described in Section 2.5.3 and Section 3.2.3, the first step is to pre-determine the T1 recovery basis functions in $\mathbf{V}$ from a dictionary of SR signal curves with 101 T1 values logarithmically spaced from 100 ms to 3000 ms, 17 flip angles from 6° to 14° in half-degree increments, and 21 saturation pulse angles linearly spaced from 60° to 120°. The T1 recovery factor $\mathbf{V}$ was directly extracted by applying SVD on the dictionary.

In the second step, the temporal tensor was recovered based on acquired training data $\mathbf{d}_{\mathrm{tr}}$ and the pre-determined $\mathbf{V}$. The training data were not available from every combination of respiratory state, SR time, and DCE phase, so the training data

tensor was highly undersampled. In addition, a motion removal scheme described in Chapter 3[127] was implemented to further remove outlier readouts corresponding to abrupt motion. The undersampled training data tensor was completed by solving:

$$\widehat{\mathcal{D}}_{\mathrm{tr}} = \arg \min_{\mathbf{D}_{\mathrm{tr},(2)} \in \mathrm{range}(\mathbf{V})} \|\mathbf{d}_{\mathrm{tr}} - \Omega_{\mathrm{tr}}(\mathcal{D}_{\mathrm{tr}})\|_2^2 + \lambda \sum_{i=1,3,4} \left\|\mathbf{D}_{\mathrm{tr},(i)}\right\|_* + R(\mathcal{D}_{\mathrm{tr}}) \qquad (4.4)$$

In this work, $R(\cdot)$ was chosen as temporal total variation (TV) along the respiratory and DCE dimensions: $R(\mathcal{D}_{\mathrm{tr}}) = \lambda_3 \left\|\boldsymbol{\nabla}\mathbf{D}_{\mathrm{tr},(3)}\right\|_1 + \lambda_4 \left\|\boldsymbol{\nabla}\mathbf{D}_{\mathrm{tr},(4)}\right\|_1$, where $\boldsymbol{\nabla}$ is the finite-difference operator. With the completed $\widehat{\mathcal{D}}_{\mathrm{tr}}$, the core-tensor $\mathcal{G}$, respiratory basis functions $\mathbf{W}$, and DCE time course basis functions $\mathbf{Q}$ can be extracted using the higher-order SVD (HOSVD)[130], which provides $\boldsymbol{\Phi} = \mathbf{G}_{(1)}(\mathbf{Q}\otimes\mathbf{W}\otimes\mathbf{V})^T$.

4.2.2.4 Spatial coefficient recovery

With a known temporal subspace spanned by the rows of $\boldsymbol{\Phi}$, the spatial factor $\mathbf{U}$ can be recovered by solving the following optimization problem:

$$\widehat{\mathbf{U}} = \arg\min_{\mathbf{U}} \|\mathbf{d} - \Omega(\mathbf{FSU}\boldsymbol{\Phi})\|_2^2 + R(\mathbf{U}) \qquad (4.5)$$

$R(\cdot)$ employs the anisotropic spatial TV: $R(\mathbf{U}) = \lambda \sum_\ell \left(\frac{1}{\Delta x}\|\nabla_x\{u_\ell(\mathbf{r})\}\|_1 + \frac{1}{\Delta y}\left\|\nabla_y\{u_\ell(\mathbf{r})\}\right\|_1 + \frac{1}{\Delta z}\|\nabla_z\{u_\ell(\mathbf{r})\}\|_1\right)$, where, e.g., Δx is the voxel width in x and $\nabla_x\{\cdot\}$ is the finite difference operator along x. The final result of the reconstruction produces the 6-dimensonal image with full T1 recovery curves for every combination of the respiratory states and multiple DCE phases.

4.2.3 Dynamic T1 quantification and PK modeling

Pixelwise dynamic T1 quantification was performed using the algorithm described in Section 3.2.4. Subsequently, the vascular properties were evaluated with the extended Tofts model (Equation 2.21) [131].

4.2.4 Imaging experiments

4.2.4.1 Imaging protocol

All studies were performed on a 3T clinical MR scanner (Biograph mMR, Siemens Medical Solutions, Erlangen, Germany) with a 12-channel phase array surface coil. In the imaging session, a routine protocol was first acquired for pancreas delineation and tumor definition. It included 3D T1W volumetric-interpolated-breath-holding imaging (T1-VIBE) with Dixon fat suppression in axial orientation, multi-slice T2W half-Fourier acquisition single-shot turbo spin-echo (T2-HASTE) in axial and coronal orientations, and multi-slice single-shot echo-planar imaging (SS-EPI) DWI. A 2D MOLLI[132] sequence in oblique planes covering as much PDAC tumor mass as possible was obtained as the reference for in-vivo T1 mapping. Following these sequences, the Multitasking DCE sequence was performed. The protocol was designed to cover the entire abdomen from the dome of the liver to the iliac crest. Each SR period was 500 ms with saturation times from 5.6 ms to 470.4 ms with an increment of 5.6 ms for T1 quantification. The SR period was repeated 1200 times in a scan of 10 min. The DCE bin duration was selected to be 1 s by combining two SR periods, striking a balance between temporal resolution and SNR[127]. Gd contrast agent (Gadavist, 0.1 mmol/kg, Bayer Schering Pharma) was administrated intravenously 2 minutes into the scan at a rate of 2 mL/s, followed by a 20 mL saline flush at the same rate. Immediately

at the end of this sequence, post-contrast MOLLI at the same slice location as pre-contrast MOLLI was collected. Detailed imaging parameters for the protocols are summarized in Table 4.1.

Table 4.1: List of imaging parameters

parameters	T1-VIBE	T2-HASTE	MOLLI	SS-EPI DWI	Multitasking DCE
Slice thickness (mm)	3	5	5	6	3
Slice resolution	50%	/	/	/	50%
Number of slices acquired	72	86	1	60	120
Gap	/	1	/	1	/
TR (ms)	4.15	1000	280.56	4500	5.60
TE (ms)	1.39/2.65(OP/IP)	99	1.12	47	2.45
Number of averages	1	1	1	6	1
FOV (mm^2)	350×280	330×226	390×390	339×306	380×268
In-plane resolution (mm^2)	1.2×1.2	1.3×1.3	2.0×2.0	2.0×2.3	1.2×1.2
Flip angle (◦)	9	105	35	90	10
Acceleration factor	3	2	2	2	/

4.2.4.2 Phantom study

The phantom study was performed on the ISMRM/NIST MRI system phantom (Model 130, High Precision Devices)[133] to validate the T1 mapping accuracy of the proposed Multitasking DCE technique. The T1 layer with T1 varying from 50 ms to 2000 ms was selected for data analysis. As a reference, a standard 2D IR-SE sequence with TR = 10000 ms and seven different inversion times (23, 100, 400, 900, 1600, 2200, 3000 ms) was also acquired at the center of the T1 layer with parameters: FOV = 220×220 mm^2, in-plane spatial resolution = 1.2 mm, slice thickness = 6 mm. Two

experiments with the same protocols were conducted on two separate days to assess the inter-session repeatability of T1 measurements in Multitasking DCE.

Table 4.2: Size and location of the tumor for all the patients. The size of the tumor is defined as the largest diameter in axial CT images according to RECIST 1.1 criteria.

Patient number	Tumor size (cm)	Tumor location
1	4.9	head
2	4.9	head
3	3.1	head
4	6.7	head
5	3.5	body
6	3.7	tail
7	2.6	neck
8	3.3	head
9	3.0	tail
10	3.9	neck
11	3.2	neck
12	4.0	body
13	1.3	head
14	6.6	body

4.2.4.3 In vivo study

The in vivo study was approved by the local institutional review board. Written informed consent was obtained from all participating subjects before scanning. The study population included both healthy subjects (as the control group) and patients with PDAC. Sixteen volunteers (8 females; aged 23 to 60 years old) without a history of

pancreatic disease were recruited as the control group; 8 of them were able to come back for a second scan with the same protocol on a different day (with at least one week apart from the first scan) for the assessment of inter-session repeatability.

For the patient study, the inclusion criteria were the presence of pathologically confirmed PDAC and tolerance to MRI and Gd-based contrast agent. Patients who had previously undergone pancreatic surgery were excluded from the study. The final patient group included 14 patients (7 females; aged from 51 to 77 years old). The mean size of the tumors, defined as the largest diameter in axial CT images according to RECIST 1.1 criteria, is 3.9 cm, ranging from 1.6 cm to 6.7 cm. The detailed size and location information of the tumor in the patient group are provided in Table 4.2. The previous clinical CE-CT scans and diagnosis reports for all patients were also obtained for tumor definition.

4.2.5 Image analysis

Post processing was performed off-line in MATLAB. The pancreas boundary of each subject was defined based on the T1-VIBE images from the same session. Dynamic T1 fitting and PK modeling were performed on all the slices involving pancreas, for all subjects.

In the control group, the PK parameters v_p, K^{trans}, v_e, and K_{ep} obtained for each subject are the mean values of all the voxels within the pancreas throughout multiple slices. For the patient group, the tumor boundary was identified by a radiologist (LW) with 11 years of experience in reading MR images for PDAC, by cross-referencing T1-VIBE, T2-HASTE, SS-EPI, and clinical CE-CT images. The PK parameters for PDAC

were the mean from all voxels within the tumor. The ROI for the non-tumoral area included all the voxels in the pancreas but outside the tumor.

4.2.6 Statistical analysis

Statistical analysis was conducted in SPSS (Version 24, IBM, NY, USA). The T1 measurement agreement between the Multitasking DCE and reference methods for both phantom and in vivo studies were evaluated by the intraclass correlation coefficient (ICC) and paired t-tests. The inter-session repeatability of the proposed technique was assessed on the repeated data from the 8 healthy volunteers who were scanned twice on separate days. Bland-Altman analysis, ICC and coefficient of variation (CoV) of the four PK parameters v_p, K^{trans}, v_e and K_{ep} were obtained.

A significance test using one-way unbalanced ANOVA was applied to identify the significant difference of each PK parameter obtained between (1) PDAC tumor mass and non-tumoral pancreatic tissue in the patient group, (2) PDAC tumor mass in the patient group and normal pancreatic tissue in control group, and (3) non-tumoral pancreatic tissue in the patient group and normal pancreatic tissue in control group. Holm-Bonferroni correction was also implemented to correct familywise error between this multi-group test.

4.3 Results

4.3.1. Phantom measurements

The colormaps in Figure 4.2 (A) display the T1 maps from the Multitasking DCE and reference IR-SE sequence. Figure 4.2 (B) shows the linear regression of the T1

measurements between the two methods, indicating that the T1 values from Multitasking DCE were in good agreement with reference values (linear regression slope = 0.972, R^2 = 0.970, ICC = 0.999). Across all spheres in the phantom, the T1 measured using Multitasking DCE shows no significant difference with the T1 measured by IR-SE (*P* = 0.073). The inter-session repeatability of the T1 mapping in Multitasking DCE was illustrated in Figure 4.2 (C). The mean absolute interscan differences were 2.55% with a relatively low CoV (9%), indicating that the T1 mapping of Multitasking DCE is repeatable.

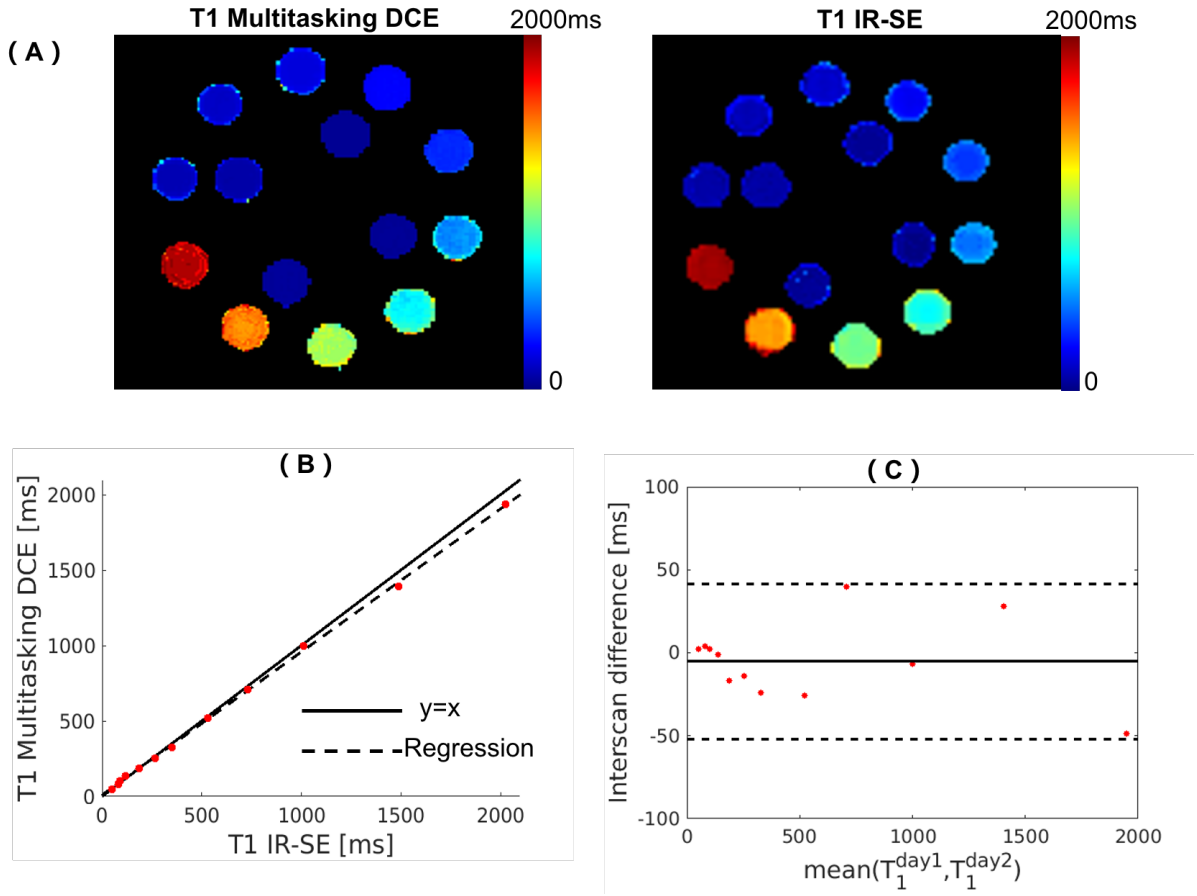


Figure 4.2: Phantom measurements. (A) T1 maps from the Multitasking DCE and reference IR-SE sequence of the T1 layer of ISMRM/NIST MRI system phantom. (B) Regression of T1 of the proposed Multitasking DCE versus IR-SE. The solid line represents y = x while the dashed lines stands for the regression of the T1 from two methods ($R^2 = 0.970$). (C) The Bland–Altman plot shows reproducibility of the T1 measurement of the Multitasking DCE measured on two different days. Solid line and dashed lines indicate the mean value and 1.96 of standard deviation of the T1 between different measurements, respectively.

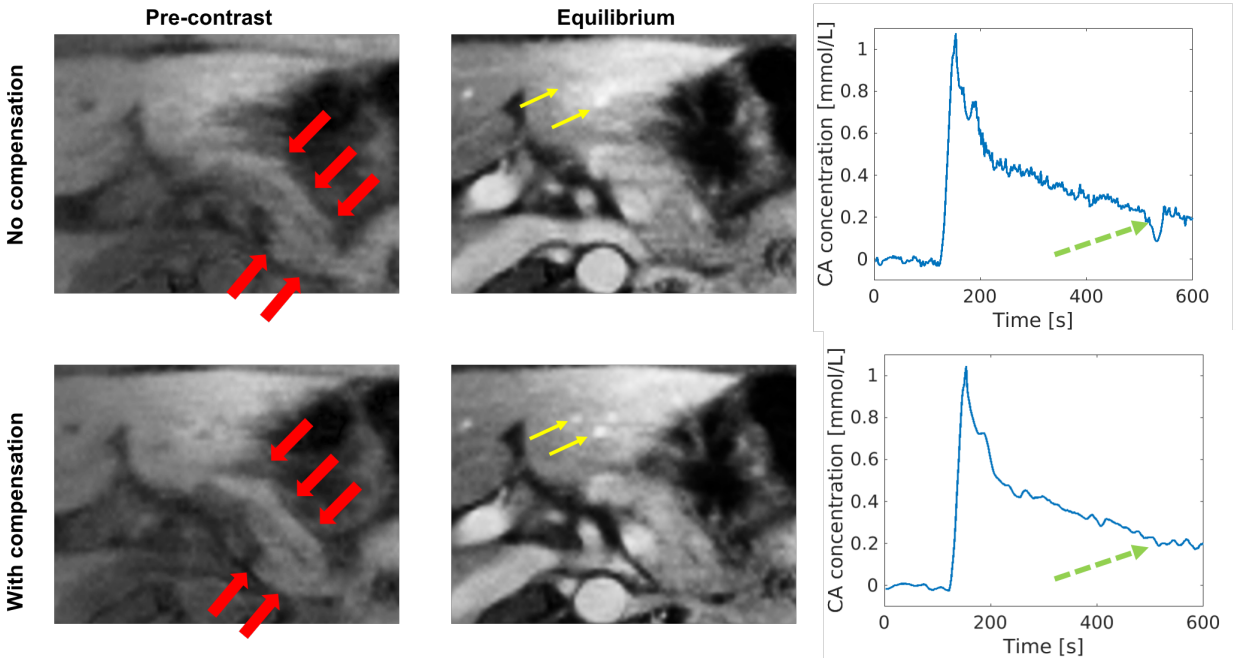


Figure 4.3: Effect of respiratory motion compensation. The images without and with respiratory compensation are shown at two DCE phases, one pre-contrast phase and one post-contrast phase. The CA concentration curve of pancreas are displayed. Images with compensation show less artifacts and improved structure delineation. The red thick arrows mark the pancreas, which is much sharper with less artifacts for both pre-contrast images with compensation. The yellow thin arrows mark small vessels, which shows clearer boundary and improved contrast on images with motion compensation. The green dashed arrows point out that the CA concentration curve with compensation is much cleaner with less oscillation.

Table 4.3: Comparison of SNR and SHP without motion compensation (NMC) and with motion compensation (MC) over all the cases (N = 30). One-tailed t test were applied and the P value are listed. The equilibrium phase is t_d = 4 min, where t_d is the time after injection

	SNR pre-contrast	SNR equilibrium	SHP pre-contrast (mm^{-1})	SHP equilibrium (mm^{-1})
NMC	29.83±14.21	35.22±13.07	0.39±0.15	0.49±0.16
MC	33.95±17.09	40.50±16.10	0.47±0.15	0.59±0.18
P value	0.006	0.008	0.013	<0.001

4.3.2. Effect of respiratory motion compensation

The respiratory motion compensation scheme was applied to all subjects. Figure 4.3 compares the image quality and CA concentration curves in the pancreas with and without respiratory motion compensation in a representative subject. The subject had an irregular respiratory pattern with non-uniformly distributed bins, resulting in poor image quality at bins with fewer image lines. In this example, respiratory motion compensation increased the inter-bin image correlation and thus improved image quality. The CA concentration curve with motion compensation is much cleaner with less oscillation from respiratory motion. SNR and sharpness (SHP) measurements before and after motion compensation for both pre-contrast and equilibrium phases (t_d = 4 min) are listed in Table 4.3 for comparison. A one-tailed t-test shows that motion compensation produced significantly superior SNR in the pancreas and SHP of the pancreas boundary (P = 0.006, 0.008, 0.013, <0.001, respectively).

4.3.3. In vivo measurements

The in vivo protocol including the conventional protocols and Multitasking DCE was successfully applied to all healthy volunteers and patients. A demonstration of the 6-dimensional images from Multitasking DCE is shown in Figure 4.4. As we described above, the DCE bin duration in the reconstruction was chosen to be 1 s, yielding 600 DCE phases, each of which contains 84 saturation times. Combined with 6 respiratory bins, the reconstructed image tensor possesses a total of $600 \times 84 \times 6 = 302400$ timepoints, each corresponding to a 3D (3 spatial dimensions) image volume. Figure 3 displays the images in either coronal or axial orientation at four key DCE phases (pre-

contrast phase, arterial phase with t_d = 20 s, venous phase with t_d = 60 s, and equilibrium phase with t_d = 4 min) at two saturation times and two respiratory states. Coronal orientation provides an appropriate view of the respiratory motion, while axial orientation shows excellent pancreas delineation. Video S1 in the supplementary materials further demonstrates the 6D images from Multitasking DCE.

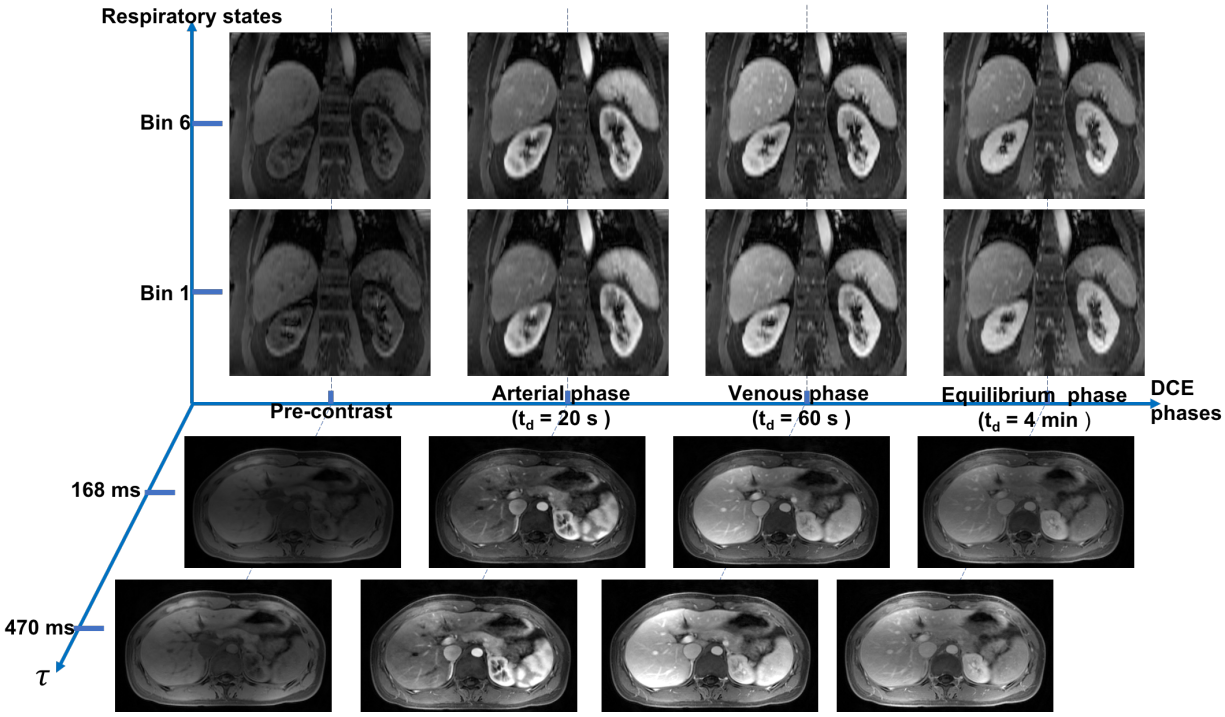


Figure 4.4: Representative 6D images with 3 spatial dimensions, a SR dimension, a respiratory dimension and a DCE time course. Images are displayed at pre-contrast phase, arterial phase (t_d = 20 s), venous phase (t_d = 60 s), and equilibrium phase (t_d = 4 min). For each DCE phase, images of end-inspiration (bin 1) and end-expiration (bin 6) phases at τ = 470 ms are shown in coronal orientation; images of different saturation recovery time τ (τ = 168 ms and τ = 470 ms) at end-expiration phase are shown in transversal view with clear pancreas delineation. t_d is the time from injection

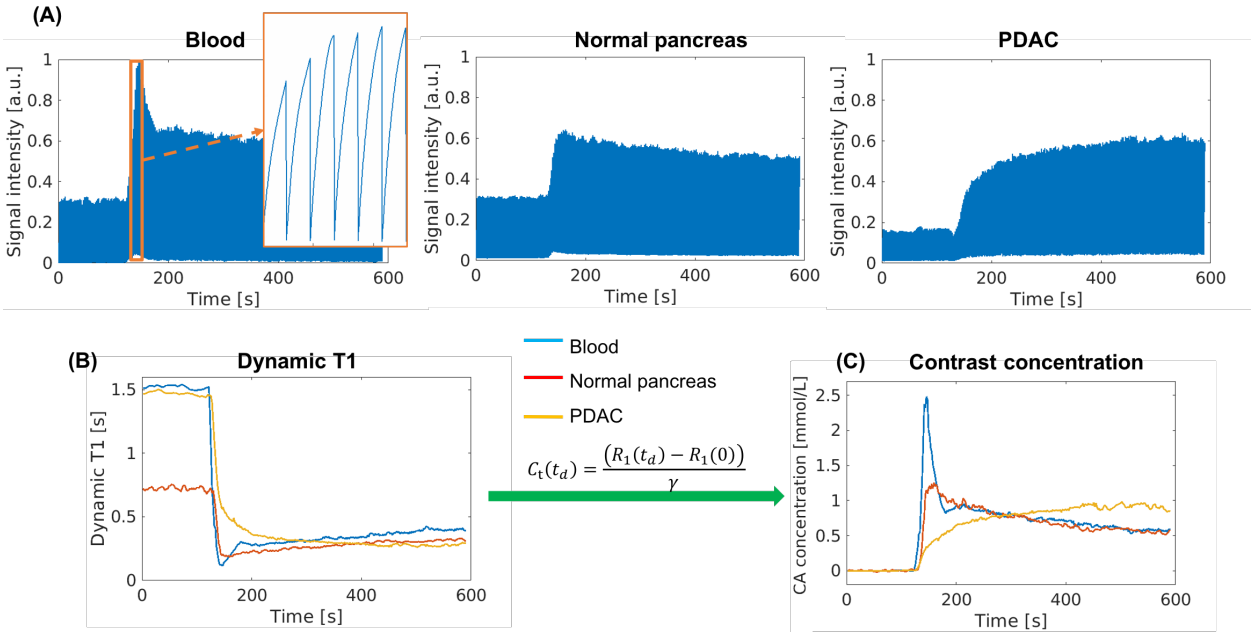


Figure 4.5: Transformation from signal intensity to contrast agent concentration. (A) Representative signal profiles of blood, normal pancreas and PDAC displayed at end expiration. The zoom-in area in the image of blood signal shows the SR curves during the peak enhancement. (B) Dynamic T1 mapping based on SR periods. (C) Contrast agent concentration curves derived directly from the T1 mapping according to contrast media relaxivity

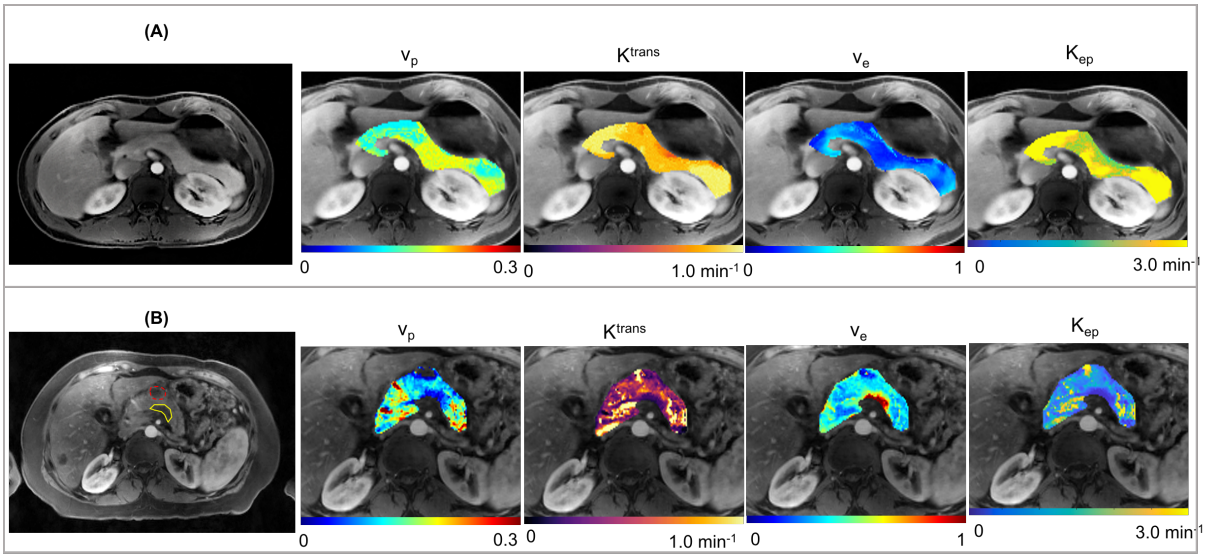


Figure 4.6: Representative maps of kinetic parameters of a 32-year-old subject in control group (A) and a 57-year-old subject with PDAC marked by yellow solid circle (B). The gray-scale image in each case is a transversal slice with excellent pancreas delineation at the arterial phase. The overlaid color maps display v_p, K^{trans}, v_e, and K_{ep} of the pancreas. In (B), the tumor region has lower v_p, K^{trans}, K_{ep} and higher v_e than the surrounding non-tumoral regions. The area marked by the red dashed line in (B) is a hypo-enhancing cyst.

The typical process of the conversion from dynamic signal to CA concentration is illustrated in Figure 4.5. Figure 4.5 (A) displays example signal intensity curves over all saturation times and DCE phases at end-expiration, displaying blood, normal pancreas, and PDAC mass. Figures 4.5 (B) and (C) show the corresponding dynamic T1 curves and contrast agent concentration curves for each of these tissues. The shape of the concentration curves is consistent with the findings in other studies[24].

The agreement of in vivo T1 measurements between Multitasking DCE and MOLLI was assessed for normal pancreas in the control group (denoted as control), PDAC mass in the patient group (denoted as tumor), and non-tumoral areas (denoted as non-tumor) in the patient group (Table 4.4). The ICC of the three categories for pre-contrast T1 (ICC = 0.820, 0.904, 0.973, respectively) and post-contrast T1 (ICC = 0.924, 0.958, 0.922, respectively) indicate good agreement of in vivo T1 measurements between Multitasking DCE and MOLLI; the P values given by paired t-tests for the three categories are 0.024, 0.180, 0.428, respectively, for pre-contrast T1, and is <0.001, 0.013, 0.043, respectively, for post-contrast T1.

Examples of the PK parametric maps are shown in Figure 4.6. Figure 4.6 (A) shows a healthy subject with a normal pancreas. The gray-scale images display the anatomical structure of a representative slice at the last saturation time of the arterial phase. The overlaid color voxels show the results of parametric mapping. Figure 4.6 (B) represents a PDAC case with tumor located within the pancreatic body. The tumor mass was marked by a yellow boundary on the gray-scale images by the radiologist, and a benign cyst is marked by a dashed red boundary.

Table 4.4: Comparison of in vivo T1 measurements between Multitasking DCE and MOLLI. The mean values and standard deviation of pre- and post-contrast T1 from Multitasking DCE and MOLLI are listed for healthy pancreas in control group, tumor and non-tumoral regions in patients. The ICC and P value by paired t-test between T1 measured by MOLLI and Multitasking are provided. The ICC of each category indicates good agreement of in vivo T1 measurement between Multitasking DCE and MOLLI.

		Multitasking (ms)	MOLLI (ms)	ICC	Paired t-test
Pre-contrast	Control	757±55	818±46	0.820	0.024
	Tumor	1571±210	1621±171	0.904	0.180
	Non-tumor	1183±338	1245±352	0.973	0.428
Post contrast	Control	419±74	470±80	0.924	<0.001
	Tumor	386±63	426±56	0.958	0.013
	Non-tumor	417±58	460±49	0.922	0.043

The inter-session repeatability of the PK parameters from our proposed Multitasking DCE method was also evaluated, with Bland-Altman plots shown in Figure 4.7. The ICC of v_p, K^{trans}, v_e and K_{ep} were 0.95, 0.98, 0.96, and 0.98, respectively. The CoV of the four parameters were 7.2%, 5.1%, 5.0%, and 2.6%, respectively.

Figure 4.8 contains a bar graph showing the mean and standard deviation measurements of v_p, K^{trans}, v_e and K_{ep} from the control, tumor, and non-tumor regions. The results for all categories were in general agreement with published values from literature[24,25,29,30]. An ANOVA analysis and Holm-Bonferroni tests indicated that all four parameters were significantly different between tumor with non-tumor (P = 0.002, 0.003, <0.001, 0.004, respectively) and between tumor and control (P = 0.0011, <0.001, <0.001, <0.001, respectively). The K^{trans}, v_e and K_{ep} between non-tumor and control also showed a significant difference (P <0.001, <0.001, =0.003, respectively). Detailed results of the statistical analyses are listed in Table 4.5.

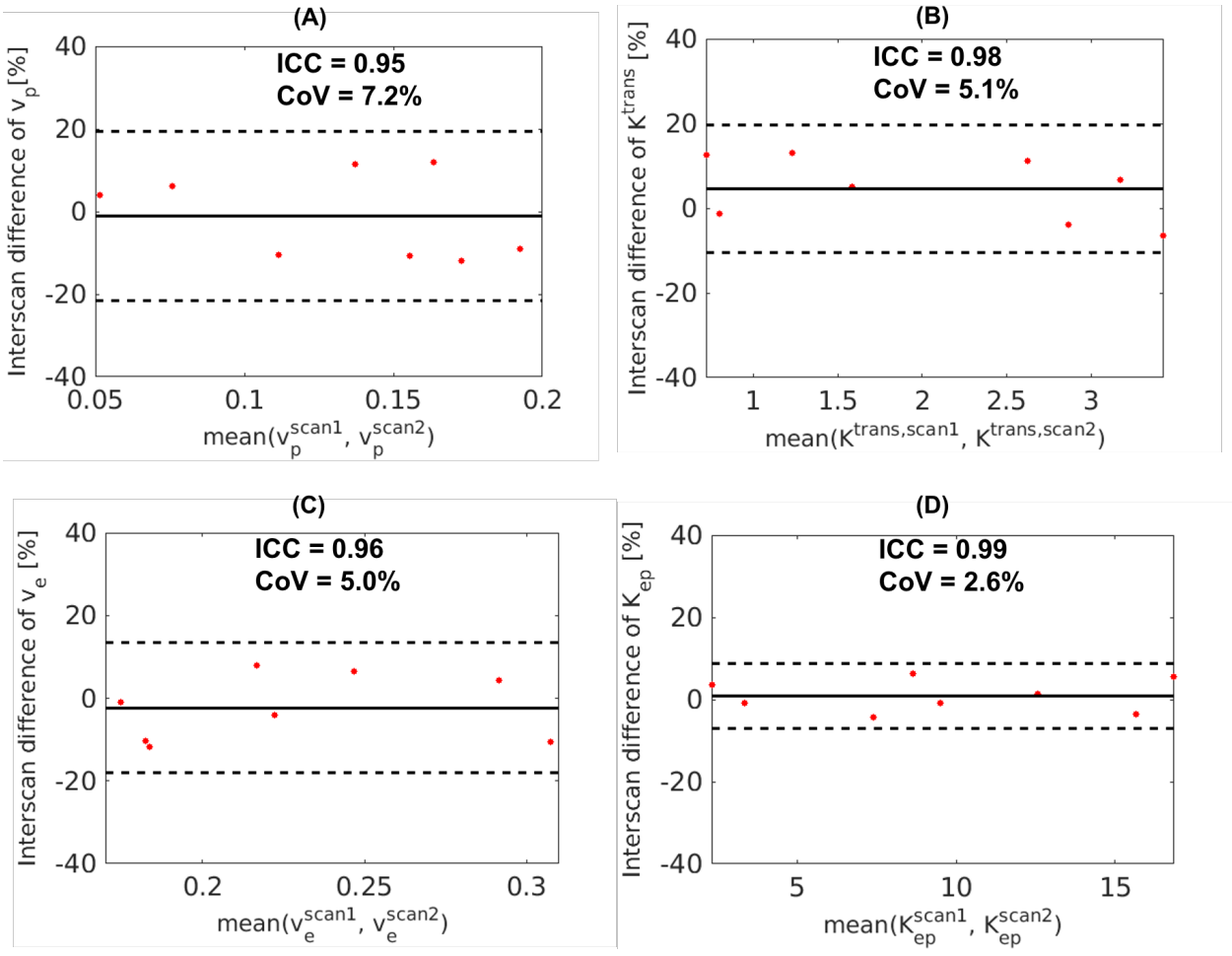


Figure 4.7: Bland-Altman plots evaluating the in vivo reproducibility of the kinetic parameters from Multitasking DCE on the eight subjects in control group who received the scan twice on separate days. The solid lines indicate the mean bias and the dashed lines indicate the 95% limit of agreement. The ICC and CoV of each parameter are listed on top of the corresponding plot

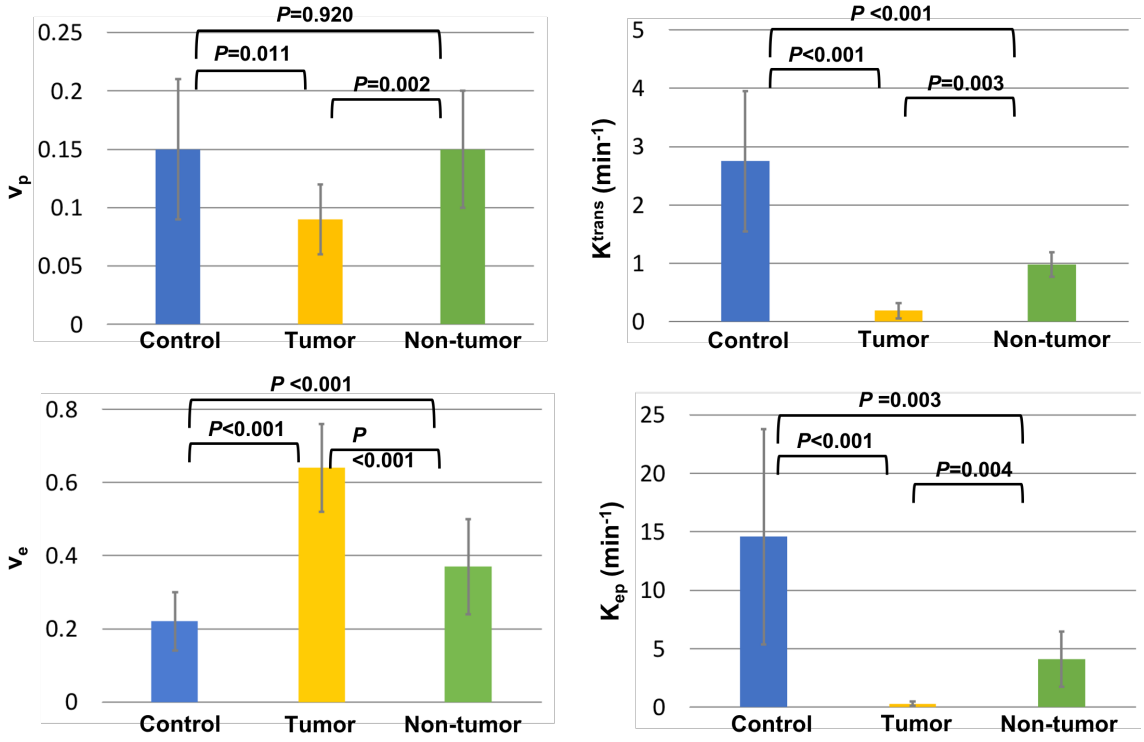


Figure 4.8: Bar graph showing the mean value and standard deviation of v_p, K^{trans}, v_e, and K_{ep} for control group, tumor and non-tumoral regions in patient group. The P values between each pair by one-way unbalanced ANOVA with Holm-Bonferroni correction are marked on top of the bar graph. All the four parameters were significantly different in the comparison between tumor and control and between tumor and non-tumor. The K^{trans}, v_e and K_{ep} between control and non-tumor also showed significant difference.

	v_p	K^{trans} (min^{-1})	v_e	K_{ep} (min^{-1})
Control	0.15±0.06	2.75±1.20	0.22±0.08	14.58±9.19
Tumor	0.09±0.03	0.19±0.13	0.64±0.12	0.30±0.19
Non-tumor	0.15±0.05	0.98±0.21	0.37±0.13	4.11±2.34
P value (Control vs Tumor)	0.011*	<0.001*	<0.001*	<0.001*
P value (Tumor vs Non-tumor)	0.002*	0.003*	<0.001*	0.004*
P value (Control vs Non-tumor)	0.920	<0.001*	<0.001*	0.003*

Table 4.5: Statistical result of v_p, K^{trans}, v_e, and K_{ep} for control group, tumor and non-tumoral regions in patient group. * indicate statistical significance

4.4 Discussion

DCE MRI has been widely applied in the study of permeability properties of lesions in oncology, especially in tumors of breast and pelvic organs[32,134-137]. Investigations have reported that permeability parameters derived from DCE MRI are associated with the histologic criteria[24,30,134-136]. However, only a limited number of studies have performed DCE MRI in the upper abdomen due to the challenges of adequate anatomical coverage, sufficient temporal resolution as well as the challenges posed by respiratory motion. In this study, we presented a 6D quantitative DCE MRI technique based on MR Multitasking and demonstrated its feasibility of the characterization of PDAC. Multitasking DCE enables 3D free-breathing acquisition, whole-abdominal coverage, high DCE temporal resolution of 1 s, and dynamic T1 mapping in a single 10-min scan, which overcomes all the aforementioned challenges and potentially facilitates the wide application of quantitative assessment of vascular properties in PDAC, including tumor characterization and treatment response monitoring.

The coverage in head-foot direction of Multitasking DCE is 360 mm from the liver dome to the iliac crest. The potential utility of the large coverage includes the evaluation of vasculature involvement of PDAC as well as the detection of abdominal metastasis of PDAC[138-140], which are vital information in the diagnosis and staging of the disease.

Sufficient temporal resolution is crucial to the quantification of DCE MRI. Othman et al. reported that a temporal resolution of at least 10 s/phase is required for the accurate diagnosis of cancer[35]. Several recent investigations have also shown that the acquisition of the AIF, which usually changes more rapidly than the tissue of interest,

requires a temporal resolution on the order of 1 s[76,77]. To achieve satisfactory temporal resolution, a tradeoff usually has to be made by reducing either the coverage or spatial resolution. For example, Akisik et al. used 2D T1W acquisition for three axial slices and one sagittal slice with 4.4-s temporal resolution[30]. Kim et al. implemented the KWIC technique, which allows k-space data sharing to reconstruct 3D images with high-spatial-low-temporal resolution or vice versa in one DCE session[29]. In this work, the proposed technique can achieve adequate coverage and spatial resolution with a high temporal resolution which can be retrospectively set based on the choice of DCE bin duration. Here it was retrospectively set to be 1 s to balance temporal resolution and SNR, as a similar temporal resolution also yielded the highest inter-session repeatability when evaluated in our previous work[127].

In addition, the contrast agent concentration in the proposed technique is directly quantified from dynamic T1 mapping to avoid the error introduced by linear approximation from T1W signal intensity. The feasibility of dynamic T1 fitting in Multitasking DCE has been assessed by numerical simulations in our previous work[127]. For the in vivo study, the pre-contrast T1 shows no significant difference between the MOLLI and Multitasking measurements for tumor and non-tumoral regions in PDAC group; a less than 10% difference ($P = 0.024$) was shown in controls, which may be due to known differences between various T1 mapping sequences[141]. The post-contrast T1 measured by Multitasking is systematically 10% shorter than the T1 from the MOLLI scan collected after Multitasking for all tissue types ($P < 0.001$, $P = 0.013$, $P = 0.043$, respectively). One possible reason is that contrast wash-out lengthened T1 during the time gap between the T1 measurement in the last DCE phase in Multitasking DCE and

the subsequent MOLLI scan, especially in cases where subjects moved during the scan and re-localization of the pancreas was required before the post-contrast MOLLI scan.

Another feature of the proposed Multitasking DCE is the capability to resolve respiratory motion. Respiration-induced motion artifacts are a major source of degraded image quality in abdominal MRI. Acquisition with breath-holds is the most common way to reduce these artifacts, which is often unreliable and in many cases infeasible. Radial sampling patterns are more robust to motion, but take longer for image reconstruction and can still result in blurring or streaking artifacts. XD-GRASP is a technique that separates respiratory motion states and uses sparsity constraints along different time dimensions. A recent publication of DCE MRI in liver using XD-GRASP described a protocol with 3D coverage and reasonable spatial resolution but a relatively low temporal resolution of 13 s and no T1 quantification[75].

The estimates of the PK parameters v_p, K^{trans}, v_e and K_{ep} of control and patient groups are generally in line with the values published in the literature[24,29]. K^{trans} and v_e have been shown to correlate with the MVD and fibrosis in PDAC lesions, respectively, and therefore can be used as imaging markers of the perfusion properties of tumor[24,25]. In the TK model, K^{trans} is dominated by the tissue blood flow and the capillary permeability–surface area and can have different physiological interpretations depending on the balance between the two factors[131]. In the context of PDAC, the microvessels in the lesions are leaky and in low density, leading to high permeability and limited blood flow, in which case K^{trans} is approximately equal to plasma flow per unit volume of tissue[131]. This is a possible pathological reason behind the decrease of K^{trans} value observed in malignant tumors compared to non-tumoral area in the patient

group and normal tissue in the control group. The v_e in the DCE MRI represents fractional extravascular extracellular space. The higher v_e in malignant tumor possibly results from the changes in the interstitial space due to the increased collagen content in the extracellular matrix. The non-tumoral area in PDAC patients are commonly associated with chronic obstructed pancreatitis caused by the obstruction of the main pancreatic duct or other physiological conditions also characterized by atrophy of the distal end towards the tail, reduced blood, and increased fibrosis[142,143], which may contribute to decreased K^{trans} and increased v_e in non-tumoral tissues in the patient group compared to the normal tissues in the control group[144-147]. Figure 5 suggests regional differences of PK parameters in the control group, which may be caused by the intrinsic heterogeneous tissue compositions in different parts of the pancreas[148]. Previous studies have shown that some imaging biomarkers such as ADC differ significantly between the head, body, and tail of the pancreas[149].

Our study had several limitations. All the patients recruited for this pilot study were undergoing chemotherapy at the time of the study. Chemotherapy may change the microvascular structures and thus the PK parameters, which limits the value of the current data to represent the vascular properties of untreated PDAC tumors. In addition, this pilot study had a relatively small number of subjects for both control and patient groups. With the encouraging findings of this work, further studies to validate the clinical utility of the proposed technique in a larger patient cohort with first diagnosed PDAC are warranted. Furthermore, tumor histological validation was not available for this pilot study. Instead, the capability of Multitasking DCE in quantitatively assessing tumor vascular properties was evaluated by the inter-session repeatability of the PK

parameters. The PK parameters are consistent with the values in the published literatures. In future studies, the correlation between the PK parameters and the histological parameters including the MVD and fibrosis should be assessed.

4.5 Conclusion

A novel Multitasking abdominal DCE technique was developed, enabling free-breathing and respiratory motion-resolved image acquisition, entire-abdominal coverage, 1-s temporal resolution, dynamic T1 quantification, and PK modeling. Quantitative DCE parameters from the preliminary in vivo study were repeatable and showed significant differences between normal pancreas, tumor and non-tumoral regions in PDAC patients.

CHAPTER 5: DIFFERENTIATING PANCREATIC DUCTAL ADENOCARCINOMA AND CHRONIC PANCREATITIS USING SIX-DIMENSIONAL QUANTITATIVE MULTITASKING DCE

5.1 Introduction

Chronic pancreatitis (CP) is a fibro-inflammatory disease characterized by progressive and irreversible functional and morphological changes caused by a variety of etiological factors[150-152], resulting in permanent impairment on both exocrine and endocrine functions. The gold standard diagnostic test of CP is histology/ biopsy. However, tissues sampling of pancreas, due to its retroperitoneal location, is challenging and carries substantial risk of bleeding and acute pancreatitis[151]. In recent years, the value of MRI in the assessment of full spectrum of pancreatic diseases has been increasingly realized. Qualitative multi-phasic DCE MRI and MR cholangiopancreatography (MRCP) have been used to detect CP in human, yielding promising results.

However, one major obstacle in the accurate diagnosis of CP and other pancreatic diseases is the difficulties to differentiate CP with PDAC. CP and PDAC may present with same symptoms and signs, and share similar radiologic features, including ductal abnormalities, mass lesions, or cystic lesions[153,154]. The association of CP and PDAC can further enhance the complexity to distinguish these two entities. The presence of CP can significantly increase the risk for developing PDAC at 8-fold in 5 years[153,155]. PDAC tends to obstruct the pancreatic duct, which can result in associated CP, especially in the upstream of pancreas. Previous studies have shown that the incidence of pancreatic

cancer in patients with CP is estimated to be 1~6%[153]. On the other hand, approximately 5-10% patients receiving surgery for suspected malignancy were found to have benign pancreatitis, which can expose them to the risk of morbidity and mortality due to the resection. Therefore, to develop clinical tools that can accurately differentiate CP and PDAC preoperatively is of great significance.

Several studies have reported that semi-quantitative DCE MRI with the evaluation of the pattern of dynamic signal intensity curves can characterize CP[144,151] and provide reliable information to distinguish CP and PDAC[146,147,156]. However, those semi-quantitative parameters are intrinsically non-specific, which can lead to overlaps in the findings of CP and PDAC[157]. Quantitative DCE parameters with Tofts model, such as v_p and K^{trans}, were demonstrated to be able to present the vascular properties of tissues and has been applied in the characterization of PDAC. However, demanding technical challenges (as described in Section 4.1), including the need to handle respiratory motion, the conflict among the requirements for coverage, spatial, and temporal resolution, and the nonlinearity between signal intensity and CA concentration, has significantly limited the application of quantitative DCE in the study of CP.

In addition, blood flow is an important pathological characteristic for CP and PDAC, both of which are identified with reduced blood flow. Some more generalized PK models such as 2CXM has the ability to estimate blood flow, v_p, K^{trans}, and v_e simultaneously. Nonetheless, accurate evaluation of blood flow using those models requires improved temporal resolution, which is impractical given the abovementioned challenges.

In this work, the 6D Multitasking DCE technique proposed in Chapter 4 were applied to address the abovementioned limitations and quantitatively evaluate the

perfusion and vascular properties of normal pancreas, CP and PDAC. This technique enables respiratory-motion-resolved, high-temporal-resolution T1 quantification of the entire abdomen in a 10-min free-breathing scan. PK model 2CXM was chosen to evaluate F_p, v_p, K^{trans}, and v_e altogether. To our knowledge, this is the first work using DCE MRI to evaluate both blood flow and vascular properties for CP and PDAC.

5.2 Methods

5.2.1 Study population

The in vivo study was approved by the local institutional review board. Written informed consent was obtained from all participating subjects before scanning. In addition to the healthy subjects (N = 16, 8 females; aged 23 to 60 years old) and patients with PDAC (N = 14, 7 females; aged from 51 to 77 years old), a group of patients with CP (N = 7, 4 females; aged from 30 to 72 years old) were recruited. All the subjects for CP group had diagnosis established by MR cholangiopancreatography (MRCP) or endoscopic retrograde cholangiopancreatography (ERCP) with Cambridge classification for CP. Patients allergic to GBCA or with renal disease were excluded. The final CP group consisted of 8 patients (4 females) aged from 30 to 72 years old.

5.2.2 MRI protocol

All the included subjects received the MRI studies performed on a 3T clinical MR scanner (Biograph mMR, Siemens Medical Solutions, Erlangen, Germany) with a 12-channel phase array surface coil. In the imaging session, a routine protocol for pancreas delineation was first acquired, including 3D T1-VIBE with Dixon fat suppression in axial

orientation, multi-slice T2-HASTE in axial and coronal orientations, and multi-slice SS-EPI DWI. The Multitasking DCE sequence was performed subsequently using the same parameters specified in Table 4.1. GBCA (Gadavist, 0.1 mmol/kg, Bayer Schering Pharma) was administrated intravenously 2 minutes into the scan at a rate of 2 mL/s, followed by a 20 mL saline flush at the same rate.

5.2.3 Image Analysis

Image reconstruction and post processing was performed off-line in MATLAB. 2CXM were applied to model the perfusion and permeability parameters:

$$C_{\mathrm{t}}(t) = F_{\mathrm{p}} \cdot C_{\mathrm{p}}(t) * \left(Me^{-\alpha t} + (1-M)e^{-\beta t}\right), \tag{5.1}$$

with the AIF $C_{\mathrm{p}}(t) = C_{\mathrm{b}}(t)/(1-\mathrm{Hct})$. With fitted F_{p}, M, α, and β, other required kinetic parameters v_{p}, K^{trans}, and v_{e} can be calculated using following equation:

$$v_{\mathrm{p}} = \frac{F_{\mathrm{p}}}{M\alpha + (1-M)\beta},\ K^{\mathrm{trans}} = F_{\mathrm{p}}\frac{M(1-M)(\alpha-\beta)^2}{M\alpha^2 + (1-M)\beta^2},\ v_e = v_{\mathrm{p}}\frac{M(1-M)(\alpha-\beta)^2}{\alpha\beta} \tag{5.2}$$

The pixelwise PK modeling using 2CXM was applied to all the pancreas data (control, PDAC, and CP groups). For CP group, the outcomes of PK parameters for each subject were the mean values over all the voxels within the pancreas throughout multiple slices. The pancreas boundaries for CP patients were defined based on the T1-VIBE by the radiologist (LW). The ROIs for normal pancreas, PDAC mass, and non-tumoral area were the same as obtained in Chapter 4.

5.2.4 Statistical Analysis

Statistical analysis was conducted in SPSS (Version 24, IBM, NY, USA). A significance test using one-way unbalanced ANOVA was applied to identify the significant

difference for each PK parameter obtained between multiple groups of tumor mass (denoted as PDAC) in the PDAC group, non-tumoral pancreatic tissue (denoted as NT) in the PDAC group, disease pancreas in the CP group (denoted as CP), and normal pancreas in the control group (NP). *P*<0.05 was considered significant.

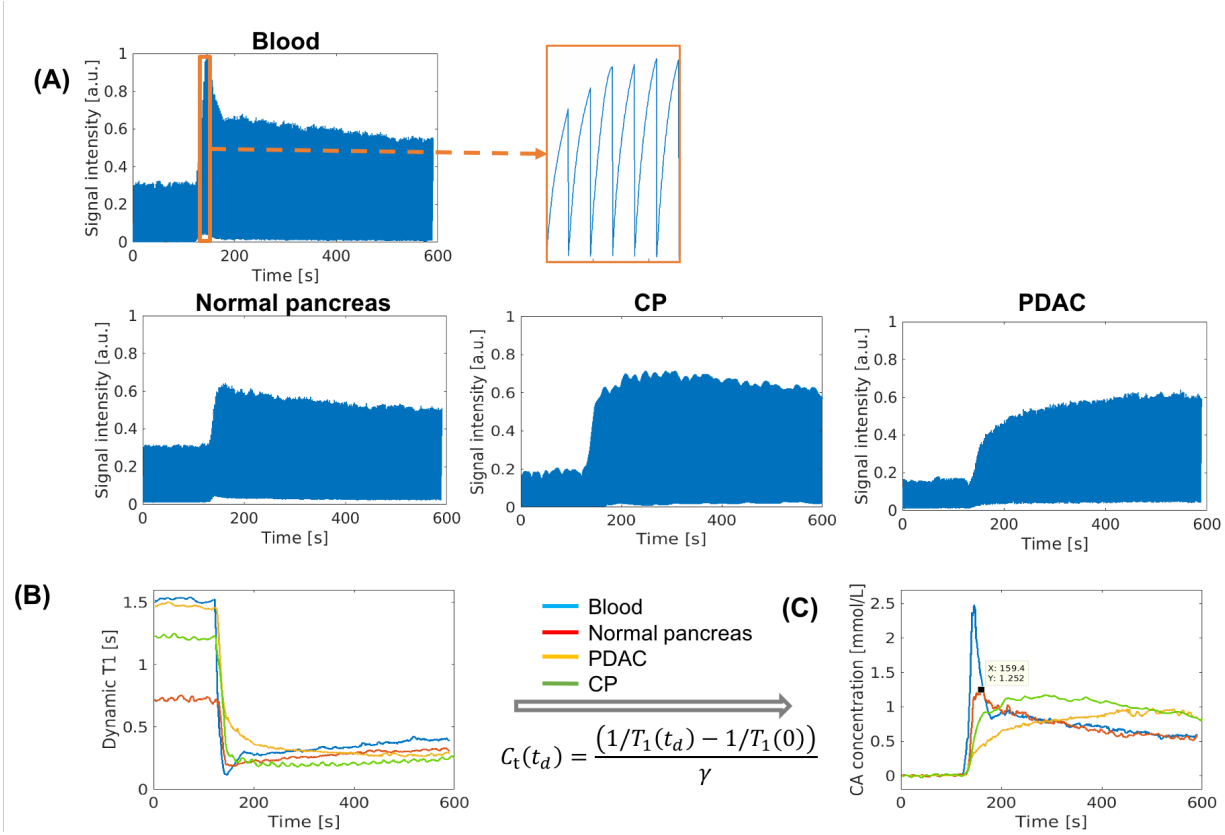


Figure 5.1: Conversion from signal intensity to CA concentration. (A) Representative signal profiles of blood, normal pancreas, CP and PDAC displayed at end expiration. The zoom-in area in the image of blood signal shows the SR curves during the peak enhancement. (B) Dynamic T1 mapping based on SR periods. (C) CA concentration curves derived directly from the T1 mapping according to contrast media relaxivity.

5.3 Results

The imaging experiments and reconstruction were successfully performed on the 8 patients with CP, followed by the estimation of PK parameters using 2CXM for the CP group and the previous control and PDAC groups. Figure 5.1 displays the typical transition from signal intensity curves in Multitasking DCE to the CA concentration based

on dynamic T1 mapping from representative cases. In general, there are differences in the shape of the CA concentration curves between normal pancreas, PDAC, and CP, implying differentiated vascular properties for the tissues.

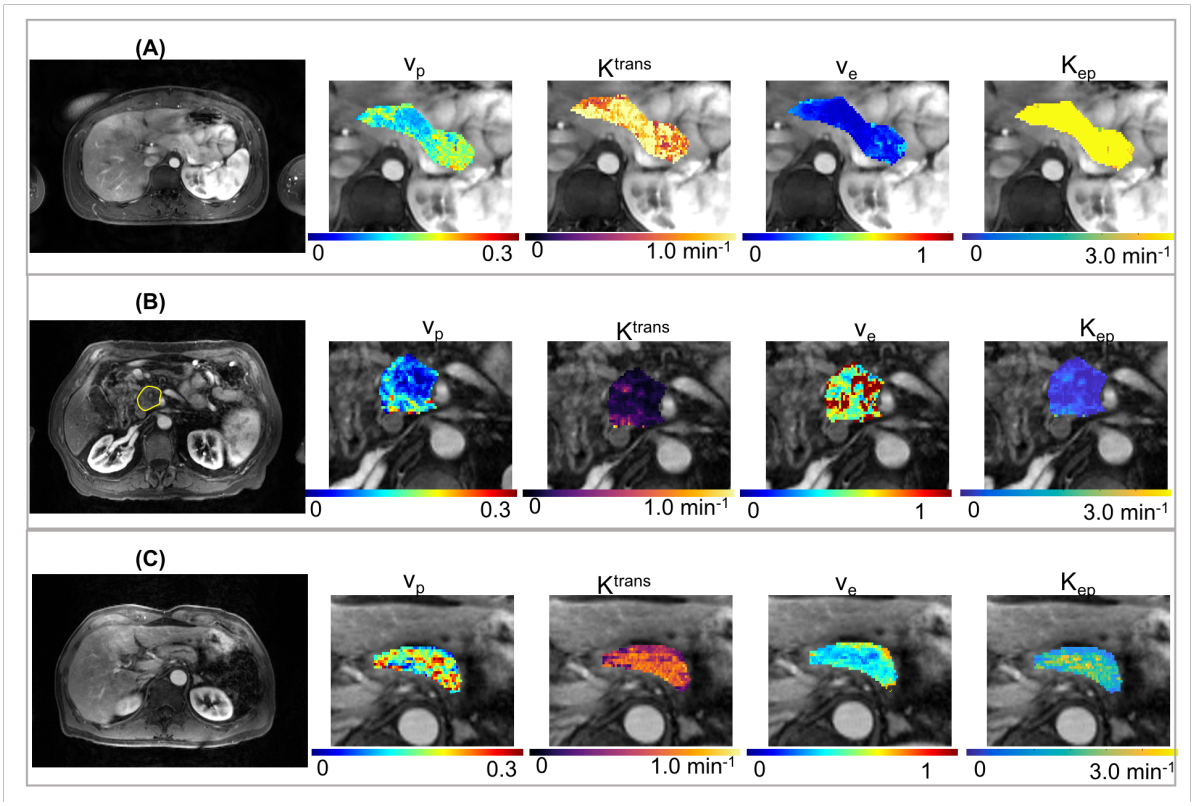


Figure 5.2: Representative maps of kinetic parameters of a 25-year-old subject in control group (A), a 77-year-old subject with PDAC marked by yellow solid circle (B), and a 65-year-old subject with CP. The gray-scale image in each subfigure is a transversal slice at the arterial phase. The overlaid color maps display v_p, K^{trans}, v_e, and K_{ep} of the pancreas

Example PK parametric maps are displayed for a healthy subject (Figure 5.2 (A)), a patient with PDAC (Figure 5.2 (B)), and a patient with CP (Figure 5.2 (C)). The gray-scale images display the anatomical structure of a representative slice at the last saturation time of the arterial phase. The overlaid color voxels show the outcomes of parametric mapping.

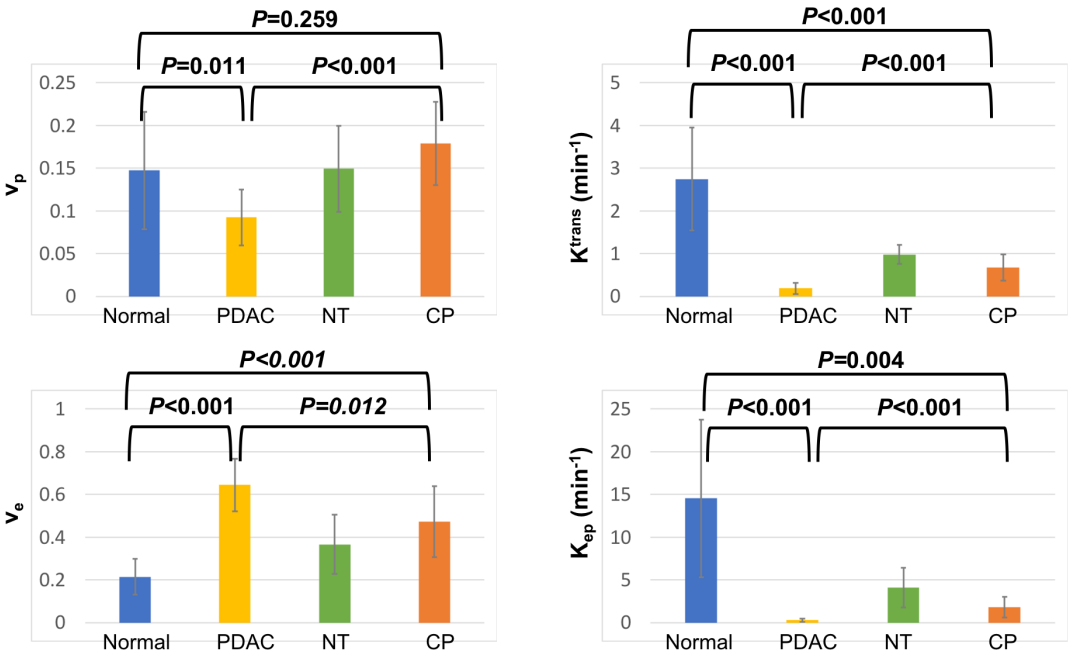


Figure 5.3: Bar graph showing the mean value and standard deviation of v_p, K^{trans}, v_e, and K_{ep} for control group, PDAC, non-tumoral regions in PDAC group (denoted as NT), and CP. The P values between PDAC versus CP, PDAC versus normal, and CP versus normal are labeled on top of each sub-graph. All the four parameters were significantly different in the comparison between PDAC versus CP and between PDAC versus normal. The K^{trans}, v_e and K_{ep} between CP and normal also showed significant difference.

Figure 5.3 are bar graphs, each of which displays the mean and standard deviation measurements of one PK parameter for normal pancreas (NP), PDAC, non-tumor (NT), and CP. The significant tests between NP vs PDAC, NP vs CP, and PDAC vs CP are labeled on top of the bars. F_p, v_p, K^{trans}, and v_e showed significant difference between PDAC vs CP (P=0.001, 0.009, <0.001, 0.014, respectively); F_p, v_p, and v_e showed significant difference between NP vs CP (P<0.001, 0.003, <0.001, respectively); F_p, K^{trans}, and v_e showed significant difference between NP vs PDAC (P<0.001, <0.001, <0.001,

respectively). The detailed *P* values for the significance test of the 6 pairs out of the 4 tissues types are listed in Table 5.1.

Table 5.1: P value of v_p, K^{trans}, v_e, and K_{ep} for each pair. * indicate statistical significance

P value	v_p	K^{trans}	v_e	K_{ep}
PDAC vs CP	**<0.001***	**<0.001***	**0.012***	**<0.001***
Normal vs PDAC	**0.011***	**<0.001***	**<0.001***	**<0.001***
Normal vs CP	**0.259**	**<0.001***	**<0.001***	**0.004***
Normal vs NT	0.920	<0.001*	<0.001*	0.003*
PDAC vs NT	0.002*	0.003*	<0.001*	0.004*
NT vs CP	0.193	0.365	0.119	0.184

5.4 Discussion

PDAC is among the most lethal malignancies with the macroscopic complete tumor resection at early stage as the only curative treatment. CP is a common pancreatic disease that causes irreversible damage to pancreas. The management of the two conditions differs greatly, so the accurate diagnosis and differentiation of CP and PDAC is of great significant in clinical practice, which, however, has been an unmet clinical need[153]. Both entities may appear with same clinical signs such as abdominal pain, weight loss, and pancreatic endocrine and exocrine dysfunction. They also share similar radiologic features including ductal abnormalities, mass lesions, and cystic lesions[154]. In recent year, DCE MRI with the potential to characterize vascular properties has been

gradually investigated in the differential diagnosis of PDAC versus CP. The preliminary results are promising. However, the application of DCE MRI in this field is still limited due to the difficulties to resolve respiratory motion and to realize adequate coverage and sufficient spatiotemporal resolution simultaneously

In this work, the 6D Multitasking DCE technique developed in our previous work was applied to explore the vascular properties of CP and PDAC. This technique enables free-breathing acquisition, whole-abdominal coverage, high DCE temporal resolution of 1 s, and dynamic T1 mapping, which offers the opportunity to capture the CA dynamics carrying the vascular information. Previous studies have demonstrated that this technique is feasible to estimate the vascular properties in vivo and characterize PDAC. In this work, the PK parameters can differentiate normal pancreas, PDAC, non-tumor tissue in PDAC patients, and CP.

Tofts model or extended Tofts model were the most-widely applied models in abdominal DCE MRI. Previous studies have shown that K^{trans} and v_e from Tofts model correlated with the MVD and fibrosis in PDAC lesions, respectively, and therefore can be used as imaging markers of the vascular properties of tumor. K^{trans} is an association of blood flow (BF) and permeability-surface area product (PS). To separately and accurately estimate BF and PS requires on the temporal resolution, which is impractical in most of the existing abdominal DCE works. In this work, 2CXM, which has the ability to estimate BF and PS, was implemented thanks to the temporal resolution accomplished by Multitasking DCE. Results indicated that PDAC and CP showed reduced blood flow compared to normal pancreas in this study, agreed with the pathological features of the two entities. F_p, v_p, and K^{trans} didn't show statistically significant difference between non-

tumoral regions in PDAC group and CP group. One possible reason is that the non-tumoral areas in PDAC cases are commonly associated with chronic obstructed pancreatitis due to the obstruction of pancreatic duct, which shares similar vascular properties compared to CP.

There are several limitations in this pilot study. First, all the data of PDAC were from patients who were undergoing chemotherapy. The properties of the microenvironment might have changed during the treatment, which limits the ability of the PK parameters to represent the original vascular properties of PDAC. Second, pathological/ histological reference of the tissue properties (such as MVD and fibrosis) for the patient cohorts were not available. In addition, the sample size for each group were relatively small. With the encouraging preliminary results, future studies will be performed on untreated patient cohort with histological validation.

5.5 Conclusion

The 6D Multitasking DCE technique, which enables free-breathing and respiratory motion-resolved image acquisition, entire-abdominal coverage, 1-s temporal resolution, and dynamic T1 quantification, were applied on 8 CP subjects. The PK parameters representing blood flow and vascular properties using 2CXM showed significant difference between normal pancreas, PDAC, and CP.

CHPATER 6: QUANTITATIVE LOW-DOSE MULTITASKING DCE (LD-MT-DCE) FOR BREAST CANCER

6.1 Introduction

Breast cancer is the most common malignant disease occurring in women worldwide with a lifetime risk of 12.4%[11]. Early diagnosis and effective selection of treatment is the key factor to increase the survival rate in the long term[158]. In recent years, DCE MRI has been widely applied in high-risk-population screening, detection, and therapy evaluation of breast cancer[11]. Studies have shown that DCE MRI has the highest sensitivity among all the imaging modalities in the diagnosis of breast tumor in current clinical practice[10-13]. A major limitation of the standard DCE MRI protocol is that the relatively poor temporal resolution, which is usually 60 to 120 seconds per volume acquisition traded for large coverage and high spatial resolution (typically at least 1 mm × 1 mm × 3 mm), can severely obscure the fast-changing PK information and limit its ability to assess physiological and functional features of tissues, such as blood flow (BF), MVD, and vascular permeability[3-5].

Recently, quantitative DCE MRI techniques capable of capturing and assessing the enhancement patterns and vascular properties of tissues have been developed and investigated for breast cancer. Previous studies suggested that K^{trans} is positively correlated with histopathological markers including MVD[26] and vascular permeability[27]. Some investigations have shown that K^{trans} can differentiate malignant and benign breast tumor[3,68,159,160]. Studies using DCE MRI to monitor therapy have reported that the

changes in BF, K^{trans}, and v_e can indicate the response status at early course of the treatment[5,31].

Despite these encouraging findings, quantitative DCE MRI of breast cancer continues to face demanding technical challenges. First, direct sampling conflicts make it hard to simultaneously achieve entire-breast coverage, high spatial resolution around 1 mm^3, and sufficient temporal resolution. As a result, current quantitative DCE methods make compromises on at least one of these goals. Second, the approximation in the quantification of CA concentration due to difficulties for direct dynamic T1 mapping can introduce extra error[36,37,69,161,162]. An additional issue with DCE MRI is the growing concern regarding Gd deposition in the brain and other body parts in patients with normal renal function[41-43], as described in Section 1.4. Imaging techniques which can reducing Gd dose without losing diagnostic accuracy would improve the risk–benefit ratio, alleviating concerns while still offering the crucial clinical information provided by DCE MRI images.

To address the above limitations and concerns, we developed a low-dose Multitasking DCE (LD-MT-DCE) technique for breast imaging based on Chapter 3&4. LD-MT-DCE performs 5-dimensional (5D) quantitative imaging with three spatial dimensions, a saturation recovery (SR) time dimension, and a DCE time dimension. It produces co-registered high-spatial-resolution (0.9 mm × 0.9 mm × 1.14 mm) dynamic T1 maps at 1.4-second temporal resolution with whole-breast coverage in one 10-min continuous scan, allowing quantification of CA concentration and PK parameters. The ultrahigh temporal resolution enables to capture the best contrast between tumor and normal tissues, which potentially allow for reduced dose. A GBCA dose of 0.02 mmol/kg was selected according

to a simulation evaluating the performance of the kinetic parametric estimation with different dosage. The two-compartment exchange model (2CXM) were used in this work to estimate tumor blood flow and vascular properties altogether[5,20,21]. The in vivo feasibility of LD-MT-DCE were then evaluated on healthy volunteers and patients with triple-negative breast cancer (TNBC).

6.2 Methods

6.2.1 Sequence design

Similar as described in Section 3.2.1, a continuous-acquisition pulse sequence with 3D segmented FLASH readouts in between periodic non-selective SR preparations was used to generate T1 contrast at multiple SR times for dynamic T1 quantification. Fat signal was suppressed by using water-only excitation for FLASH readouts.

Axial Cartesian readouts were collected using Gaussian random ordering in both phase and partition encoding directions. In addition, a projection line in the anterior-posterior direction (kx = ky = 0) was collected every 8th readout as training data.

6.2.2 Image reconstruction

In this work, the target LD-MT-DCE image possesses five dimensions with three spatial dimensions (x, y, z), and two time dimensions (SR time τ and DCE time course t), which can be formed as a three-way tensor $\mathcal{A}$ with voxel location index $\mathbf{x} = [x\ y\ z]^T$, τ, and t:

$$\mathbf{A}_{(1)} = \mathbf{U}\mathbf{G}_{(1)}(\mathbf{W}\otimes\mathbf{V})^T, \tag{6.1}$$

where the columns of $\mathbf{U}$, $\mathbf{V}$, and $\mathbf{W}$ contain the basis functions for spatial, SR, and DCE time dimensions. The reconstruction of $\mathcal{A}$ was explicitly decomposed into the recovering of each factor matrix, as described in Section 3.2.3[79-82].

The first step was to determine the SR basis function in $\mathbf{V}$ from a pre-generated dictionary of SR curves with 101 T1 values logarithmically spaced from 100 ms to 3000 ms, 17 flip angles from 1° to 9° in half-degree increments centered at 5°, and 21 saturation pulse angles linearly spaced from 60° to 120° were comprised in the dictionary. The SR factor $\mathbf{V}$ was then defined from the singular value decomposition (SVD) of the dictionary.

The second step was to estimate the core tensor $\mathcal{G}$ and DCE factor $\mathbf{W}$ from the completed training data $\widehat{\mathcal{D}}_{\mathrm{tr}}$ using the following equation:

$$\widehat{\mathcal{D}}_{\mathrm{tr}} = \arg \min_{\mathbf{D}_{\mathrm{tr},(2)} \in \mathrm{range}(\mathbf{V})} \|\mathbf{d}_{\mathrm{tr}} - \Omega_{\mathrm{tr}}(\mathcal{D}_{\mathrm{tr}})\|_2^2 + \lambda \left(\left\|\mathbf{D}_{\mathrm{tr},(1)}\right\|_* + \left\|\mathbf{D}_{\mathrm{tr},(3)}\right\|_* \right) + R(\mathcal{D}_{\mathrm{tr}}) \qquad (6.2)$$

The abrupt motion removal scheme as described in Section 3.2.5 was also applied to minimal any abrupt bulk motion. $R(\cdot)$ is an optional additional regularization functional, which employed temporal total variation (TV) along DCE dimension $R(\mathcal{D}_{\mathrm{tr}}) = \lambda_2 \left\|\boldsymbol{\nabla}\mathbf{D}_{\mathrm{tr},(3)}\right\|_1$ with finite-difference operator $\boldsymbol{\nabla}$ in this work. Subsequently, $\mathcal{G}$ and $\mathbf{W}$ can be extracted by applying higher-order SVD (HOSVD) to the completed $\widehat{\mathcal{D}}_{\mathrm{tr}}$, till where the temporal factor $\boldsymbol{\Phi} = \mathbf{G}_{(1)}(\mathbf{W} \otimes \mathbf{V})^T$ was determined.

The third step was to determine the spatial factor $\mathbf{U}$ with the acquired data $\mathbf{d}$ and the obtained tamporal factor $\boldsymbol{\Phi}$ by solving the optimization problem:

$$\widehat{\mathbf{U}} = \arg \min_{\mathbf{U}} \|\mathbf{d} - \Omega(\mathbf{FSU}\boldsymbol{\Phi})\|_2^2 + R(\mathbf{U}) \qquad (6.3)$$

The final result of the reconstruction produces the 5D image with full SR recovery curves for every DCE phase.

6.2.3 Motion compensation

In some cases, the position of the subjects may change during the 10-min scan. To reduce the consequent artifacts and mis-registration, a translational motion registration was applied to the k-space data. For the dataset with visible position changes, a single-time-dimension images, as described in Section 4.2.2.1 were first generated to estimate the translational parameters. The images over all elapsed time points were divided into N (usually $N = 2$ or 3) motion states based on positions. A template image of each state was obtained by averaging the single-time-dimension images within this state. The template image of the motion state which was assigned most of time points was chosen to be the reference, denoted as $\mathbf{a}_{\mathrm{ref}}$; the template images from the other states are denoted as $\mathbf{a}_i$, $i \in 1,2,\cdots,N-1$. The translation vector b_i between the moving state i and the reference was estimated as

$$\widehat{b_i} = \arg\max_{b_i} Mt\left(\mathbf{F}^{-1}\left(\mathbf{P}(b_i) \circ (\mathbf{F}\mathbf{a}_i)\right), \mathbf{a}_{\mathrm{ref}}\right), \tag{6.4}$$

with spatial Fourier transform $\mathbf{F}$, linear phase modulator $\mathbf{P}(b_i)$ (the k-space operation equivalent to image-domain translation), and mutual information metric $Mt(\cdot,\cdot)$. The k-space data was then directly compensated by applying $\mathbf{P}(b_i)$ to all k-space lines corresponding to the ith motion state[161].

6.2.4 PK modeling

As described in Section 3.2.4, The signal intensity of at a certain DCE time t and certain SR time $\tau = nT_{\mathrm{R}}$ can be expressed as:

$$s\big(A,\alpha,B,n,R_1(t)\big) = A\frac{1-e^{-T_{\mathrm{R}}\cdot R_1(t)}}{1-e^{-T_{\mathrm{R}}\cdot R_1(t)}\cos\alpha}\Big[1+(B-1)\big(e^{-T_{\mathrm{R}}\cdot R_1(t)}\cos\alpha\big)^n\Big]\sin\alpha, \quad (6.5)$$

with $R_1(t) = 1/T_1(t)$, amplitude A, SR pulse efficiency B, FLASH readout interval T_{R}, and flip angle α. The signal intensity vector $\mathbf{s}$ for an entire SR period with $n = 1, 2, \cdots, N$ at DCE time t is:

$$\mathbf{s}\big(A,\alpha,B,R_1(t)\big) = \big[s\big(A,\alpha,B,1,R_1(t)\big),\cdots,s\big(A,\alpha,B,N,R_1(t)\big)\big]^{\boldsymbol{T}}, \quad (6.6)$$

and the signal intensity matrix $\mathbf{S}$ over all DCE time bins $t = 0, 1, \cdots, T$ ($t = 0$ represents pre-contrast DCE phase) is:

$$\mathbf{S}(A,\alpha,B,\mathbf{r_1}) = \big[\boldsymbol{s}\big(A,\alpha,B,R_1(0)\big),\cdots,\boldsymbol{s}\big(A,\alpha,B,R_1(T)\big)\big], \quad (6.7)$$

where $\mathbf{r_1} = [R_1(0), R_1(1), \cdots, R_1(T)]^{\boldsymbol{T}}$ is the vector dynamic R_1 values over all DCE time bins. The dynamic CA concentration for tissues of interest C_{t} can be quantified based on the relaxivity accordingly:

$$C_{\mathrm{t}}(t) = \frac{R_1(t) - R_1(0)}{\gamma} \quad (6.8)$$

Following the derivation of CA concentration, the 2CXM was applied to describe the tracer activities within the tissue and estimate the vascular properties including plasma flow (F_{p}), plasma volume v_{p}, transfer constant K^{trans}, and EES volume faction v_{e}. As introduced in Section 2.3.4, the time-domain solution for 2CXM is[5,20,21]:

$$C_{\mathrm{t}}(t) = F_{\mathrm{p}}\cdot C_{\mathrm{p}}(t) * \big(Me^{-\alpha t} + (1-M)e^{-\beta t}\big) \quad (6.9)$$

$C_{\mathrm{p}}(t)$ is the AIF derived from the CA concentration in blood $C_{\mathrm{b}}(t)$ considering hematocrit: $C_{\mathrm{p}}(t) = C_{\mathrm{b}}(t)/(1-\mathrm{Hct})$. In this work, a population-based $\mathrm{Hct} = 0.4$ was employed. With fitted F_{p}, M, α, and β, other required kinetic parameters v_{p}, K^{trans}, and v_{e} can be calculated using following equation:

$$v_{\mathrm{p}} = \frac{F_{\mathrm{p}}}{M\alpha + (1-M)\beta},\ K^{\mathrm{trans}} = F_{\mathrm{p}}\frac{M(1-M)(\alpha-\beta)^2}{M\alpha^2 + (1-M)\beta^2},\ v_e = v_{\mathrm{p}}\frac{M(1-M)(\alpha-\beta)^2}{\alpha\beta} \quad (6.10)$$

6.2.5 Simulations

A numerical simulation was carried out in MATLAB (R2018a, Mathworks, MA, USA) to evaluate the performance of Multitasking DCE at different CA dosage from 0.01mmol/kg to 0.1 mmol/kg at a 0.01mmol/kg increment. A realistic AIF for the standard dose (0.1mmol/kg) was first generated using a traditional biexponential function[107] at 0.1-second temporal resolution. The AIF for other doses were then created proportionally. The CA concentration curves for breast tumor and normal breast tissue are generated according to Equation (6.9) and (6.10) using the following parameters: 1) for tumor, $F_{\mathrm{p}} = 1$ ml/min/g, $v_{\mathrm{p}} = 0.2$, $K^{\mathrm{trans}} = 0.08$ min^{-1} , $v_{\mathrm{e}} = 0.2$; 2) for normal breast tissue, $F_{\mathrm{p}} = 0.1$ ml/min/g, $v_{\mathrm{p}} = 0.05$, $K^{\mathrm{trans}} = 0.03$ min^{-1}, $v_{\mathrm{e}} = 0.4$. The dynamic R1 curves for each tissue type at different dose level can be produced using Equation (6.8) with a baseline T1 of 1900 ms, 1400 ms, 1400 ms for blood, tumor, and normal breast tissue.

Subsequently, the 5D Multitasking DCE image was simulated based on Equation (6.7) containing blood, tumor, and normal breast tissue using the undersampled dynamic R1 curves at a temporal resolution of 1.4 seconds. Random Gaussian noise were added to the 3D volume at each time point at two different signal-to-noise ratios (SNRs) of 20 and 40. The SNR was defined as the mean signal intensity of tumor using 0.1 mmol/kg dose over the standard deviation of the noise. Pixelwise dynamic T1 mapping were then conducted and kinetic parameters were estimated for tumor and normal blood tissue. For the image with each dose at each SNR level, the numerical experiment was repeated 20 times to assess the variation of the estimation.

6.2.6 Imaging experiments

6.2.6.1 Imaging protocol

All studies were carried out on a 3T MR scanner (VIDA, Siemens Medical Solutions, Erlangen, Germany), positioned prone and headfirst, using a 16-channel phase array bilateral breast coil for signal reception. In the imaging session, a standard clinical pre-contrast protocol was first performed, including multi-slice short-TI-inversion-recovery (STIR), multi-slice single-shot echo-planar imaging (SS-EPI) DWI, and 3D fat-suppressed T1W FLASH sequence. Following these sequences, the proposed LD-MT-DCE was applied. In the protocol, each SR period was designed to be 1400 ms with saturation times from 5.03 ms to 1388.3 ms at an increment of 5.03 ms for T1 quantification. The SR period was repeated 420 times, yielding a scan of 10 min. A low-dose GBCA (Gadavist, 0.02 mmol/kg, Bayer Schering Pharma) was diluted to 5 times of its original volume (which equals to the volume of a standard dose without dilution) and administrated intravenously 3 minutes into the scan using a power injector at a rate of 2 mL/s, followed by a 20 mL saline flush at the same rate. After the low-dose scan, clinical DCE images using the same 3D T1W FLASH sequence were acquired at 7 phases: 1 was acquired before an injection of a standard 0.1mmol/kg of Gadavist, and 6 were acquired continuously 12 second after this injection. All images in the session were acquired in axial orientation. Table 6.1 summarized the detailed imaging parameters for each sequence.

Table 6.1: List of imaging parameters

parameters	STIR	SS-EPI DWI	T1W GRE	LM-DCE
FOV (mm^2)	350 × 350	360 × 216	350 × 350	380 × 250
In-plane resolution (mm^2)	0.8 × 0.8	1.6 × 1.6	0.9 × 0.9	0.9 × 0.9
Slice thickness (mm)	4	5	1.14	1.14
Number of slices	40	38	192	152
Gap	0	0		/
TI (ms)	230	/	/	/
TR (ms)	4060	5800	3.59	5.00
TE (ms)	70	59	1.88	2.41
Average	2	1	1	1
Flip angle (◦)	80	180	10	5
b value (s/mm^2)	/	0/400/800	/	/
Acceleration factor	3	2	3	/

6.2.6.2 Volunteer study

The in vivo study was approved by the institutional review board and written informed consent was obtained for all participating subjects. Twenty healthy female subjects aged 22 to 78 years (mean age, 41 years) were recruited as control group. All subjects in the control group received the standard clinical pre-contrast protocol and LD-MT-DCE. Instead of the clinical DCE scan, half of the group (N = 10) received another LD-MT-DCE with the 0.02mmol/kg dose 30-minute apart from the first LD-MT-DCE scan in the same session to assess the repeatability of the LD-MT-DCE; the other half of the group (N = 10) received a standard-dose Multitasking DCE (SD-MT-DCE) 30-minute

apart from the first LD-MT-DCE scan to assess the ability in the quantitative evaluation of kinetic parameters of Multitasking DCE using low-dose or standard-dose.

6.2.6.3 Patient study

In addition to volunteer study, seven female patients aged from 28 to 66 (mean age, 48 years) with pathologically confirmed triple-negative breast cancer were recruited. Each patient received the imaging protocol described in Section 2.4.1. Histology reports from breast biopsy / surgery for each patient were also available as a proof of the lesions diagnosed in MRI images.

6.2.7 Image analysis

Image reconstruction and post processing were performed off-line in MATLAB (R2018a, Mathworks, MA, USA) for all Multitasking DCE data. Following image reconstruction, the pixelwise dynamic T1 was quantified from the reconstructed (τ, t)-space signal using *lsqnonlin* (non-linear least-square solver) and the pixelwise CA concentration curve was derived. The AIF was averaged over the inner area of left ventricle to minimize the effect of respiratory and cardiac motion. Subsequently, the maps for PK parameters F_{p}, v_{p}, K^{trans}, v_{e}, and the initial area under the CA concentration curve (iAUC) for the first 60 seconds (iAUC_{60}) and 120 seconds (iAUC_{120}) were obtained. The PK parameters reported for normal breast tissue in control group were the average over all the voxels of breast tissue throughout multiple slices excluding visible vessels and ducts.

The patient data were read by two radiologists (RS, with 32-year experience, and YG, with 10-year experience in the reading of Breast MRI) independently and the ROI of the tumors were drawn for all cases. For reading, LD-MT-DCE images were averaged to a temporal resolution at 84 seconds, close to the timing of clinical DCE images. Each radiologist reviewed the images from the two methods separately. For each set of image, a score was given to the overall image quality using a 5-point scale: 1-worst, anatomic details were impossible to identify, and there were extremely high noise and artifacts; 2-bad, anatomic details were difficultly identified, and there were significant noise and artifacts; 3-moderate, anatomic structures were visible but not clearly shown, and there were acceptable noise and artifacts; 4-good, the anatomic structures and details were visible and there were some noise and artifacts; 5-excellent, the anatomic structures and details were highly visible and there were no significant noise and artifacts. The location, size, type (focal-mass or non-mass), margin (smooth, spiculate, or lobulate), and perfusion type (persistent, plateau, or wash-out) were also measured separately on each set of images for each lesion. Then the radiologists compared the reports from the two methods and gave a score indicating if the findings on LD-MT-DCE were consistent with clinical DCE diagnosis using a three-point scale: 1- doesn't match, 2-partially match, and 3-match. The contrast-to-noise ratio (CNR) of the tumor versus surrounding parenchymal was evaluated for both imaging methods at the peak-enhanced phase on original DCE images and subtracted images using following equation:

$$CNR = \frac{\left|SI_t - SI_{pc}\right|}{\sigma_f}, \tag{6.11}$$

where SI_t is the signal intensity of tumor, SI_{pc} is the signal intensity of surrounding parenchymal, and σ_f is the standard deviation of the suppressed fat signal. For the PK

evaluation, the ROI for each lesion on LD-MT-DCE images was the average of the ROIs separately provided by the two radiologists. F_{p}, v_{p}, K^{trans}, v_{e}, iAUC$_{60}$, and iAUC$_{120}$ were estimated accordingly.

6.2.8 Statistical analysis

The repeatability of proposed technique was assessed on the repeat data from the 10 volunteers who were scanned twice with LD-MT-DCE. The Intra-class coefficient (ICC) and coefficient of variation (CoV) of F_{p}, v_{p}, K^{trans}, v_{e}, iAUC$_{60}$, and iAUC$_{120}$ were obtained. Linear regression was applied to assess correlation of LD- and SD-MT-DCE on the data from the other 10 volunteers who were scanned with LD-MT-DCE and SD-MT-DCE in the same imaging session and the regression coefficient were calculated for the six parameters.

The mean and standard deviation of the CNR for LD-MT-DCE and clinical DCE were measured and a paired t-test were applied to compare the CNR performance between the two methods. A one-way unbalanced analysis of variance (ANOVA) with Tukey test was performed to identify the significant difference of each PK parameter obtained between the following pairs: (1) malignant breast tumor and benign breast tumor in the patient group, (2) malignant breast tumor in the patient group and normal breast tissue in control group, and (3) benign breast tumor in the patient group and normal breast tissue in control group.

6.3 Results

6.3.1 Simulations

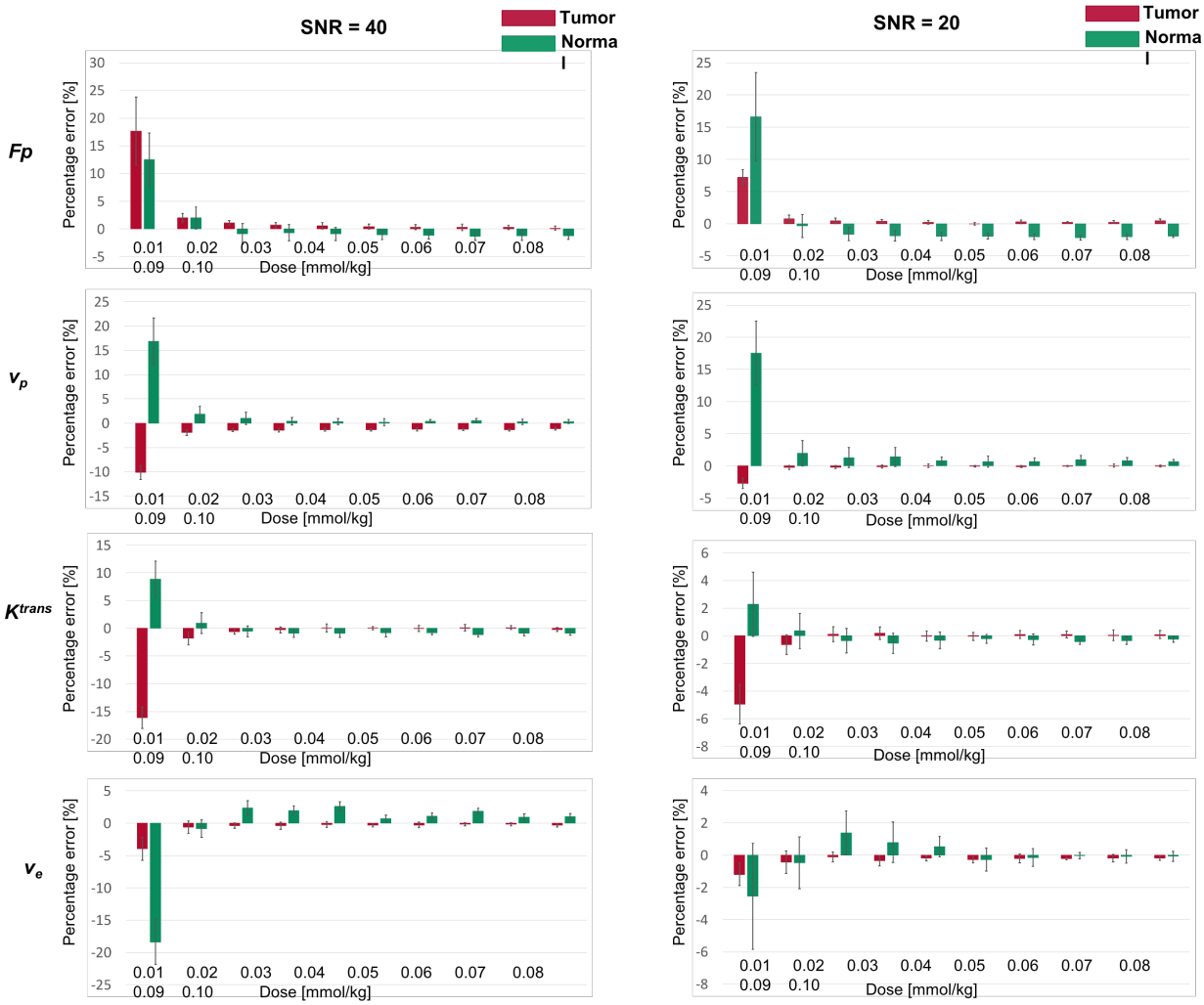


Figure 6.1: Simulations results. Each bar graph displays the mean relative error between the estimated parameter and the true parameter for GBCA dose from 0.01 mmol/kg to 0.1 mmol/kg at one SNR level. The error bars show the relative standard deviation of the 20 repetitions for each condition. For a dose equivalent or larger than 0.02 mmol/kg, the mean relative errors and relative standard deviations are within 2% for both tumor and normal tissue

The numerical data for blood, tumor, and normal breast tissue were generated using 10 different doses at 2 SNR levels. The PK parameters were fitted for each condition. The relative mean estimate error and relative standard deviation over the 20 repeated simulations for each parameter under each condition were displayed by the bar graphs with standard error bar (Figure 6.1). It is clearly demonstrated that for all parameters at both SNR levels, using a dose equal to or greater than 0.02 mmol/kg yields

an average estimation close to the true value (the percentage error is within 1%) with a narrow standard deviation within 1% for both tumor and normal tissue.

6.3.2 In vivo demonstration

The in vivo studies were performed on the 20 volunteers and 7 patients and all LD-MT-DCE data were reconstructed successfully. The 5D images contains 420 DCE phases at a temporal resolution of 1.4 seconds and each phase comprises 276 saturation times, yielding a total of 420□276=115,920 timepoints, each of which corresponds to a volumetric image. Figure 6.2 displays an example 5D LD-MT-DCE images in axial and sagittal orientations at three key DCE phases (pre-contrast phase, peak-enhanced phase $t \approx 80$ seconds, and late-enhancement phase $t \approx 480$ seconds) with two saturation times. Typical process of the transformation from LD-MT-DCE signal to dynamic CA concentration is demonstrated in Figure 6.3. Signal intensity curves expanded over all SR times and DCE phases representing blood, breast tumor, and normal breast tissue respectively are displayed in Figure 6.3 (A). The dynamic T1 for the three tissue types in Figure 6.3 (B) are directly quantified based on SR curves. The CA concentration curves are then calculated according to relaxivity, as shown in Figure 6.3 (C). The shape of the concentration curves for each tissue type is consistent with the findings shown in literatures. Figure 6.4 shows representative parametric maps of F_{p}, v_{p}, K^{trans}, v_{e}, iAUC_{60}, and iAUC_{120} from a healthy volunteer (A), a benign tumor of patient data (B), and a malignant tumor of patient data (C). The area marked by green solid boundary and red dashed boundary on the LD-MT-DCE image in Figure 6.4 (B) and (C) presents the benign and malignant breast tumors, respectively.

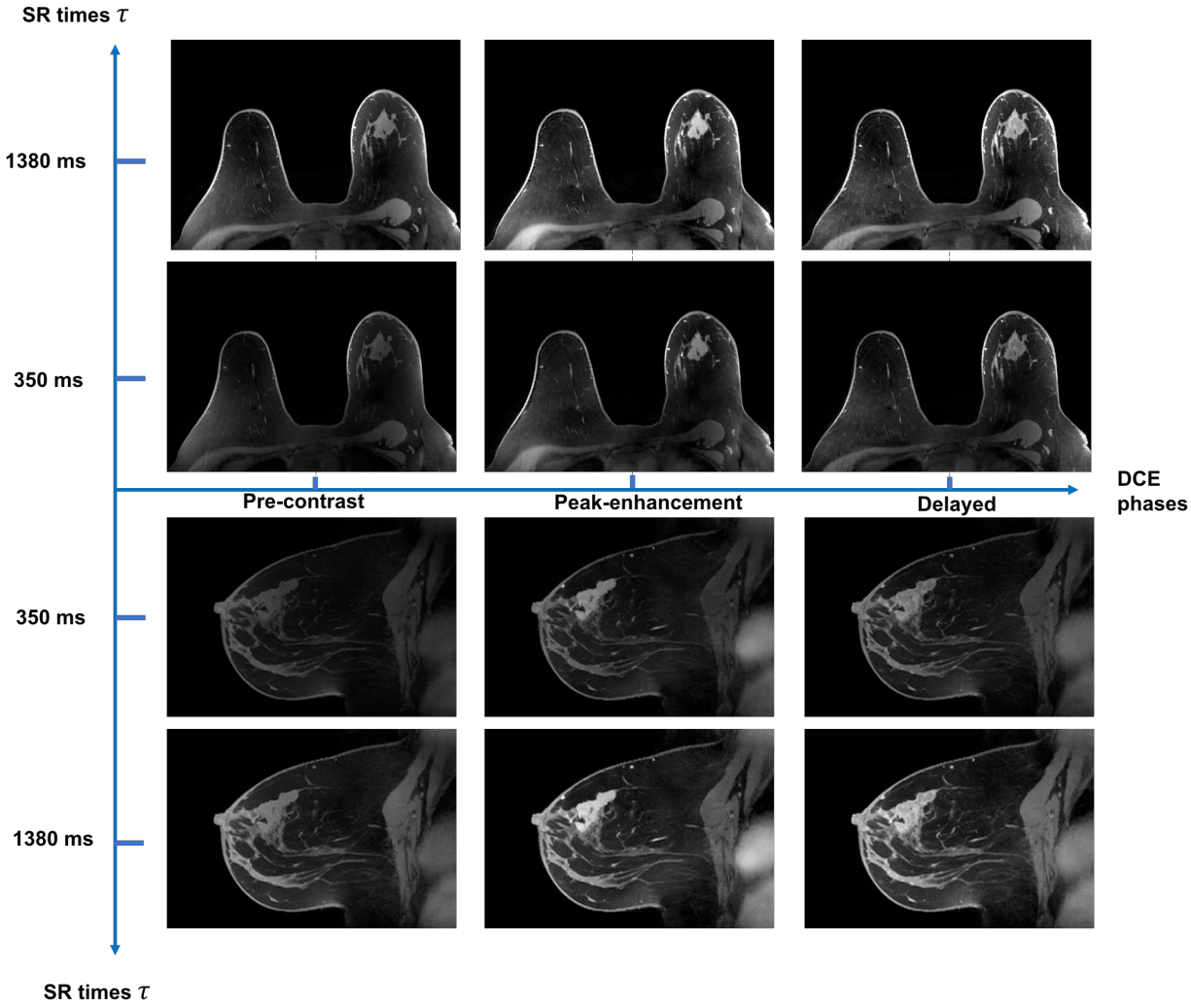


Figure 6.2: Representative 5D images of LD-MT-DCE from a 66-year-old patient. Images are displayed at pre-contrast phase, peak-enhancement phase (t = 40 s), and delayed phase (t = 5 min). For each DCE phase, images at two different saturation recovery times (τ = 350 ms and τ = 1380 ms) are shown in axial and sagittal views with clear tumor delineation. t is the time from injection

Figure 6.5 shows an example of motion compensation effect from a patient of 51 years old. The image from the peak-enhanced clinical DCE are displayed in Figure 6.5 (A) for tumor delineation. The patient had obvious movement during the scan of LD-MT-

DCE. Figure (B) displays the motion-corrupted frame and Figure 6.5 (C) displays corresponding image after motion compensation. The image quality parameters before motion removal is: SNR_{tumor}=13.4, $SNR_{nontumor}$ = 5.1, CNR = 8.3, sharpness = 1.45mm^{-1} (The signal intensity was normalized). After motion removal, the parameters are: SNR_{tumor} = 18.3, $SNR_{nontumor}$ = 7.4, CNR = 10.9, sharpness = 3.82mm^{-1}. The image is much clearner with less motion artifacts and all the parameters are substantially higher after motion compensation.

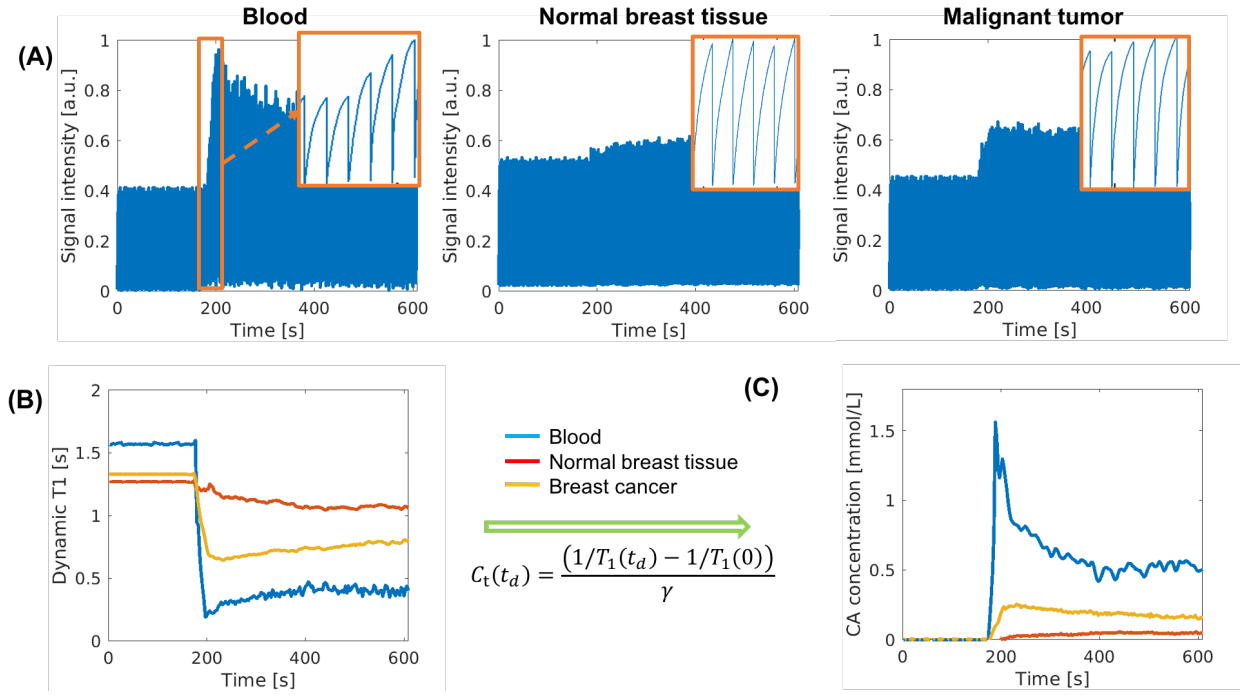


Figure 6.3: Transformation from signal intensity to CA concentration. (A) Representative signal profiles of blood, normal breast tissue, and malignant tumor. The zoom-in area shows the SR curves during the enhancement. (B) Dynamic T1 mapping based on SR periods. (C) Contrast agent concentration curves derived directly from the T1 mapping according to CA relaxivity

6.3.3 Volunteer study

The repeatability of F_p, v_p, K^{trans}, v_e, $iAUC_{60}$, and $iAUC_{120}$ for LD-MT-DCE are illustrated using regression (Figure 6.6). The regression coefficient R for the six

parameters were 0.99, 0.98, 0.99, 0.99, 0.97, and 0.97, respectively. The ICC were 0.99, 0.99, 0.99, 0.99, 0.98, and 0.99, respectively, and the CoV were 5.0%, 7.8%, 5.4%, 4.9%, 5.9%, 4.6%, respectively, as labeled on top of each regression plots.

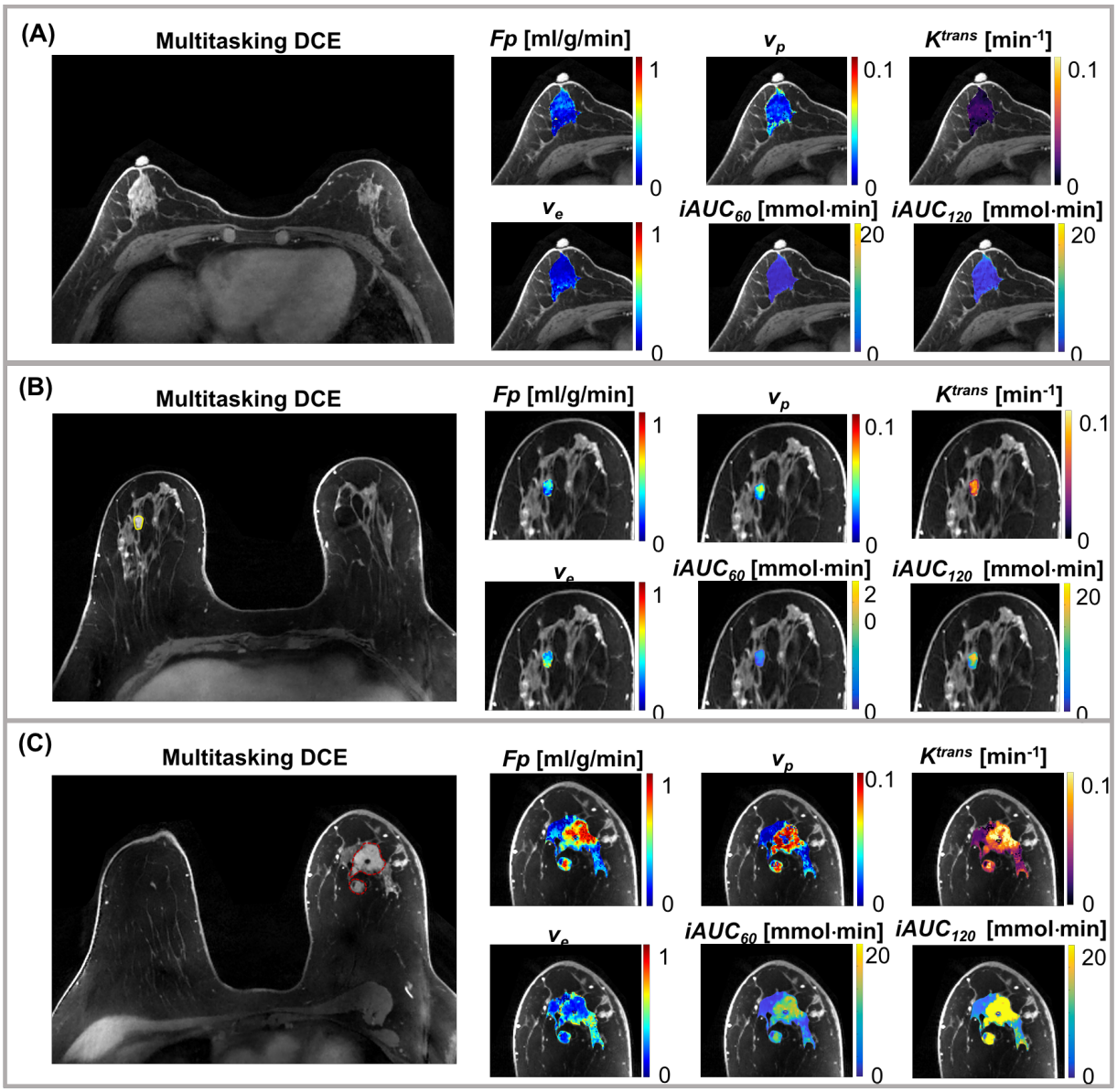


Figure 6.4: Representative maps of PK parameters showing normal breast tissue from a 52-year-old healthy volunteer (A), a benign tumor (marked by a yellow solid boundary) from a 49-year-old patient (B), and a malignant tumor (marked by a red dashed boundary) from a 65-year-old patient (C). The gray-scale images display peak-enhanced LD-MT-DCE images. The overlaid colormaps represents F_p, v_p, K^{trans}, v_e, $iAUC_{60}$, and $iAUC_{120}$, respectively. The malignant tumor has the highest F_p, v_p, K^{trans}, $iAUC_{60}$, and $iAUC_{120}$ values

Figure 6.7 demonstrates the correlation of the kinetic parameters estimated from LD-MT-DCE and SD-MT-DCE. The regression coefficient R for F_{p}, v_{p}, K^{trans}, v_{e}, iAUC$_{60}$, and iAUC$_{120}$ were 0.89, 0.85, 0.74, 0.91, 0.77, and 0.76, respectively. Among the six parameters, F_{p}, v_{p}, K^{trans}, and v_{e} are supposed to be dose-independent. The ICC for these four parameters were 0.93, 0.88, 0.84, and 0.94, respectively, and CoV were 11.4%, 21.5%, 10.3%, and 11.9%, respectively, indicating a good agreement between the parameters estimated using LD-MT-DCE and SD-MT-DCE.

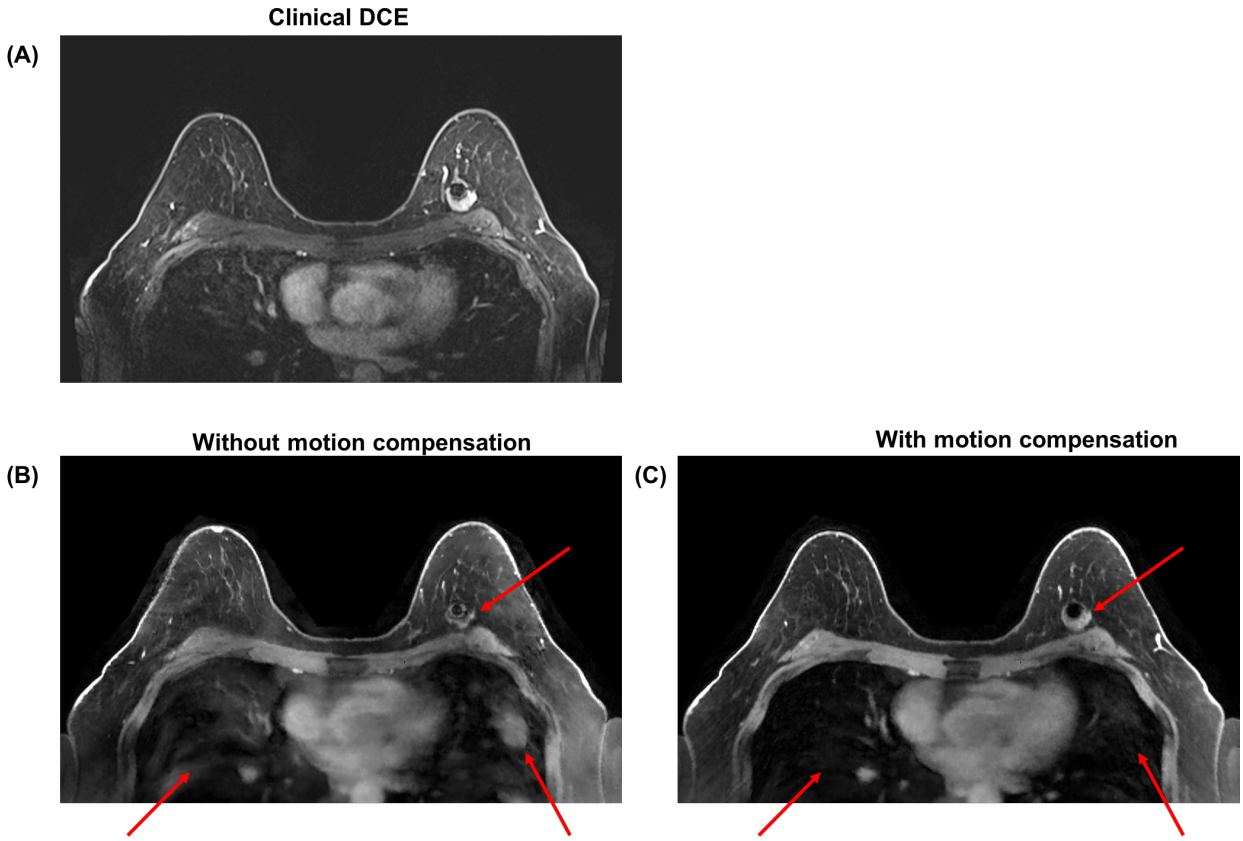


Figure 6.5: Motion compensation effect of a patient of 51 years old. (A) Peak-enhanced phase of clinical DCE. The tumor is labeled by the red dashed boundary, showing clear structure. (B) Motion-corrupted phase in LD-MT-DCE due to movement of the patient. Yellow arrows point out motion artifacts. The tumor structure is unclear. (C) The image after motion compensation. The motion artifacts are removed. The tumor has largely improved delineation.

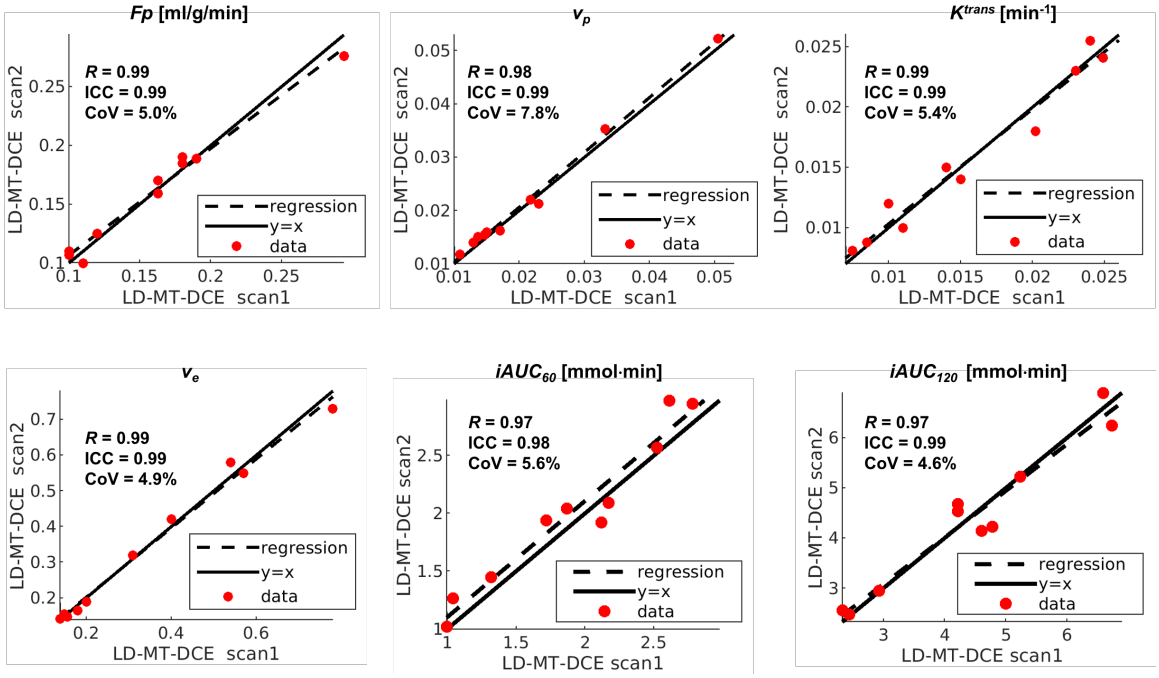


Figure 6.6: Repeatability evaluation for PK parameters on the repeat LD-MT-DCE data. The regression coefficients, ICC, and CoV between the estimation using the first and second LD-MT-DCE images were evaluated and displayed for all parameters.

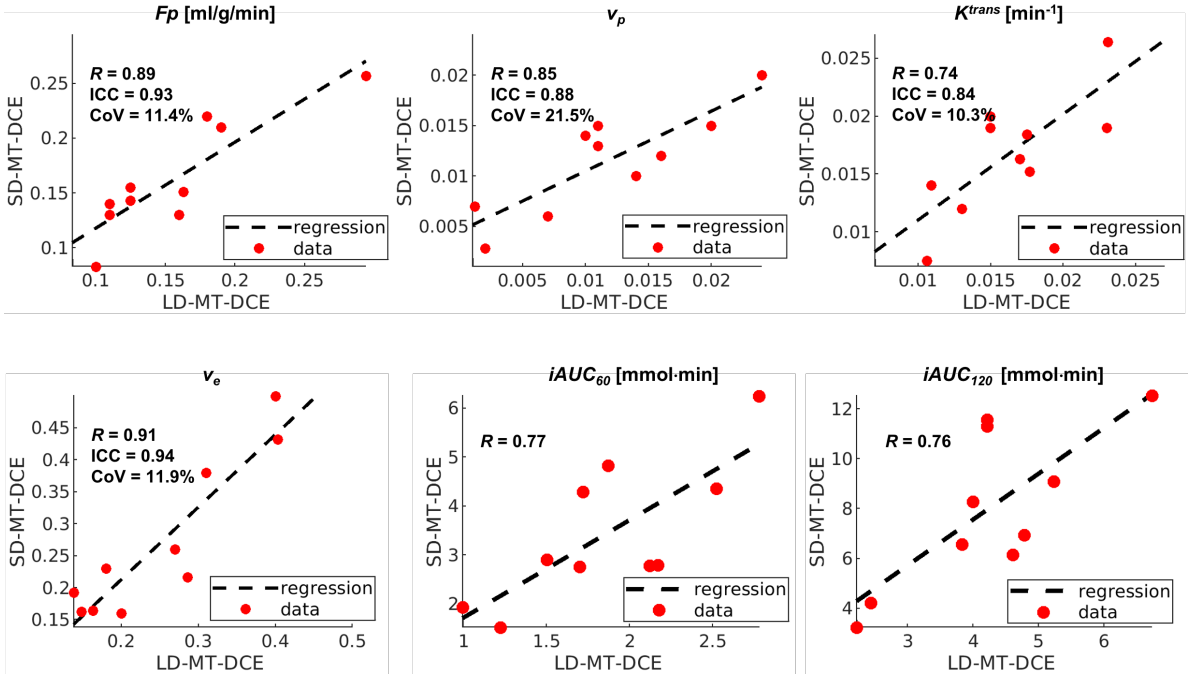


Figure 6.7: Correlation between the PK parameters estimated using LD-MT-DCE and SD-MT-DCE. The regression coefficients R, ICC, and CoV were evaluated for the dose-independent parameters F_p, v_p, K^{trans}, v_e. For dose-dependent parameters $iAUC_{60}$, and $iAUC_{120}$, R between LD- and SD-MT-DCE were assessed.

6.3.4 Patient study

The two radiologists provided their professional reading. The detailed size and properties of for each lesion are shown in Table 6.2 in the supplementary materials. According to the clinical reports, a total of 18 lesions were detected in the 7 patients and 14 of the lesions have been confirmed on breast biopsy / surgical pathology: 8 of the lesions are malignant and 6 are benign. The number of lesions and the average scores for image quality and consistency between LD-MT-DCE and clinical DCE provided by the two radiologists are listed in Table 6.3. The LD-MT-DCE images were scored as "excellent" for 5 cases and equal or above "good" for the other 2 cases by both radiologists. In 6 cases the lesions detected by LD-MT-DCE perfectly matched the findings on clinical DCE images.

Table 6.2: Comparison of the image quality and diagnosis results between LD-MT-DCE and clinical DCE. The number of malignant tumors and benign tumors were diagnosed on clinical DCE. The image quality of both methods are listed. The LD-MT-DCE images were scored as "excellent" for 5 cases and equal or above "good" for the other 2 cases by both radiologists. In 6 cases, the diagnosis results of LD-MT-DCE perfectly match the results of clinical DCE in terms of the location, size, type, margin, and perfusion type.

	Age	Number of malignant tumor	Number of benign tumor	Image quality (1-5)		Consistency (1-3)
				LD-MT-DCE	Clinical DCE	
Patient 1	66	1	1	**5**	4.5	**3**
Patient 2	58	1	1	**4.5**	4.5	**3**
Patient 3	35	1	2	**5**	5	**2.5**
Patient 4	49	2	0	**5**	5	**3**
Patient 5	28	1	1	**5**	5	**3**
Patient 6	51	1	1	**4**	5	**3**
Patient 7	50	1	0	**5**	5	**3**

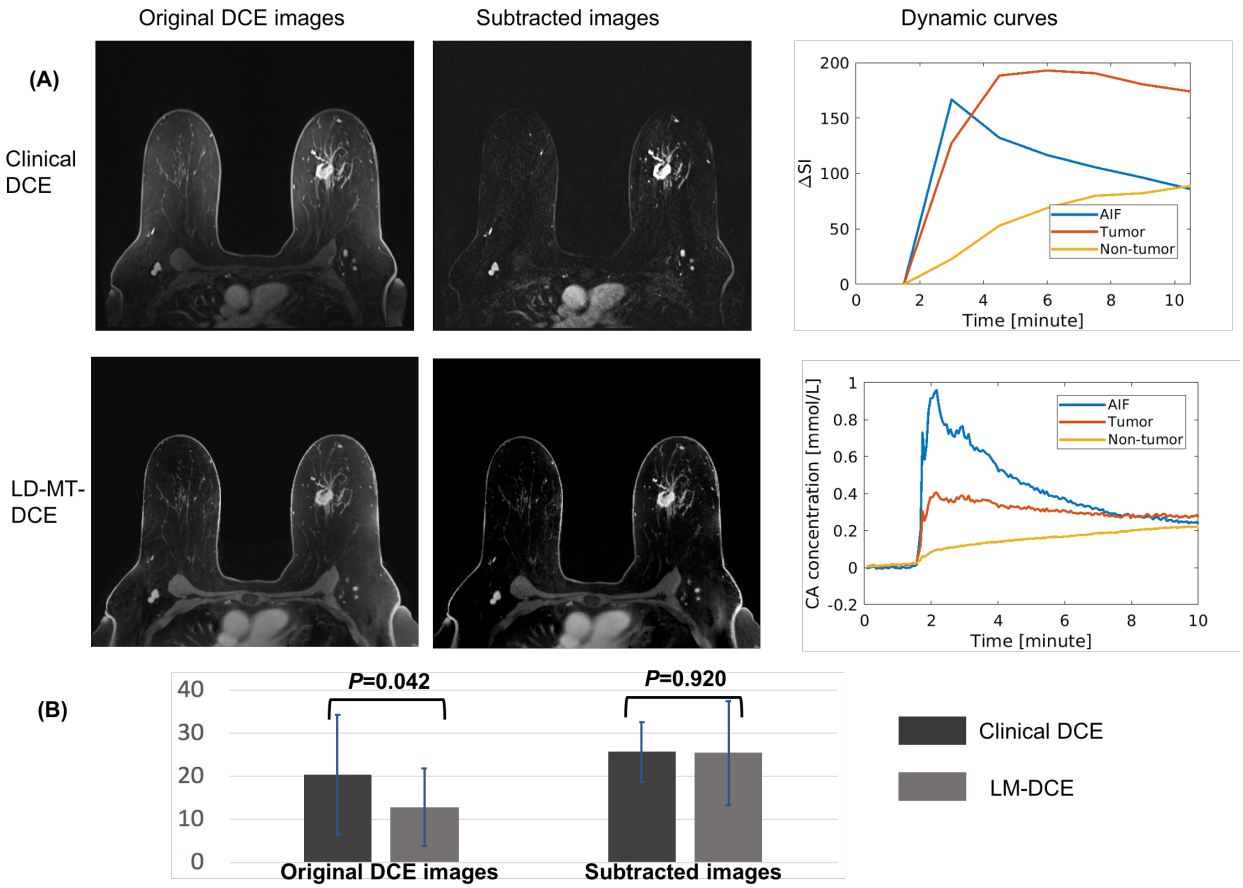


Figure 6.8: (A) Representative images from LD-MT-DCE and clinical DCE of a 58-year-old patient. The original DCE images display the images at peak-enhancement phase for both methods. The subtracted images are the original DCE images subtracting pre-contrast images. Dynamic curves from LD-MT-DCE and clinical DCE are displayed. With higher temporal resolution, LD-MT-DCE produces dynamic curves with more temporal details. (B) Bar graphs showing the CNR for original DCE images at peak-enhancement phase and subtracted images for all patients. The CNR of subtracted images shows no difference between LD-MT-DCE and clinical DCE.

Figure 6.8 (A) shows the comparison of LD-MT-DCE and clinical DCE. Figure 6.8 (A) is an example patient case including the original and subtracted peak-enhanced images, and the CA concentration curves for both imaging methods. The bar graphs in Figure 6.8 (B) compares the CNR of different imaging methods of original DCE images (LD-MT-DCE: 12.8±7.1; clinical DCE: 20.4±14.3) and subtracted images (LD-MT-DCE:

25.4±12.0; clinical DCE: 25.7±9.4) at the peak-enhanced phase. The paired t-test indicated that CNR on subtracted images has no significant difference using LD-MT-DCE compared to clinical DCE with standard dose.

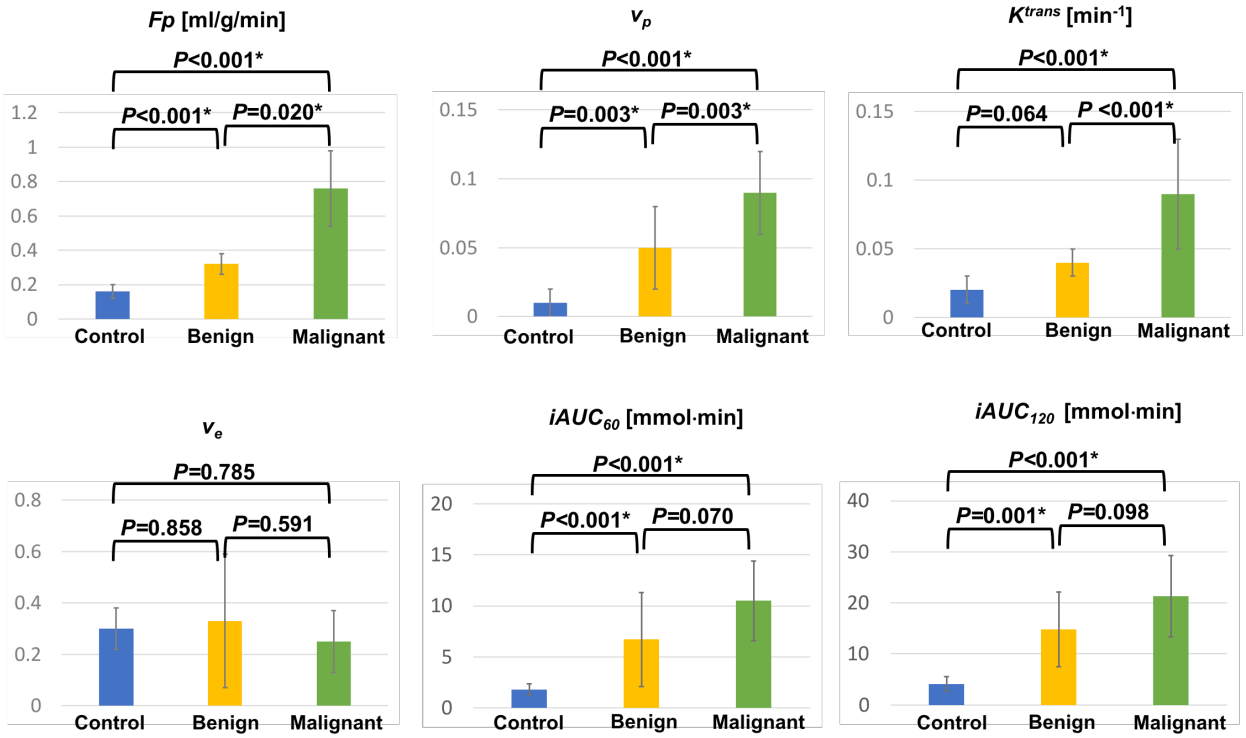


Figure 6.9: Bar graph showing the mean value and standard deviation of F_p, v_p, K^{trans}, v_e, $iAUC_{60}$, and $iAUC_{120}$ for control group, benign tumors and malignant tumors in patient group. The P values between each pair by one-way unbalanced ANOVA with Tukey test are marked on top of the bar graphs. F_p, v_p, K^{trans}, $iAUC_{60}$, and iAUC120 were significantly different between control breast tissue and malignant tumor; F_p, v_p, $iAUC_{60}$, and iAUC120 were significantly different between control and benign tumor; F_p, v_p, and K^{trans} were significantly different between malignant and benign tumor. * indicates statistically significant difference.

Figure 6.9 displays the mean and standard deviation measurements of F_{p}, v_{p}, K^{trans}, v_{e}, $iAUC_{60}$, and $iAUC_{120}$ from the control, malignant, and benign tumors. The Tukey test shows that F_{p}, v_{p}, K^{trans}, $iAUC_{60}$, and iAUC120 were significantly different between control breast tissue and malignant tumor (P <0.001, <0.001, <0.001, <0.001,

<0.001, respectively); F_{p}, v_{p}, iAUC$_{60}$, and iAUC120 were significantly different between control and benign tumor (*P* <0.001, 0.003, <0.001, 0.001, respectively); F_{p}, v_{p}, and K^{trans} were significantly different between malignant and benign tumor (*P* =0.020, 0.003, <0.001, respectively). Table 6.4 listed the detailed number of the statistical analyses.

Table 6.3: Detailed information about tumors detected in patient group.

			Location	Size (TX × AP × SI mm^3)	Margin	Type	Perfusion	BI-RADS
Patient 1	Lesion 1	Malignant	left	47.1 × 66.0 × 45.5	Lobulate	Focal mass	Wash-out	5
	Lesion 2	Benign	right	6.4 × 10.7 × 5.7	Lobulate	Focal mass	Persistent	3
Patient 2	Lesion 1	Malignant	left	20.4 × 21.6 × 17.1	Spiculate	Focal mass	Wash-out	5
	Lesion 2	Benign	right	3.0 × 8.8 × 5.1	Smooth	Focal mass	Persistent	2
Patient 3	Lesion 1	Malignant	left	14.8 × 17.6 × 14.3	Spiculate	Focal mass	Wash-out	5
	Lesion 2	Benign	left	3.2 × 3.7 × 4.3	Lobulate	Focal mass	Persistent	4
	Lesion 3	Benign	left	4.5 × 5.1 × 4.9	Spiculate	Focal mass	Wash-out	4
Patient 4	Lesion 1	Malignant	left	29.8 × 38.9 × 48.7	\	Regional	Wash-out	5
	Lesion 2	Malignant	right	8.3 × 13.2 × 12.5	Smooth	Focal mass	Wash-out	4
Patient 5	Lesion 1	Malignant	right	42.0 × 33.2 × 33.5	Spiculate	Focal mass	Wash-out	5
	Lesion 2	Benign	right	41. × 3.4 × 4.1	Smooth	Focal mass	Persistent	3
Patient 6	Lesion 1	Malignant	left	17.9 × 15.0 × 22.9	Spiculate	Focal mass	Wash-out	5
	Lesion 2	Benign	left	3.2 × 3.5 × 4.4	Lobulate	Focal mass	Persistent	3
Patient 7	Lesion 1	Malignant	right	30.4 × 31.0 × 33.1	Spiculate	Focal mass	Wash-out	5

Table 6.4: Detailed statistical results of F_p, v_p, K^{trans}, v_e, $iAUC_{60}$, and $iAUC_{120}$ for control group, benign tumors and malignant tumors in patient group. C: control; B: benign tumor; M: malignant tumor. * indicates statistically significant difference.

	Fp (ml/min/g)	v_p	K^{trans}	v_e	$iAUC_{60}$	$iAUC_{120}$
Control (n = 15)	0.16±0.04	0.01±0.01	0.02±0.01	0.30±0.08	1.80±0.58	4.12±1.42
Benign (N = 6)	0.32±0.06	0.05±0.03	0.04±0.01	0.33±0.26	6.72±4.59	14.86±7.31
Malignant (N = 8)	0.76±0.22	0.09±0.03	0.09±0.04	0.25±0.12	10.48±3.94	21.30±7.96
P (C vs M)	<0.001*	<0.001*	<0.001*	0.785	<0.001*	<0.001*
P (M vs B)	0.020*	0.003*	<0.001*	0.591	0.070	0.098
P (C vs B)	<0.001*	0.003*	0.064	0.858	<0.001*	0.001*

6.4 Discussions

In this study, we presented a novel 5D quantitative DCE technique based on MR Multitasking, which enables whole-breast coverage, high spatial resolution at $0.9\times0.9\times1.14$ mm^3, high temporal resolution at 1.4 s, and dynamic T1 mapping in a single 13-min scan using a GBCA dose of 0.02 mmol/kg. The results from the volunteer and patient studies demonstrated the feasibility of the proposed LD-MT-DCE technique in the characterization of breast tumor.

A major challenge that limits the adoption of quantitative DCE MRI techniques in the clinical practice of breast is the conflicts to achieve adequate coverage, spatial resolution and temporal resolution simultaneously. The American College of Radiology guidelines recommend to acquire clinical breast DCE MRI images using 3D scheme with

a slice thickness less than 3 mm and in-plane spatial resolution of 1 mm to minimize volume-averaging effect and possibility for missing small lesions[163], rendering a poor temporal sampling rate up to 4 minutes. However, sufficient temporal resolution is crucial to quantify the vascular properties. Previous investigations have shown that the a temporal resolution at least 10 seconds is necessary to depict tumor dynamic[35], and 1-3 seconds to capture the dynamics of AIF[76-78], both of which are key factors in the pharmacokinetic modeling[5]. To improve the temporal resolution, Brix et al. collected the dynamic T1W image at a 3.25 s temporal resolution with only two slices crossing the lesion and the aorta[164]; Abe et al. traded spatial resolution (1.5 mm × 1.5 mm × 3.0 mm) for temporal resolution (7 s) using an ultrafast DCE technique[3]; Georgiou et al. interleaved high-spatial/low-temporal resolution images with low-spatial/high-temporal resolution images[5]. However, the acquisition rate in some work are still suboptimal for pharmacokinetic modeling. Also, the important spatial distribution of the vascular properties could be obscured when the dynamic features used to estimate of kinetic parameters is mainly based on low-spatial-resolution images. The proposed LD-MT-DCE technique, on the other side, can truly acquire the images with adequate coverage, spatial resolution and temporal resolution at the same time, without the sacrifice of spatial or temporal depiction.

The CA concentration in the proposed technique is directly quantified from dynamic T1 mapping to avoid possible error introduced by linear approximation from T1W signal intensity or misregistration caused by separately acquired pre-contrast T1 maps. The feasibility of dynamic T1 fitting in Multitasking DCE has been assessed by numerical simulations, phantom validation, and in vivo study in our previous work[161,162].

The standard 0.1 mmol/kg dose of GBCA for DCE MRI was determined in the 1980s[39,40]. Due to the improved imaging technique and intensified concern towards gadolinium deposition in body, efforts seeking to reduce the dose while keeping the lesion conspicuity have been made[41,165,166]. In this work, the simulation results showed that with a dose equal to or greater than 0.02 mmol/kg, the percentage error between the true and estimate parameters and the standard deviation of the estimate parameter were within 2% in most cases. The estimate error was stable to the increase of dosage, indicating that a dose of 0.02 mmol/kg is the minimum effective dose to keep the accuracy / confidence of the parameter quantification. The in vivo studies suggested that LD-MT-DCE with only 20% percent of the standard dose produced excellent image quality comparable to standard clinical DCE. The ratio of CNR calculated from original images between LD-MT-DCE and clinical DCE is 0.63, much high than the ratio of the dose, which is 0.2. The similar CNR from subtracted images and consistent diagnosis results offered by two imaging methods suggested that LD-MT-DCE has the potential to be equivalent to standard clinical DCE in the detection of breast lesions, which is promising as a future approach in the management of breast cancer, especially for high-risk screening and multiple follow-ups.

The kinetic parameters estimated by LD-MT-DCE for normal breast tissue, malignant, and benign tumors are in the range of published results[5,167]. Among them, F_{p} and v_{p} were able to show significant difference between each pair of the three tissues: control, malignant, and benign tumor; K^{trans} is able to differentiate malignant tumors with benign tumors and control. There were only a few studies on blood flow in breast tumor using MRI due to the demanding sampling requirements. Makkat et al. reported a blood

flow at 0.84±0.46 ml/g/min for malignant tumor and 0.23±0.46 ml/g/min for benign tumor with significant difference[40]; Georgiou et al. reported 0.61±0.25 ml/g/min for malignant tumor[5]. Those results compared well with the values in our work, which is 0.76±0.22 ml/g/min for malignant tumor and 0.32±0.06 ml/g/min for benign tumor with significant difference (P<0.001). K^{trans} has been extensively applied in the characterization of breast tumor with a wide range on order of 0.01 to 1 min^{-1} due to different imaging technique and pharmacokinetic model adopted[159,160,168]. Investigations suggested that K^{trans} can differentiating malignant and benign breast tumor, which is agreed with the results in our work (P <0.001 between malignant and benign tumor). The volunteer study indicates F_{p}, v_{p}, K^{trans}, v_{e}, $iAUC_{60}$, and $iAUC_{120}$ estimated using LD-MT-DCE were in vivo repeatable with high ICC and small CoV values. The strong correlation between the parameters estimated by LD-MT-DCE and SD-MT-DCE demonstrated that Multitasking DCE technique using 20% dose has similar ability in the quantification of vascular properties compared with using standard dose. Although F_{p}, v_{p}, K^{trans}, v_{e} are supposed to be dose-independent, the water exchange and T2* effect can still affect the estimation of kinetic parameters to some extent, which may contributes to the differences of the parameters estimated by LD-MT-DCE and SD-MT-DCE.

A major limitation of this study is the small number and limited type of cases. All the seven patients included in the study had TNBC and the malignant tumors were mostly large and invasive. With the promising initial results, future studies should be conducted on a larger patient cohort with various subgroup analysis in terms of size, grade, or other pathological characteristics. Another limitation is that the repeatability of the estimate of kinetic parameters was not evaluated in patient group in this pilot study due to the need

for an extra contrast injection of standard dose clinical DCE. In addition, detailed pathological analysis, which is the gold standard for lesion definition, was not applicable. In the following-up studies, the accuracy of the LD-MT-DCE in the diagnosis of breast lesions should be validated with pathology and the repeatability on a larger population should be assessed.

6.5 Conclusion

A novel LD-MT-DCE technique was developed for breast imaging, enabling whole-breast coverage, high spatial resolution at 0.9□0.9□1.14 mm^3, high temporal resolution at 1.4 s, and dynamic T1 mapping in a single scan using a GBCA dose of 0.02 mmol/kg. It showed excellent image quality and equivalent diagnosis compared to standard-dose clinical DCE. The quantitative DCE parameters estimated by LD-MT-DCE were in vivo repeatable and significantly different between normal breast tissue, malignant, and benign tumors in TNBC patients.

CHAPTER 7: CONCLUSIONS AND FUTURE INNOVATIONS

DCE MRI plays a crucial role in the diagnosis, staging, and treatment monitoring of numerous pathological conditions. Besides morphological delineation, it also has the potential to capture functional information, such as blood flow, MVD, fibrosis, etc., by modeling the CA passage within the tissues. Those functional changes of tissues typically precede the morphological alteration, which provides a possible pathway for the early detection of diseases. However, the lack of well-agreed DCE MRI protocol to address the technical difficulties, including the sampling conflict for coverage and resolution, the requirement to handle physiological motion, and the need to accurately quantify CA concentration, have limited the application of DCE MRI to evaluate the functional properties of tissues in clinical practice.

To tackle these technical challenges, the presented dissertation developed a Multitasking DCE technique, which achieved respiratory motion-resolved acquisition and dynamic T1 mapping with adequate coverage, sufficient spatial resolution, and 1-second temporal resolution. The pilot clinical studies in carotid atherosclerosis, PDAC, and CP demonstrated that proposed technique is feasible to characterize the pathological tissues in multiple organs/ disease; in the study of patients with breast cancer, the proposed technique is demonstrated equivalent diagnosis using 20% of the standard dose compare to clinical DCE with standard dose, indicating the feasibility of Multitasking DCE to reduce the dose of GBCA.

7.1 Summary of the Work

7.1.1 Multitasking DCE in carotid atherosclerosis

DCE MRI has been used for quantitative assessment of the neovascular architecture and perfusion properties in carotid atherosclerosis. However, most existing techniques are incapable of fulfilling the technical requirements including submillimeter in-plane spatial resolution (0.5–0.7mm), adequate anatomical coverage, high temporal resolution, and accurate quantification of the CA concentration. We proposed the Multitasking DCE technique, which enables 3D coverage of entire carotid vasculature with high spatial resolution (0.7 mm isotropic), high temporal resolution (595 ms), and dynamic T1 mapping for direct quantification of CA concentration. Bulk motion detection and removal scheme were also implemented for the improvement of image quality. Phantom and in vivo studies have shown that the proposed technique can achieve accurate T1 quantification and robustness to motion. The PK parameters were repeatable in vivo and showed significant difference between carotid atherosclerosis and normal carotid vessel wall.

7.1.2 Multitasking DCE in abdomen

DCE MRI is the key protocol in the management of PDAC, a highly lethal malignancy with a 5-year survival rate at 8%. However, besides the common limitations, DCE MRI in abdomen is subject to respiratory motion, which can significantly degrade image quality and exaggerate the sampling challenges. We improved the Multitasking DCE technique to perform 6-dimensional (6D) quantitative imaging with three spatial dimensions, a saturation recovery dimension, a respiration dimension, and a DCE time dimension. It achieves respiratory-motion-resolved, high-temporal-resolution T1

quantification of the entire abdomen in a 10-min free-breathing scan. To our knowledge, this is the first abdominal DCE MRI method that simultaneously allows for 3D true free-breathing acquisition, 1-s temporal resolution, and dynamic T1 mapping. Sixteen healthy volunteers and 14 patients with pathologically confirmed PDAC were recruited for the in vivo study. The results demonstrated that the quantitative PK parameters using Multitasking DCE were repeatable in vivo and showed significant differences between normal pancreas, tumor and non-tumoral regions in PDAC patients.

In addition, to explore the ability of the 6D Multitasking DCE to distinguish PDAC versus CP, 8 patients with confirmed CP were recruited. The 2CXM model was applied to estimate blood flow and vascular properties simultaneously. The PK parameters representing blood flow and vascular properties showed significant difference between normal pancreas, PDAC, and CP.

7.1.3 Multitasking DCE in breast with low-dose

DCE MRI has the highest sensitivity in the diagnosis of breast cancer among all imaging modalities. However, due to the high requirement on the spatial resolution to capture small lesions, the temporal resolution of clinical DCE protocols is typically compromised at 60 to 120 seconds, which significantly limits its ability for the functional evaluation. The concern for GBCA deposition also restricts its application in the screening for high-risk population. To address the limitations, we developed a low-dose Multitasking DCE (LD-MT-DCE) technique for breast imaging, which provides co-registered high-spatial-resolution (0.9 mm × 0.9 mm × 1.14 mm) dynamic T1 maps at 1.4-second temporal resolution with whole-breast coverage in one 10-min continuous scan, allowing

quantification of CA concentration and PK parameters. The dose was chosen to be 0.02 mmol/kg, 20% of the standard dose, based on a numerical simulation conducted to evaluate the dose effect on the accuracy and precision of the PK parameters quantified using LD-MT-DCE. Twenty healthy volunteers and 7 patients with TNBC were recruited for the in vivo study. The results demonstrated that LD-MT-DCE possessed excellent image quality and equivalent diagnosis compared to standard-dose clinical DCE. The quantitative PK parameters estimated by LD-MT-DCE were in vivo repeatable and significantly different between normal breast tissue, malignant, and benign tumors in TNBC patients.

7.2 Future Work

7.2.1 Accelerating image reconstruction

The relatively long reconstruction time is a major limitation for the wide clinical application of Multitasking DCE. The bottleneck is to iteratively resolve spatial factor using Equation 2.29. One possible solution is to incorporate deep learning network into the reconstruction procedure. Previous works have shown that directly recovering images from undersampled k-space data using deep learning network is feasible[169,170]. In Multitasking framework, deep learning can accelerate the recovery of spatial factor matrix and thus highly speed up the reconstruction procedure.

7.2.2 Application of LD-MT-DCE to a variety of pathological conditions

LD-MT-DCE has been demonstrated feasible in the characterization of breast cancer. It is promising to greatly alleviate the concern towards GBCA deposition and DCE

MRI if this technique can provide same diagnosis power compared to conventional techniques with only 20% dose in more pathological conditions.

A preliminary study using 6D Multitasking DCE with a GBCA dose of 0.02 mmol/kg to characterize pancreas has been performed on 10 healthy volunteers. The repeatability of the PK parameters estimated from repeated 6D LD-MT-DCE scans and the correlation of the PK estimation between 6D LD-MT-DCE and 6D SD-MT-DCE are illustrated in Figure 7.1 and Figure 7.2

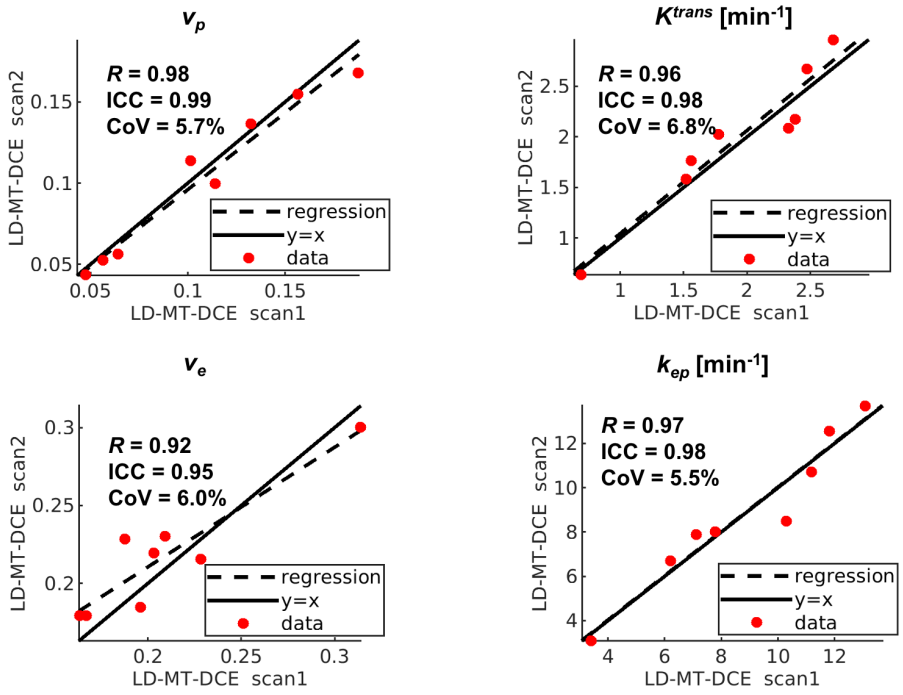


Figure 7.1: Repeatability evaluation for PK parameters on the repeat LD-MT-DCE data in pancreas. The regression coefficients, ICC, and CoV between the estimation using the first and second LD-MT-DCE images were evaluated and displayed for all parameters.

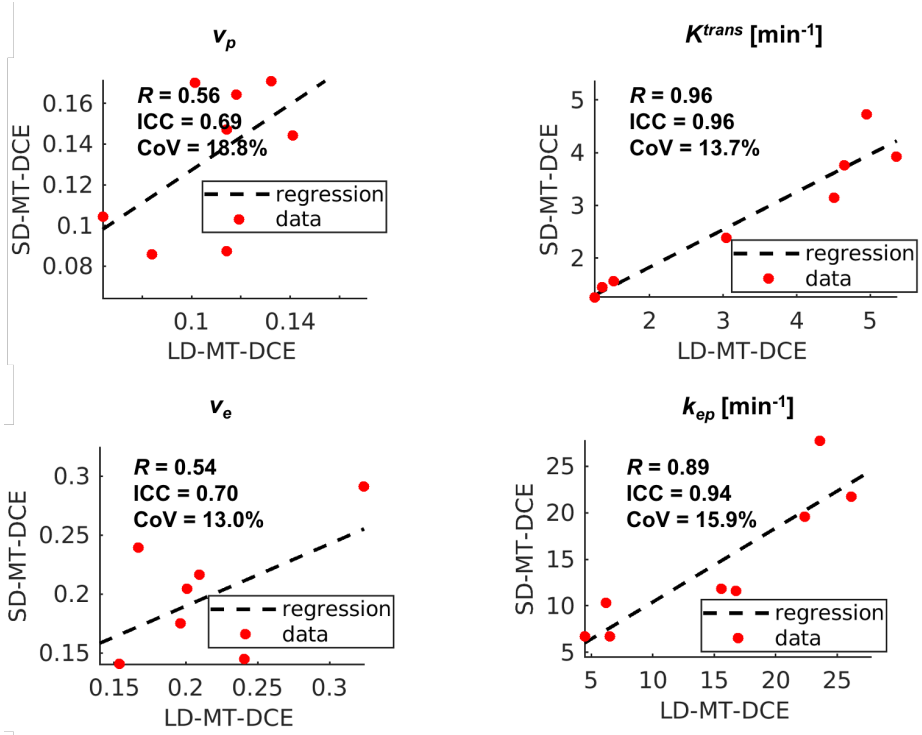


Figure 7.2: Correlation between the PK parameters estimated using LD-MT-DCE and SD-MT-DCE. The regression coefficients, ICC, and CoV were evaluated and displayed for all parameters.

7.2.3 Animal studies with histological validation

Future studies will include to perform Multitasking DCE technique on a larger patient cohort with the histological validation. Previously in various applications, correlations were reported between the PK parameters and histological markers, including the inflammatory markers, MVD, and fibrosis. However, the estimation of the PK parameters can be affected by technique, protocol, etc. With the ability of Multitasking DCE to achieve dynamic high-spatiotemporal-resolution T1 quantification, it is important to develop the correlation between the PK parameters from Multitasking DCE and the histological biomarkers. Animal studies using Multitasking DCE technique with the access to the histology/pathology are preferable.

7.2.4 Follow-up study for therapy monitoring

One important utility to assess the vascular properties using DCE MRI is to monitor the therapeutic effect of pathological lesions. For example, in the treatment of tumor, the criteria of response are the morphologically decrease in the size of tumor. However, it usually takes time to wait for the morphological changes. Approach to evaluate the therapeutic effect at earlier stage for the optimization of treatment scheme individually is in great demand. Changes in the vascular properties are the hallmarks to indicate the status of the pathological lesions, which can be used as markers to evaluate the therapeutic effect. Multitasking DCE, as a quantitative technique with less variation due to the coil positioning, intra/inter-reader mismatch, can potentially provide an avenue to evaluate the changes of microenvironment of lesions at early stage. Future studies involving multi-time-point follow-up scans using Multitasking DCE will be designed.

7.2.5 Early diagnosis incorporating deep learning

Since early 1980s, computer-aided diagnosis (CAD) system has been brought to assist doctors to improve the interpretation of medical images. Feature exaction is the key step in most of the available system. In recent years, the idea of deep learning has been flourishing and widely explored in assisting the detection of tumors or residual lesions. The key advantage of deep learning is that it can directly generate the high-level feature representation from the raw images[171]. Currently most deep learning network are built on CT images due to the easy access to the data and the relatively simple contrast. In the meantime, interest has been growing to develop reliable deep learning tool for

disease detection based on MRI images to take advantages of the exquisite soft tissue contrast. To develop the deep learning network using the PK parametric maps from Multitasking DCE can increasingly exploit the vascular information of the tissues and provide an avenue for improved diagnosis.

Reference

1. Khalifa F, Soliman A, El-Baz A, Abou El-Ghar M, El-Diasty T, Gimel'farb G, Ouseph R, Dwyer AC. Models and methods for analyzing DCE-MRI: A review. *Med Phys* 2014;41(12).
2. Choyke PL, Dwyer AJ, Knopp MV. Functional tumor imaging with dynamic contrast-enhanced magnetic resonance imaging. *J Magn Reson Imaging* 2003;17(5):509-520.
3. Abe H, Mori N, Tsuchiya K, Schacht DV, Pineda FD, Jiang Y, Karczmar GS. Kinetic analysis of benign and malignant breast lesions with ultrafast dynamic contrast-enhanced MRI: comparison with standard kinetic assessment. *Am J Roentgenol* 2016;207(5):1159-1166.
4. Wang C-H, Yin F-F, Horton J, Chang Z. Review of treatment assessment using DCE-MRI in breast cancer radiation therapy. *World J Methodol* 2014;4(2):46.
5. Georgiou L, Sharma N, Broadbent DA, Wilson DJ, Dall BJ, Gangi A, Buckley DL. Estimating breast tumor blood flow during neoadjuvant chemotherapy using interleaved high temporal and high spatial resolution MRI. *Magn Reson Med* 2018;79(1):317-326.
6. Wasser K, Klein S, Fink C, Junkermann H, Sinn H, Zuna I, Knopp M, Delorme S. Evaluation of neoadjuvant chemotherapeutic response of breast cancer using dynamic MRI with high temporal resolution. *Eur Radiol* 2003;13(1):80-87.
7. Mankoff DA, Dunnwald LK, Gralow JR, Ellis GK, Schubert EK, Tseng J, Lawton TJ, Linden HM, Livingston RB. Changes in blood flow and metabolism in locally advanced breast cancer treated with neoadjuvant chemotherapy. *J Nucl Med* 2003;44(11):1806-1814.
8. Mazaheri Y, Akin O, Hricak H. Dynamic contrast-enhanced magnetic resonance imaging of prostate cancer: a review of current methods and applications. *World J Radiol* 2017;9(12):416.

9. Verma S, Turkbey B, Muradyan N, Rajesh A, Cornud F, Haider MA, Choyke PL, Harisinghani M. Overview of dynamic contrast-enhanced MRI in prostate cancer diagnosis and management. *Am J Roentgenol* 2012;198(6):1277-1288.
10. Mann RM, Kuhl CK, Kinkel K, Boetes C. Breast MRI: guidelines from the European society of breast imaging. *Eur Radiol* 2008;18(7):1307-1318.
11. Menezes GL, Knuttel FM, Stehouwer BL, Pijnappel RM, van den Bosch MA. Magnetic resonance imaging in breast cancer: a literature review and future perspectives. *World J Clin Oncol* 2014;5(2):61.
12. Schelfout K, Van Goethem M, Kersschot E, Colpaert C, Schelfhout A, Leyman P, Verslegers I, Biltjes I, Van Den Haute J, Gillardin J. Contrast-enhanced MR imaging of breast lesions and effect on treatment. *Eur J Surg Oncol* 2004;30(5):501-507.
13. Hlawatsch A, Teifke A, Schmidt M, Thelen M. Preoperative assessment of breast cancer: sonography versus MR imaging. *Am J Roentgenol* 2002;179(6):1493-1501.
14. Chen Z, Zheng Y, Ji G, Liu X, Li P, Cai L, Guo Y, Yang J. Accuracy of dynamic contrast-enhanced magnetic resonance imaging in the diagnosis of prostate cancer: systematic review and meta-analysis. *Oncotarget* 2017;8(44):77975.
15. Koelblinger C, Ba-Ssalamah A, Goetzinger P, Puchner S, Weber M, Sahora K, Scharitzer M, Plank C, Schima W. Gadobenate dimeglumine–enhanced 3.0-T MR imaging versus multiphasic 64–detector row CT: prospective evaluation in patients suspected of having pancreatic cancer. *Radiology* 2011;259(3):757-766.
16. Lee ES, Lee JM. Imaging diagnosis of pancreatic cancer: a state-of-the-art review. *World J Gastroenterol* 2014;20(24):7864.
17. Abramson RG, Li X, Hoyt TL, Su P-F, Arlinghaus LR, Wilson KJ, Abramson VG, Chakravarthy AB, Yankeelov TE. Early assessment of breast cancer response to neoadjuvant chemotherapy by semi-quantitative analysis of high-temporal resolution DCE-MRI: preliminary results. *Magn Reson Imaging* 2013;31(9):1457-1464.

18. Peng W, Fan J, Xue H. The relationship between DCE-MRI imaging manifestations, semi-quantitative parameters, and VEGF expression in breast cancer. *Int J Clin Exp Med* 2018;11(7):7224-7231.

19. Medved M, Karczmar G, Yang C, Dignam J, Gajewski TF, Kindler H, Vokes E, MacEneany P, Mitchell MT, Stadler WM. Semiquantitative analysis of dynamic contrast enhanced MRI in cancer patients: variability and changes in tumor tissue over time. *J Magn Reson Imaging* 2004;20(1):122-128.

20. Sourbron S, Buckley DL. Tracer kinetic modelling in MRI: estimating perfusion and capillary permeability. *Phys Med Biol* 2011;57(2):R1.

21. Sourbron SP, Buckley DL. Classic models for dynamic contrast-enhanced MRI. *NMR Biomed* 2013;26(8):1004-1027.

22. Kerwin WS, O'Brien KD, Ferguson MS, Polissar N, Hatsukami TS, Yuan C. Inflammation in carotid atherosclerotic plaque: A dynamic contrast-enhanced MR imaging study. *Radiology* 2006;241(2):459-468.

23. Calcagno C, Lobatto ME, Dyvorne H, Robson PM, Millon A, Senders ML, Lairez O, Ramachandran S, Coolen BF, Black A, Mulder WJ, Fayad ZA. Three-dimensional dynamic contrast-enhanced MRI for the accurate, extensive quantification of microvascular permeability in atherosclerotic plaques. *NMR Biomed* 2015;28(10):1304-1314.

24. Bali MA, Metens T, Denolin V, Delhaye M, Demetter P, Closset J, Matos C. Tumoral and nontumoral pancreas: correlation between quantitative dynamic contrast-enhanced MR imaging and histopathologic parameters. *Radiology* 2011;261(2):456-466.

25. Wegner CS, Hauge A, Gaustad J-V, Andersen LMK, Simonsen TG, Galappathi K, Rofstad EK. Dynamic contrast-enhanced MRI of the microenvironment of pancreatic adenocarcinoma xenografts. *Acta Oncologica* 2017;56(12):1754-1762.

26. Kim SH, Lee HS, Kang BJ, Song BJ, Kim H-B, Lee H, Jin M-S, Lee A. Dynamic contrast-enhanced MRI perfusion parameters as imaging biomarkers of angiogenesis. *PloS One* 2016;11(12).

27. Huuse EM, Moestue SA, Lindholm EM, Bathen TF, Nalwoga H, Krüger K, Bofin A, Mælandsmo GM, Akslen LA, Engebraaten O. In vivo MRI and histopathological assessment of tumor microenvironment in luminal-like and basal-like breast cancer xenografts. *Journal of Magnetic Resonance Imaging* 2012;35(5):1098-1107.

28. Zhang N, Zhang L, Qiu B, Meng L, Wang X, Hou BL. Correlation of volume transfer coefficient Ktrans with histopathologic grades of gliomas. *J Magn Reson Imaging* 2012;36(2):355-363.

29. Kim JH, Lee JM, Park JH, Kim SC, Joo I, Han JK, Choi BI. Solid pancreatic lesions: characterization by using timing bolus dynamic contrast-enhanced MR imaging assessment—a preliminary study. *Radiology* 2013;266(1):185-196.

30. Akisik MF, Sandrasegaran K, Bu G, Lin C, Hutchins GD, Chiorean EG. Pancreatic cancer: utility of dynamic contrast-enhanced MR imaging in assessment of antiangiogenic therapy. *Radiology* 2010;256(2):441-449.

31. Am O'Flynn E, Nandita Md. Functional magnetic resonance: biomarkers of response in breast cancer. *Breast Cancer Res* 2011;13(1):204.

32. Alonzi R, Padhani AR, Allen C. Dynamic contrast enhanced MRI in prostate cancer. *Eur J Radiol* 2007;63(3):335-350.

33. Alonzi R, Padhani AR, Taylor NJ, Collins DJ, D'Arcy JA, Stirling JJ, Saunders MI, Hoskin PJ. Antivascular effects of neoadjuvant androgen deprivation for prostate cancer: an in vivo human study using susceptibility and relaxivity dynamic MRI. *International Journal of Radiation Oncology*Biology*Physics* 2011;80(3):721-727.

34. Rosen MA, Schnall MD. Dynamic contrast-enhanced magnetic resonance imaging for assessing tumor vascularity and vascular effects of targeted therapies in renal cell carcinoma. *Clin Cancer Res* 2007;13(2):770s-776s.

35. Othman AE, Falkner F, Weiss J, Kruck S, Grimm R, Martirosian P, Nikolaou K, Notohamiprodjo M. Effect of temporal resolution on diagnostic performance of dynamic contrast-enhanced magnetic resonance imaging of the prostate. *Investigative radiology* 2016;51(5):290-296.

36. Kim H. Variability in Quantitative DCE-MRI: Sources and Solutions. *J Nat Sci* 2018;4(1).

37. Wake N, Chandarana H, Rusinek H, Fujimoto K, Moy L, Sodickson DK, Kim SG. Accuracy and precision of quantitative DCE-MRI parameters: How should one estimate contrast concentration? *Magn Reson Imaging* 2018;52:16-23.

38. Gries H, Rosenberg D, Weinmann H. Patent application. *Patent DE-OS* 1981;3129906:A1.

39. Lohrke J, Frenzel T, Endrikat J, Alves FC, Grist TM, Law M, Lee JM, Leiner T, Li K-C, Nikolaou K. 25 years of contrast-enhanced MRI: developments, current challenges and future perspectives. *Adv Ther* 2016;33(1):1-28.

40. Niendorf H, Laniado M, Semmler W, Schörner W, Felix R. Dose administration of gadolinium-DTPA in MR imaging of intracranial tumors. *Am J Neuroradiol* 1987;8(5):803-815.

41. Pineda F, Sheth D, Abe H, Medved M, Karczmar GS. Low-dose imaging technique (LITE) MRI: initial experience in breast imaging. *Br J Radiol* 2019;92(1103):20190302.

42. Kanda T, Ishii K, Kawaguchi H, Kitajima K, Takenaka DJR. High signal intensity in the dentate nucleus and globus pallidus on unenhanced T1-weighted MR images: relationship with increasing cumulative dose of a gadolinium-based contrast material. 2014;270(3):834-841.

43. Adin M, Kleinberg L, Vaidya D, Zan E, Mirbagheri S, Yousem D. Hyperintense dentate nuclei on T1-weighted MRI: relation to repeat gadolinium administration. *Am J Neuroradiol* 2015;36(10):1859-1865.

44. Carmeliet P, Jain RK. Angiogenesis in cancer and other diseases. *Nature* 2000;407(6801):249-257.

45. Adair TH, Montani J-P. Angiogenesis. 2010. Morgan & Claypool Life Sciences. p 1-84.

46. Patan S. Vasculogenesis and angiogenesis. Angiogenesis in Brain Tumors: *Springer*; 2004. p 3-32.

47. Martini L. Encyclopedia of endocrine diseases: *Elsevier acad. press*; 2004.

48. Folkman JJO, Canada: Decker. pp. Cancer Medicine IN: HOLLAND JF. 2000:132-152.

49. Viallard C, Larrivée B. Tumor angiogenesis and vascular normalization: alternative therapeutic targets. *Angiogenesis* 2017;20(4):409-426.

50. Park HJ, Griffin RJ, Hui S, Levitt SH, Song CW. Radiation-induced vascular damage in tumors: implications of vascular damage in ablative hypofractionated radiotherapy (SBRT and SRS). *Radiat Res* 2012;177(3):311-327.

51. Zuazo-Gaztelu I, Casanovas O. Unraveling the role of angiogenesis in cancer ecosystems. *Front Oncol* 2018;8:248.

52. Farnsworth RH, Lackmann M, Achen MG, Stacker SA. Vascular remodeling in cancer. *Oncogene* 2014;33(27):3496-3505.

53. Cuenod C, Balvay D. Perfusion and vascular permeability: basic concepts and measurement in DCE-CT and DCE-MRI. *Diagn Interv Radiol* 2013;94(12):1187-1204.

54. Bjørnerud A. The Physics of Magnetic Resonance Imaging: FYS-KJM 4740. *Department of Physics*

2008.

55. Laniado M, Weinmann H, Schörner W, Felix R, Speck U. First use of GdDTPA/dimeglumine in man. *Physiol Chem Phys Med NMR* 1984;16(2):157-165.

56. Grobner T. Gadolinium–a specific trigger for the development of nephrogenic fibrosing dermopathy and nephrogenic systemic fibrosis? *Nephrol Dial Transplant* 2006;21(4):1104-1108.

57. Becker S, Walter S, Witzke O, Kreuter A, Kribben A, Mitchell A. Application of gadolinium-based contrast agents and prevalence of nephrogenic systemic fibrosis in a cohort of end-stage renal disease patients on hemodialysis. *Nephron Clin Pract* 2012;121(1-2):c91-c94.

58. Wang Y, Alkasab TK, Narin O, Nazarian RM, Kaewlai R, Kay J, Abujudeh HH. Incidence of nephrogenic systemic fibrosis after adoption of restrictive gadolinium-based contrast agent guidelines. *Radiology* 2011;260(1):105-111.

59. Evelhoch JL. Key factors in the acquisition of contrast kinetic data for oncology. *J Magn Reson Imaging* 1999;10(3):254-259.

60. Hansford BG, Peng Y, Jiang Y, Vannier MW, Antic T, Thomas S, McCann S, Oto A. Dynamic contrast-enhanced MR imaging curve-type analysis: is it helpful in the differentiation of prostate cancer from healthy peripheral zone? *Radiology* 2015;275(2):448-457.

61. Dijkhoff RA, Maas M, Martens MH, Papanikolaou N, Lambregts DM, Beets GL, Beets-Tan RG. Correlation between quantitative and semiquantitative parameters in DCE-MRI with a blood pool agent in rectal cancer: can semiquantitative parameters be used as a surrogate for quantitative parameters? *Abdom Radiol* 2017;42(5):1342-1349.

62. Larsson H, Stubgaard M, Frederiksen J, Jensen M, Henriksen O, Paulson O. Quantitation of blood-brain barrier defect by magnetic resonance imaging and gadolinium-DTPA in patients with multiple sclerosis and brain tumors. *Magn Reson Med* 1990;16(1):117-131.

63. Tofts PS, Kermode AG. Measurement of the blood-brain barrier permeability and leakage space using dynamic MR imaging. 1. Fundamental concepts. *Magn Reson Med* 1991;17(2):357-367.

64. Brix G, Semmler W, Port R, Schad LR, Layer G, Lorenz WJ. Pharmacokinetic parameters in CNS Gd-DTPA enhanced MR imaging. *J Comput Assist Tomogr* 1991;15(4):621-628.

65. Tofts PS, Brix G, Buckley DL, Evelhoch JL, Henderson E, Knopp MV, Larsson HB, Lee TY, Mayr NA, Parker GJ, Port RE, Taylor J, Weisskoff RM. Estimating kinetic parameters from dynamic contrast-enhanced T(1)-weighted MRI of a diffusable tracer: standardized quantities and symbols. *J Magn Reson Imaging* 1999;10(3):223-232.

66. Parker GJ. Measuring contrast agent concentration in T 1-weighted dynamic contrast-enhanced MRI. Dynamic contrast-enhanced magnetic resonance imaging in oncology: *Springer*; 2005. p 69-79.

67. Gaens ME, Backes WH, Rozel S, Lipperts M, Sanders SN, Jaspers K, Cleutjens JP, Sluimer JC, Heeneman S, Daemen J-WH, Wildberger JE, Kwee RM, Kooi ME. Dynamic contrast-enhanced MR imaging of carotid atherosclerotic plaque: model selection, reproducibility, and validation. *Radiology* 2013;266(1):271-279.

68. Rahbar H, Partridge SC. Multiparametric MR imaging of breast cancer. *Magn Reson Imaging Clin* 2016;24(1):223-238.

69. Calcagno C, Mani V, Ramachandran S, Fayad ZA. Dynamic contrast enhanced (DCE) magnetic resonance imaging (MRI) of atherosclerotic plaque angiogenesis. *Angiogenesis* 2010;13(2):87-99.

70. Dong L, Kerwin WS, Chen HJ, Chu BC, Underhill HR, Neradilek MB, Hatsukami TS, Yuan C, Zhao XQ. Carotid Artery Atherosclerosis: Effect of Intensive Lipid Therapy on the Vasa Vasorum-Evaluation by Using Dynamic Contrast-enhanced MR Imaging. *Radiology* 2011;260(1):224-231.

71. Song HK, Dougherty L. k-Space weighted image contrast (KWIC) for contrast manipulation in projection reconstruction MRI. *Magn Reson Med* 2000;44(6):825-832.

72. Song HK, Dougherty L. Dynamic MRI with projection reconstruction and KWIC processing for simultaneous high spatial and temporal resolution. *Magn Reson Med* 2004;52(4):815-824.

73. Lin W, Guo J, Rosen MA, Song HK. Respiratory motion-compensated radial dynamic contrast-enhanced (DCE)-MRI of chest and abdominal lesions. *Magnetic Resonance in Medicine* 2008;60(5):1135-1146.

74. Feng L, Grimm R, Block KT, Chandarana H, Kim S, Xu J, Axel L, Sodickson DK, Otazo R. Golden-angle radial sparse parallel MRI: combination of compressed sensing, parallel imaging, and golden-angle radial sampling for fast and flexible dynamic volumetric MRI. *Magn Reson Med* 2014;72(3):707-717.

75. Feng L, Axel L, Chandarana H, Block KT, Sodickson DK, Otazo R. XD-GRASP: Golden-angle radial MRI with reconstruction of extra motion-state dimensions using compressed sensing. *Magn Reson Med* 2016;75(2):775-788.

76. Henderson E, Rutt BK, Lee T-Y. Temporal sampling requirements for the tracer kinetics modeling of breast disease. *Magn Reson Imaging* 1998;16(9):1057-1073.

77. Li KL, Buonaccorsi G, Thompson G, Cain JR, Watkins A, Russell D, Qureshi S, Evans DG, Lloyd SK, Zhu X. An improved coverage and spatial resolution—using dual injection dynamic contrast-enhanced (ICE-DICE) MRI: A novel dynamic contrast-enhanced technique for cerebral tumors. *Magn Reson Med* 2012;68(2):452-462.

78. Luypaert R, Sourbron S, de Mey JJMrim. Validity of perfusion parameters obtained using the modified Tofts model: a simulation study. 2011;65(5):1491-1497.

79. Christodoulou AG, Shaw JL, Nguyen C, Yang Q, Xie Y, Wang N, Li D. Magnetic resonance multitasking for motion-resolved quantitative cardiovascular imaging. *Nat Biomed Eng* 2018;2(4):215.

80. He J, Liu Q, Christodoulou AG, Ma C, Lam F, Liang Z-P. Accelerated High-Dimensional MR Imaging With Sparse Sampling Using Low-Rank Tensors. *IEEE Trans Med Imaging* 2016;35(9):2119-2129.

81. Christodoulou AG, Redler G, Clifford B, Liang Z-P, Halpern HJ, Epel B. Fast dynamic electron paramagnetic resonance (EPR) oxygen imaging using low-rank tensors. *Journal of Magnetic Resonance* 2016;270:176-182.

82. Liang Z-P. Spatiotemporal imagingwith partially separable functions. 2007. IEEE. p 988-991.

83. Lingala SG, Hu Y, DiBella E, Jacob M. Accelerated dynamic MRI exploiting sparsity and low-rank structure: kt SLR. *IEEE Trans Med Imaging* 2011;30(5):1042-1054.

84. Trzasko J, Manduca A, Borisch E. Local versus global low-rank promotion in dynamic MRI series reconstruction. 2011. p 4371.

85. Zhao B, Haldar JP, Christodoulou AG, Liang Z-P. Image Reconstruction From Highly Undersampled (k, t)-Space Data With Joint Partial Separability and Sparsity Constraints. *IEEE Trans Med Imaging* 2012;31(9):1809-1820.

86. Yuan C, Oikawa M, Miller Z, Hatsukami T. MRI of carotid atherosclerosis. *J Nucl Cardiol* 2008;15(2):266-275.

87. Ross R. Atherosclerosis—an inflammatory disease. *N Engl J Med* 1999;340(2):115-126.

88. Wasserman BA, Smith WI, Trout HH, Cannon RO, Balaban RS, Arai AE. Carotid artery atherosclerosis: in vivo morphologic characterization with gadolinium-enhanced double-oblique MR imaging—initial results. *Radiology* 2002;223(2):566-573.

89. Langheinrich AC, Kampschulte M, Buch T, Bohle RM. Vasa vasorum and atherosclerosis-Quid novi? *Thrombosis and Haemostasis* 2007;97(6):873-879.

90. Falk E. Why do plaques rupture? *Circulation* 1992;86(6 Suppl):III30-42.

91. Gillard J. Imaging of carotid artery disease: from luminology to function? *Neuroradiology* 2003;45(10):671-680.

92. Saba L, Anzidei M, Sanfilippo R, Montisci R, Lucatelli P, Catalano C, Passariello R, Mallarini G. Imaging of the carotid artery. *Atherosclerosis* 2012;220(2):294-309.

93. Naghavi M, Libby P, Falk E, Casscells SW, Litovsky S, Rumberger J, Badimon JJ, Stefanadis C, Moreno P, Pasterkamp G. From vulnerable plaque to vulnerable patient. *Circulation* 2003;108(14):1664-1672.

94. Calcagno C, Robson PM, Ramachandran S, Mani V, Kotys-Traughber M, Cham M, Fischer SE, Fayad ZA. SHILO, a novel dual imaging approach for simultaneous HI-/LOw temporal (Low-/Hi-spatial) resolution imaging for vascular dynamic contrast enhanced cardiovascular magnetic resonance: numerical simulations and feasibility in the carotid arteries. *J Cardiovasc Magn Reson* 2013;15.

95. Kerwin WS, Oikawa M, Yuan C, Jarvik GP, Hatsukami TS. MR imaging of adventitial vasa vasorum in carotid atherosclerosis. *Magn Reson Med* 2008;59(3):507-514.

96. Wu T, Wang J, Song Y, Deng X, Li A, Wei J, He L, Zhao X, Li R, Zhou Z, Wu W, Huang J, Jiao S, Yuan C, Chen H. Homologous HOmologous Black-Bright-blood and flexible Interleaved imaging sequence (HOBBI) for dynamic contrast-enhanced MRI of the vessel wall. *Magn Reson Med* 2015;73(5):1754-1763.

97. Gaens ME, Backes WH, Rozel S, Lipperts M, Sanders SN, Jaspers K, Cleutjens JPM, Sluimer JC, Heeneman S, Daemen MJAP, Welten RJTJ, Daemen JWH, Wildberger JE, Kwee RM, Kooi ME. Dynamic Contrast-enhanced MR Imaging of Carotid Atherosclerotic Plaque: Model Selection, Reproducibility, and Validation. *Radiology* 2013;266(1):271-279.

98. Liang Z-P. Spatiotemporal imaging with partially separable functions. Proc IEEE Int Symp Biomed Imaging2007. p 988-991.

99. Yu Y, Jin J, Liu F, Crozier S. Multidimensional compressed sensing MRI using tensor decomposition-based sparsifying transform. *PloS One* 2014;9(6):e98441.

100. Trzasko JD, Manduca A. A unified tensor regression framework for calibrationless dynamic, multi-channel MRI reconstruction. 2013.

101. Monajemi H, Jafarpour S, Gavish M, Donoho DL, Ambikasaran S, Bacallado S, Bharadia D, Chen Y, Choi Y, Chowdhury M. Deterministic matrices matching the compressed sensing phase transitions of Gaussian random matrices. *Proc Natl Acad Sci* 2013;110(4):1181-1186.

102. Wech T, Lemke A, Medway D, Stork LA, Lygate CA, Neubauer S, Köstler H, Schneider JE. Accelerating cine-MR imaging in mouse hearts using compressed sensing. *J Magn Reson Imaging* 2011;34(5):1072-1079.

103. Lingala SG, Hu Y, DiBella E, Jacob M. Accelerated dynamic MRI exploiting sparsity and low-rank structure: k-t SLR. *IEEE Trans Med Imaging* 2011;30(5):1042-1054.

104. Adluru G, Awate SP, Tasdizen T, Whitaker RT, DiBella EV. Temporally constrained reconstruction of dynamic cardiac perfusion MRI. *Magn Reson Med* 2007;57(6):1027-1036.

105. De Lathauwer L, De Moor B, Vandewalle J. A multilinear singular value decomposition. *SIAM J Matrix Anal Appl* 2000;21(4):1253-1278.

106. Morozov VA. On the solution of functional equations by the method of regularization. 1966. Russian Academy of Sciences. p 510-512.

107. Jaspers K, Aerts HJ, Leiner T, Oostendorp M, van Riel NA, Post MJ, Backes WH. Reliability of pharmacokinetic parameters: Small vs. medium-sized contrast agents. *Magn Reson Med* 2009;62(3):779-787.

108. Fan Z, Zuehlsdorff S, Liu X, Li D. Prospective self-gating for swallowing motion: A feasibility study in carotid artery wall MRI using three-dimensional variable-flip-angle turbo spin-echo. *Magn Reson Med* 2012;67(2):490-498.

109. Higaki T, Tatsugami F, Fujioka C, Sakane H, Nakamura Y, Baba Y, Iida M, Awai K. Visualization of simulated small vessels on computed tomography using a model-based iterative reconstruction technique. *Data in Brief* 2017;13:437-443.

110. Xue H, Greiser A, Zuehlsdorff S, Jolly MP, Guehring J, Arai AE, Kellman P. Phase-sensitive inversion recovery for myocardial T1 mapping with motion correction and parametric fitting. *Magn Reson Med* 2013;69(5):1408-1420.

111. McGraw KO, Wong SP. Forming inferences about some intraclass correlation coefficients. *Psychological Methods* 1996;1(1):30.

112. Millon A, Mathevet J-L, Boussel L, Faries PL, Fayad ZA, Douek PC, Feugier P. High-resolution magnetic resonance imaging of carotid atherosclerosis identifies vulnerable carotid plaques. *J Vasc Surg* 2013;57(4):1046-1051. e1042.

113. van Wijk DF, Strang AC, Duivenvoorden R, Enklaar D-JF, van der Geest RJ, Kastelein JJ, de Groot E, Stroes ES, Nederveen AJ. Increasing spatial resolution of 3T MRI scanning improves reproducibility of carotid arterial wall dimension measurements. *Magn Reson Mater Phy* 2014;27(3):219-226.

114. Cai J, Hatsukami TS, Ferguson MS, Kerwin WS, Saam T, Chu B, Takaya N, Polissar NL, Yuan C. In vivo quantitative measurement of intact fibrous cap and lipid-rich necrotic core size in atherosclerotic carotid plaque. *Circulation* 2005;112(22):3437-3444.

115. Danet IM, Semelka RC, Nagase LL, Woosely JT, Leonardou P, Armao D. Liver metastases from pancreatic adenocarcinoma: MR imaging characteristics. *Journal of Magnetic Resonance Imaging: An Official Journal of the International Society for Magnetic Resonance in Medicine* 2003;18(2):181-188.

116. Li D, Xie K, Wolff R, Abbruzzese JL. Pancreatic cancer. *The Lancet* 2004;363(9414):1049-1057.

117. Siegel RL, Miller KD, Jemal A. Cancer statistics, 2017. *CA* 2017;67(1):7-30.

118. Keleg S, Büchler P, Ludwig R, Büchler MW, Friess H. Invasion and metastasis in pancreatic cancer. *Molecular Cancer* 2003;2(1):14.

119. Oberstein PE, Olive KP. Pancreatic cancer: why is it so hard to treat? *Therapeutic Advances in Gastroenterology* 2013;6(4):321-337.

120. Scheufele F, Hartmann D, Friess H. Treatment of pancreatic cancer—neoadjuvant treatment in borderline resectable/locally advanced pancreatic cancer. *Transl Gastroenterol Hepatol* 2019;4.

121. Holzapfel K, Reiser-Erkan C, Fingerle AA, Erkan M, Eiber MJ, Rummeny EJ, Friess H, Kleeff J, Gaa J. Comparison of diffusion-weighted MR imaging and multidetector-row CT in the detection of liver metastases in patients operated for pancreatic cancer. *Abdominal Imaging* 2011;36(2):179-184.

122. Danet IM, Semelka RC, Nagase LL, Woosely JT, Leonardou P, Armao D. Liver metastases from pancreatic adenocarcinoma: MR imaging characteristics. *J Magn Reson Imaging* 2003;18(2):181-188.

123. Park HS, Lee JM, Choi HK, Hong SH, Han JK, Choi BI. Preoperative evaluation of pancreatic cancer: comparison of gadolinium-enhanced dynamic MRI with MR cholangiopancreatography versus MDCT. *J Magn Reson Imaging* 2009;30(3):586-595.

124. Schima W, Függer R. Evaluation of focal pancreatic masses: comparison of mangafodipir-enhanced MR imaging and contrast-enhanced helical CT. *Eur Radiol* 2002;12(12):2998-3008.

125. Naish J, Hutchinson C, Caunce A, Roberts C, Waterton J, Hockings P, Taylor C, Parker GJJoMRI. Multiple-bolus dynamic contrast-enhanced MRI in the pancreas during a glucose challenge. 2010;32(3):622-628.

126. Ippoliti M, Lukas M, Winfried B, Schaeffter T, Makowski MR, Kolbitsch C. 3D nonrigid motion correction for quantitative assessment of hepatic lesions in DCE-MRI. *Magn Reson Med* 2019.

127. Wang N, Christodoulou AG, Xie Y, Wang Z, Deng Z, Zhou B, Lee S, Fan Z, Chang H, Yu W. Quantitative 3D dynamic contrast-enhanced (DCE) MR imaging of carotid vessel wall by fast T1 mapping using Multitasking. *Magnetic resonance in medicine* 2018.

128. Kolda TG, Bader BW. Tensor decompositions and applications. *SIAM review* 2009;51(3):455-500.

129. Zhou R, Huang W, Yang Y, Chen X, Weller DS, Kramer CM, Kozerke S, Salerno M. Simple motion correction strategy reduces respiratory-induced motion artifacts for kt accelerated and compressed-sensing cardiovascular magnetic resonance perfusion imaging. *J Cardiovasc Magn Reson* 2018;20(1):6.

130. De Lathauwer L, De Moor B, Vandewalle J. A multilinear singular value decomposition. *SIAM journal on Matrix Analysis and Applications* 2000;21(4):1253-1278.

131. Tofts PS, Brix G, Buckley DL, Evelhoch JL, Henderson E, Knopp MV, Larsson HB, Lee T-Y, Mayr NA, Parker GJ. Estimating kinetic parameters from dynamic contrast-enhanced T 1-weighted MRI of a diffusable tracer: standardized quantities and symbols. *J Magn Reson Imaging* 1999;10(3):223-232.

132. Messroghli DR, Radjenovic A, Kozerke S, Higgins DM, Sivananthan MU, Ridgway JP. Modified Look-Locker inversion recovery (MOLLI) for high-resolution T1 mapping of the heart. *Magn Reson Med* 2004;52(1):141-146.

133. Russek S, Boss M, Jackson E, Jennings D, Evelhoch J, Gunter J, Sorensen A. Characterization of NIST/ISMRM MRI system phantom. 2012. p 2456.

134. Esserman L, Hylton N, George T, Weidner N. Contrast-enhanced magnetic resonance imaging to assess tumor histopathology and angiogenesis in breast carcinoma. *The breast journal* 1999;5(1):13-21.

135. Su MY, Cheung YC, Fruehauf JP, Yu H, Nalcioglu O, Mechetner E, Kyshtoobayeva A, Chen SC, Hsueh S, McLaren CE. Correlation of dynamic contrast enhancement MRI

parameters with microvessel density and VEGF for assessment of angiogenesis in breast cancer. *J Magn Reson Imaging* 2003;18(4):467-477.

136. de Lussanet QG, Backes WH, Griffioen AW, Padhani AR, Baeten CI, van Baardwijk A, Lambin P, Beets GL, van Engelshoven JM, Beets-Tan RG. Dynamic contrast-enhanced magnetic resonance imaging of radiation therapy-induced microcirculation changes in rectal cancer. *International Journal of Radiation Oncology* Biology* Physics* 2005;63(5):1309-1315.

137. Feng L, Wen Q, Huang C, Tong A, Liu F, Chandarana H. GRASP-Pro: imProving GRASP DCE-MRI through self-calibrating subspace-modeling and contrast phase automation. *Magn Reson Med* 2019.

138. Yachida S, Iacobuzio-Donahue CA. The pathology and genetics of metastatic pancreatic cancer. *Arch Pathol Lab Med* 2009;133(3):413-422.

139. Embuscado EE, Laheru D, Ricci F, Yun KJ, de Boom Witzel S, Seigel A, Flickinger K, Hidalgo M, Bova GS, Iacobuzio-Donahue CA. Immortalizing the complexity of cancer metastasis: genetic features of lethal metastatic pancreatic cancer obtained from rapid autopsy. *Cancer biology & therapy* 2005;4(5):548-554.

140. Disibio G, French SW. Metastatic patterns of cancers: results from a large autopsy study. *Arch Pathol Lab Med* 2008;132(6):931-939.

141. Teixeira T, Hafyane T, Stikov N, Akdeniz C, Greiser A, Friedrich MG. Comparison of different cardiovascular magnetic resonance sequences for native myocardial T1 mapping at 3T. *J Cardiovasc Magn Reson* 2016;18(1):65.

142. Mantovani A, Allavena P, Sica A, Balkwill F. Cancer-related inflammation. *Nature* 2008;454(7203):436.

143. Coussens LM, Werb Z. Inflammation and cancer. *Nature* 2002;420(6917):860.

144. Coenegrachts K, Van Steenbergen W, De Keyzer F, Vanbeckevoort D, Bielen D, Chen F, Dockx S, Maes F, Bosmans HJJoMRIAOJotISfMRiM. Dynamic contrast-enhanced

MRI of the pancreas: initial results in healthy volunteers and patients with chronic pancreatitis. 2004;20(6):990-997.

145. Johnson PT, Outwater EK. Pancreatic carcinoma versus chronic pancreatitis: dynamic MR imaging. *Radiology* 1999;212(1):213-218.

146. Tajima Y, Kuroki T, Tsutsumi R, Isomoto I, Uetani M, Kanematsu T. Pancreatic carcinoma coexisting with chronic pancreatitis versus tumor-forming pancreatitis: diagnostic utility of the time-signal intensity curve from dynamic contrast-enhanced MR imaging. *World J Gastroenterol* 2007;13(6):858.

147. Zhang T-T, Wang L, Liu H-h, Zhang C-y, Li X-m, Lu J-p, Wang D-b. Differentiation of pancreatic carcinoma and mass-forming focal pancreatitis: qualitative and quantitative assessment by dynamic contrast-enhanced MRI combined with diffusion-weighted imaging. *Oncotarget* 2017;8(1):1744.

148. Adelson JW, Miller PE. Heterogeneity of the exocrine pancreas. *Am J Physiol Gastrointest Liver Physiol* 1989;256(5):G817-G825.

149. Schoennagel BP, Habermann CR, Roesch M, Hahne JD, Arndt C, Kleibeler L, Petersen KU, Graessner J, Adam G, Herrmann J. Diffusion-weighted imaging of the healthy pancreas: Apparent diffusion coefficient values of the normal head, body, and tail calculated from different sets of b-values. *J Magn Reson Imaging* 2011;34(4):861-865.

150. Kong X, Sun T, Kong F, Du Y, Li Z. Chronic pancreatitis and pancreatic cancer. *Gastrointest Tumors* 2014;1(3):123-134.

151. Shu J, Zhang XM, Zhao JN, Yang L, Zeng NL, Zhai ZH. DCE-MRI in experimental chronic pancreatitis. *Contrast Media Mol Imaging* 2009;4(3):127-134.

152. Gupte AR, Forsmark CE. Chronic pancreatitis. *Curr Opin Gastroenterol* 2014;30(5):500-505.

153. Sandrasegaran K, Nutakki K, Tahir B, Dhanabal A, Tann M, Cote GA. Use of diffusion-weighted MRI to differentiate chronic pancreatitis from pancreatic cancer. *American Journal of Roentgenology*
2013;201(5):1002-1008.

154. Van Gulik T, Moojen T, Van Geenen R, Obertop H, Gouma D, Rauws E. Differential diagnosis of focal pancreatitis and pancreatic cancer. *Ann Oncol* 1999;10:S85-S88.

155. Wang L, Gaddam S, Wang N, Xie Y, Deng Z, Zhou Z, Fan Z, Jiang T, Christodoulou AG, Han F, Lo SK, Wachsman AM, Hendifar AE, Pandol SJ, Li D. Multiparametric Mapping Magnetic Resonance Imaging of Pancreatic Disease. *Front Physiol* 2020;11:8.

156. Kim JK, Altun E, Elias Jr J, Pamuklar E, Rivero H, Semelka RC. Focal pancreatic mass: Distinction of pancreatic cancer from chronic pancreatitis using gadolinium-enhanced 3D-gradient-echo MRI. *J Magn Reson Imaging* 2007;26(2):313-322.

157. Fattahi R, Balci NC, Perman WH, Hsueh EC, Alkaade S, Havlioglu N, Burton FR. Pancreatic diffusion-weighted imaging (DWI): comparison between mass-forming focal pancreatitis (FP), pancreatic cancer (PC), and normal pancreas. *J Magn Reson Imaging* 2009;29(2):350-356.

158. Wang L. Early diagnosis of breast cancer. *Sensors* 2017;17(7):1572.

159. Huang W, Tudorica LA, Li X, Thakur SB, Chen Y, Morris EA, Tagge IJ, Korenblit ME, Rooney WD, Koutcher JA. Discrimination of benign and malignant breast lesions by using shutter-speed dynamic contrast-enhanced MR imaging. *Radiology* 2011;261(2):394-403.

160. Jena A, Taneja S, Singh A, Negi P, Mehta SB, Sarin R. Role of pharmacokinetic parameters derived with high temporal resolution DCE MRI using simultaneous PET/MRI system in breast cancer: a feasibility study. *Eur J Radiol* 2017;86:261-266.

161. Wang N, Gaddam S, Wang L, Xie Y, Fan Z, Yang W, Tuli R, Lo SK, Hendifar AE, Pandol SJ, Li D. Six-dimensional quantitative DCE MR Multitasking of the entire abdomen:

Method and application to pancreatic ductal adenocarcinoma. *Magn Reson Med* 2020;84(2):928-948.

162. Wang N, Christodoulou AG, Xie Y, Wang Z, Deng Z, Zhou B, Lee S, Fan Z, Chang H, Yu W, Li D. Quantitative 3D dynamic contrast-enhanced (DCE) MR imaging of carotid vessel wall by fast T1 mapping using Multitasking. *Magn Reson Med* 2019;81(4):2302-2314.

163. Shahid H, Wiedenhoefer JF, Carol Dornbluth MD D, Pamela Otto M, Kist KA. An overview of breast MRI. *Appl Radiol* 2016;45(10):7.

164. Brix G, Kiessling F, Lucht R, Darai S, Wasser K, Delorme S, Griebel J. Microcirculation and microvasculature in breast tumors: pharmacokinetic analysis of dynamic MR image series. *Magn Reson Med* 2004;52(2):420-429.

165. He D, Chatterjee A, Fan X, Wang S, Eggener S, Yousuf A, Antic T, Oto A, Karczmar GS. Feasibility of Dynamic Contrast-Enhanced Magnetic Resonance Imaging Using Low-Dose Gadolinium: Comparative Performance With Standard Dose in Prostate Cancer Diagnosis. *Invest Radiol* 2018;53(10):609-615.

166. Li KL, Lewis D, Jackson A, Zhao S, Zhu X. Low-dose T1W DCE-MRI for early time points perfusion measurement in patients with intracranial tumors: A pilot study applying the microsphere model to measure absolute cerebral blood flow. *J Magn Reson Imaging* 2018;48(2):543-557.

167. Makkat S, Luypaert R, Sourbron S, Stadnik T, De Mey J. Quantification of perfusion and permeability in breast tumors with a deconvolution-based analysis of second-bolus T1-DCE data. *J Magn Reson Imaging* 2007;25(6):1159-1167.

168. Drisis S, Metens T, Ignatiadis M, Stathopoulos K, Chao S-L, Lemort M. Quantitative DCE-MRI for prediction of pathological complete response following neoadjuvant treatment for locally advanced breast cancer: the impact of breast cancer subtypes on the diagnostic accuracy. *Eur Radiol* 2016;26(5):1474-1484.

169. Yang G, Yu S, Dong H, Slabaugh G, Dragotti PL, Ye X, Liu F, Arridge S, Keegan J, Guo Y. DAGAN: Deep de-aliasing generative adversarial networks for fast compressed sensing MRI reconstruction. *IEEE Trans Med Imaging* 2017;37(6):1310-1321.

170. Schlemper J, Caballero J, Hajnal JV, Price AN, Rueckert D. A deep cascade of convolutional neural networks for dynamic MR image reconstruction. *IEEE Trans Med Imaging* 2017;37(2):491-503.

171. Munir K, Elahi H, Ayub A, Frezza F, Rizzi AJC. Cancer Diagnosis Using Deep Learning: A Bibliographic Review. *Cancers* 2019;11(9):1235.